Antibody-Immobilized Cellulose Nanocrystals for the Detection of Cancer Biomarkers

by

Uma Madhuri Nori

A thesis submitted to the Graduate Faculty of
Auburn University
in partial fulfillment of the
requirements for the Degree of
Master of Science

Auburn, Alabama
December 14, 2019

Keywords: Cellulose nanocrystals, biosensors, surface functionalization, cancer detection, antibodies, biomarkers

Approved by

Dr. Virginia Davis, Chair, Alumni Professor, Chemical Engineering
Dr. William R. Ashurst, Associate Department Chair, Chemical Engineering
Dr. Maria Auad, Professor, Chemical Engineering
Dr. Soledad Peresin, Assistant Professor, Forestry & Wildlife Science

Abstract

Naturally derived anisotropic nanomaterials such as cellulose nanocrystals (CNC) are an intriguing material for biosensors due to their exceptional mechanical properties, nanoscale structure, and sustainability. However, relatively little is known about antibody immobilization on CNC; this is particularly true for the commonly available CNC that are produced by sulfuric acid extraction from woody biomass. The main objective of this research was to develop a multi-step reaction scheme to immobilize model cancer antibodies on the surfaces of CNC in a liquid dispersion and compare the results to a previously established method for immobilizing antibodies on solid CNC films. An additional objective was to understand whether the modified CNC could be used as probe for the cancer detection of the corresponding antigens.

All of the surface modifications were performed using 3-aminopropyl-triethoxysilane (APTES) and glutaric anhydride (GA) chemistry. This was followed by the immobilization of the following primary monoclonal antibodies: alpha-fetoprotein (AFP) antibody, which is used in liver cancer detection, prostate-specific antigen (PSA) antibody which is used in prostate cancer detection, and carcinoembryonic antigen (CEA) antibody which is used in ovarian cancer detection. To the best of author's knowledge, quartz crystal microbalance with dissipation monitoring (QCM-D) has never been used before for characterizing or analyzing the sensing performance of the antibody-immobilized CNC. In this work, QCM-D was used to follow each step of the immobilization scheme and antigen-binding in real time. QCM-D also enabled quantification of the amounts of antibody and antigen-binding. In addition, thermal gravimetric analysis (TGA) and Fourier Transform Infrared Spectroscopy (FTIR), coupled TGA-FTIR, and

microscopy methods were used to characterize the results of each step in the protocol. In addition, fluorescence anisotropy (FA) was used to explore the selectivity of the antibody-antigen binding.

All antibodies were successfully immobilized on both dispersed CNC and CNC films. While immobilization on the films was the simpler, greater immobilization and antigen-binding were achieved on dispersed CNC. This is attributed to the accessibility of the entire CNC surface area for functionalization in the dispersions; in contrast only the outermost CNC surfaces were accessible in the solid films. However, APTES functionalization of dispersed CNC tended to result in cross-linking and aggregation; this was mitigated by running the reaction at relatively dilute conditions. The extent of aggregation was characterized using optical microscopy, scanning electron microscopy (SEM) with energy dispersive X-ray spectroscopy (EDS). In terms of differences between the model antibodies, CEA antibody showed the highest affinity to its immunogen (CEA) whereas the antibodies PSA and AFP showed cross-reactivities with other antigens from the QCM-D and FA results.

This research provides novel insights into the challenges and benefits of immobilizing antibodies on CNC using different approaches and provides a framework for detailed analysis of the process using QCM-D in addition to more standard analytical techniques. This pioneering research study also highlights the promise of using antibody immobilization on CNC for biomarker detection using piezo-based methods such as QCM-D and microcantilever arrays.

Acknowledgments

I would first like to thank my thesis advisor Dr. Virginia A. Davis of the Chemical Engineering department at Auburn University. The door to Dr. Davis's office was always open whenever I had a question about my research or writing. She consistently allowed this thesis to be my work but steered me in the right direction whenever she thought I needed it.

Secondly, I would like to thank my committee members of this thesis: Dr. William R. Ashurst, Dr. Maria Auad of Chemical Engineering for their passionate participation and input, encouragement, insightful comments, and hard questions. I would also like to acknowledge Dr. Soledad Peresin of the Forestry & Wildlife Sciences department at Auburn University for her support as the outside reader of this thesis, and I am grateful for her valuable comments on this thesis.

I would like to thank Diego Gómez Maldonado from Forestry & Wildlife Sciences, Yuan Tian from Chemical Engineering, Dr. Micheal E. Miller from Auburn University Instrumentation Facility, and Dr. Paul A. Cobine from Biological Sciences for helping me with the various analytical techniques.

I thank my fellow lab mates in Dr. Davis's Group: Matthew Noor, Zahra Karimi, Fatima Hamade, Sadat Amit, Delaney Clouse, Mackenzie Bockhold, Marisa Rodriguez, and Lindsey Parsons, Elliott Glover and Dr. Partha Saha for the stimulating discussions, encouragement while working together before deadlines, and for all the fun. Also, I thank my friends at Auburn University: Rithvija Avvari, Abhinav Saxena and Vinita Shinde who were my biggest support system. I would like to thank the Chemical Engineering department faculty, staff members especially Ms. Elaine Manning for their constant encouragement and support.

Finally, I must express my very profound gratitude to my family Mr. Srinivas Nori, Ms. Jaya Nori, Sumanth Nori and Mr. Dinesh Ponnathota for providing me with unfailing support and continuous encouragement throughout my years of study and through the process of researching and writing this thesis.

Table of Contents

List of Tables

List of Figures

List of Abbreviations

CNC	Cellulose nanocrystals
APTES	3-aminopropyl-triethoxy silane
GA	Glutaric anhydride
ATR-IR	Attenuated total reflection infrared spectroscopy
SEM	Scanning electron microscope
EDS	Energy dispersive X-ray spectroscopy
FESEM	Field emission scanning electron microscope
QCM-D	Quartz crystal microbalance with dissipation monitoring
FA	Fluorescence anisotropy
CEA	Carcinoembryonic antigen
AFP	Alpha-fetoprotein
PSA	Prostate-specific antigen
POC	Point-of-care
TGA	Thermogravimetric analysis
FTIR	Fourier Transform Infrared Spectroscopy
IgG	Immunoglobulin
TRITC	Tetramethylrhodamine
CP	Cross-polarized
HAT	Hypoxanthine-aminopterin-thymidine
HGPRT	Hypoxanthine: guanine phosphoribosyl transferase
ELISA	Enzyme-linked immunosorbent assay

MEMS	Micro-electro-mechanical systems
SPR	Surface plasmon resonance
BSA	Bovine serum albumin
AFM	Atomic force microscope
EHT	Electron high tension

Chapter 1. Introduction

Cancer is the second leading cause of death in the United States and most developing countries.[1, 2] Early diagnosis of the disease has been found to be pivotal for the successful treatment of the disease.[2-4] On the other hand, lack of rapid and economical diagnostic techniques for successful biomarker detection is also a key factor for cancer-causing mortalities.[5] During the past decade, point-of-care (POC) biosensor devices have emerged as a powerful tool in this front, enabling real-time, rapid, label-free, sensitive and economic detection of the disease biomarkers.[6] Nanomaterial probes, due to their high surface area to volume ratios, provide numerous immobilized detection sites for the target biomarker.[6] With this motivation, the main goal of this thesis was to develop antibody immobilized cellulose nanocrystal-based biosensor probes via a multi-step reaction scheme in dispersion for the detection of model cancer biomarkers.

In this research, wood-based sulfuric acid hydrolyzed cellulose nanocrystals (CNC) were used to demonstrate sensitive detection of the model cancer biomarkers namely alpha-fetoprotein (AFP), prostate-specific antigen (PSA), and carcinoembryonic antigen (CEA) used in the liver, prostate, and ovarian cancer detection respectively. Naturally derived CNC are unique materials due to their high aspect ratios (10-70),[7] high specific surface area (150 m^2/g),[8] impressive mechanical properties such as high strength and modulus (10 and 150 GPa, respectively),[9] and biodegradability. CNC are also considered benign and biocompatible as compared to similar high-performance materials.[10] However, CNC have some limitations for use in industry and high-performance applications. The most relevant drawback here is that the materials assembled from CNC which were extracted using sulfuric acid hydrolysis lack hydrolytic stability needed for applications requiring immersion in aqueous solutions. Other extraction methods can result in

better hydrolytic stability but poor dispersibility during processing.[11-14] Both of these issues can impact the bulk mechanical properties of solid materials assembled from CNC.[12]

In the case of CNC produced by sulfuric acid hydrolysis of cellulose, ~ 30% of the native hydroxyl (-OH) groups are replaced with negative sulfate half esters ($-OSO_3^-$) [15]; the remaining –OH groups are available for typical functionalization schemes such as cationization, acetylation, oxidation, and silylation. Silylation improves the hydrolytic stability of solid CNC materials and various processes have been developed by the researchers to graft silane onto the CNC using[19-21] but most of them involve tedious[22] and hazardous steps. In this study, 3-aminopropyl-triethoxysilane (APTES) functionalization was performed on the CNC. APTES was chosen as it is highly reactive, less toxic, economical, and because of its amino group ($-NH_2$). APTES is one of the most standard reagents used for the immobilizing antibodies and other biomolecules. Additional background on CNC and their modification is in Chapter 2, and the methodologies for the CNC modification and characterization are presented in Chapter 3.

For the dispersed CNC, the rapid polymerization reaction that occurs between CNC and APTES can result in aggregation and crosslinking. After multiple trials, this issue was largely resolved by running one of the possible functionalization methods at relatively dilute conditions. The resulting APTES modified CNC from each methodology were labeled accordingly. The APTES reaction was followed by further surface modification with GA (glutaric anhydride), which acts as an organo-linker for the successful immobilization of the model cancer antibodies. The GA modification also retards the denaturation or accidental removal of the immobilized antibody from the CNC-APTES surface during further processing.[23] After the reaction with GA, the antibodies for the model biomarkers were immobilized: anti-alpha-fetoprotein (antiAFP), anti-prostate-specific antigen (antiPSA), and anti-carcinoembryonic antigen (antiCEA). Finally, the antiCEA,

antiAFP and antiPSA immobilized CNC were reacted with their respective antigens namely CEA, AFP and PSA. After each step of the process, a detailed characterization of the resulting materials were performed using analytical tools such as optical microscopy, fluorescence microscopy, scanning electron microscopy with energy dispersive X-ray spectroscopy (SEM/EDS), goniometry, and thermal gravimetric analysis (TGA), Fourier Transform Infrared Spectroscopy (FTIR), and coupled TGA-FTIR. These and other results are explained in Chapter 4.

In addition, to the previously listed techniques, quartz crystal microbalance with dissipation monitoring (QCM-D) analysis was performed to monitor the modification steps and quantify antibody and antigen-binding. The advantages of the QCM-D result from its ability to provide a real-time analysis of a reaction and sensitive detection of the mass of each layer adsorbed. In one study, the antibody immobilized dispersions were spin-coated on to QCM-D mass sensors (also known as Qsensors), introduced into QCM-D chambers and the respective antigen solutions were passed through the sensor surfaces. In a different approach, the CNC dispersions were first spin-coated on the Qsensors which were then introduced into QCM-D for all the series of reactions with reagents (APTES, GA, antibody and antigen). This was known as the film modification scheme on CNC which had similar reaction parameters as dispersion modification. QCM-D was used to compare the antigen detection capabilities of the dispersion modified and film modified CNC. Both film and dispersion modification schemes on CNC resulted in antibody immobilization, but greater immobilization and antigen-binding were achieved on dispersed CNC. This is attributed to the accessibility of the entire CNC surface area in the dispersions. However, film modification scheme was the simplest as compared to the dispersion modification on CNC. Based on the QCM-D results, the antibody CEA detected its immunogen which is the antigen CEA with highest

affinity as compared to the other two antibodies which are AFP and PSA in the dispersion modification scheme.

In addition, since the antibodies used had fluorescent probes attached to them, fluorescence imaging was performed to compare the change in fluorescence intensities between the GA-modified CNC and antibody-immobilized CNC. Fluorescence anisotropy (FA) was used to confirm the antigen-binding with its respective antibody surface for all the three biomarker cases. The differences in anisotropy between the antibody immobilized CNC and the ultimate antigen bound CNC dispersions allowed to discern whether the antigen detection reactions were successful.

QCM-D and FA were also used to understand the specificity of each antigen to its immunogen, and to evaluate the cross-reactivity behaviors of the antibodies towards other antigens. In QCM-D, the dispersion-modified, antibody immobilized CNC surfaces were prepared by spin coating on the Qsensors. They were then tested individually for their specificity/cross-reactivity by passing all the three antigens *in situ.* Similarly, FA was also used to check for the changes in anisotropy values between the antibody-immobilized CNC and antigen immobilized CNC. To facilitate this analysis, each of the antibody-immobilized CNC dispersions were reacted with other antigens instead of its immunogen. This technique was also used to measure the fluorescence intensities of all the samples namely after GA, antibody-antigen reactions (including cross-reactions). The specificity was confirmed based on the highest increase in anisotropy in case of an antibody-immunogen (specific antigen) pair as compared to antibody-other antigen pair. From the QCM-D specificity experiments, only the antibody CEA was specific to its immunogen CEA. Antibody AFP cross-reacted with CEA and PSA; and antibody PSA cross-reacted with CEA. This was also confirmed from the FA measurements, where the antibody CEA showed highest

affinity to its antigen CEA from the highest increase in anisotropy while the other antibodies showed cross-reactivity behaviors.

To the best of the author's knowledge, this work provides the first detailed insights into CNC modification for the detection of cancer biomarkers. Chapter 5 provides a summary of the conclusions from this research and suggestions for future research. It also describes the challenges and advantages of CNC-based biosensors and their potential application in point-of-care diagnostics.

Chapter 2. Background

2.1. Cellulose

Cellulose, a tough fibrous carbohydrate polymer (polysaccharide) is the most abundant renewable polymer on earth.[24] About fifty percent of natural biomass is comprised of cellulose.[25, 26] The chemical formula is $(C_6H_{10}O_5)_n$, where n ranges from 10000 to 15000 and depends on the source material from which cellulose is extracted. It consists of 1,4-anhydro-D-glucopyranose units as depicted in (Figure 1) and the chain has a flat ribbon-like conformation.[27] The tensile strength of cellulose is on par with the commercial fibers such as carbon fiber.[28]

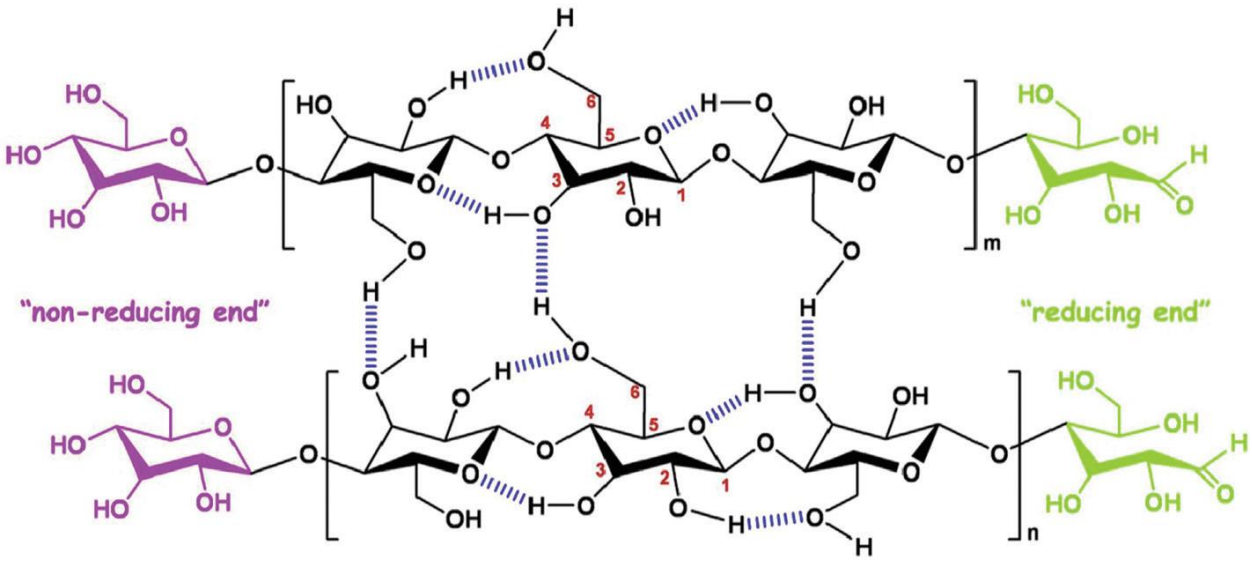

Figure 1 Schematic representation of the chemical structure and intra-, inter-molecular hydrogen bonds in cellulose.[29]

The cellulose comes in various forms such as microcrystalline cellulose and nanocrystalline cellulose, etc. Nanocellulose based materials are perceived to have a great potential in revolutionizing the domain of point-of-care (POC) diagnostics.[30-33] As the name suggests,

nanocellulose has one or more dimensions in the nanometer range (<100 nm).[34, 35] There are various nanomaterials that come under the family of nanocellulose.[36] Among these, the rod-like cellulose nanocrystals (CNC) which are commonly extracted through chemical treatments such as acid hydrolysis from cellulose have gained tremendous popularity in the sustainable biosensing applications over the last decade.[37, 38]

2.2. Cellulose nanocrystals (CNC)

CNC can be isolated from various cellulose sources such as micro-organisms (bacteria, fungi, algae); bio-based materials (wood, flax, cotton, hemp) and even sea animals such as tunicates.[28, 34, 37-41] One of the most attractive property of CNC is their high aspect ratio; the specific value is dependent on the source from which they are extracted. Table 1 presents the range of aspect ratios of CNC extracted from each of these sources. CNC represent the most highly crystalline fraction of cellulose with the degree of crystallinity in the range of 54-88 % depending on the source type and extraction process.[34] The CNC are very rigid and stiff for this very reason. The CNC derived from tunicates are known to have the highest crystallinity values.[34]

Table 1 Aspect Ratio of cellulose nanocrystals (CNC) Derived from Different Sources.[42]

	Source Length (nm)	Width (nm)	Aspect Ratio
Bacterial	640–1070	12–22	50
Cotton	100–30	4–10	29
Flax	100–500	10–30	15
Ramie	150–250	6–8	29
Sisal	150–350	3–5	62
Tunicate (Sea animal)	500–2000	10–20	83
Wood	100–200	3–15	17

Cellulose fibers can be converted to CNC by a two-stage isolation method. For the cellulose sources such as wood, plant etc. a pre-treatment and homogenization steps are required to remove

hemicellulose, lignin, etc. (matrix material) and isolation of cellulose fibres.[43] In the second stage, the purified cellulose and its crystalline components are separated. There is a range of methods to isolate CNC from its source including mechanical treatment[44-46] chemical treatment (acid hydrolysis)[44, 45, 47] and enzymatic hydrolysis.[44, 45] When treated with acids, the amorphous regions in the cellulose get preferentially disintegrate as a result of the difference in the kinetics of the hydrolysis between amorphous and crystalline domains of cellulose.[47] The mechanism involves protonation of the glucosidic oxygen followed by dissociation of glucosidic bonds (hydrolytic cleavage) in the amorphous regions. Then due to the deprotonation and nucleophile formation in the acid molecules, the protonation of out of the plane -OH groups of cellulose take place resulting in nucleophile substitution and condensation.[47] Therefore, a colloidal suspension of cellulose crystallites are formed (Figure 2).

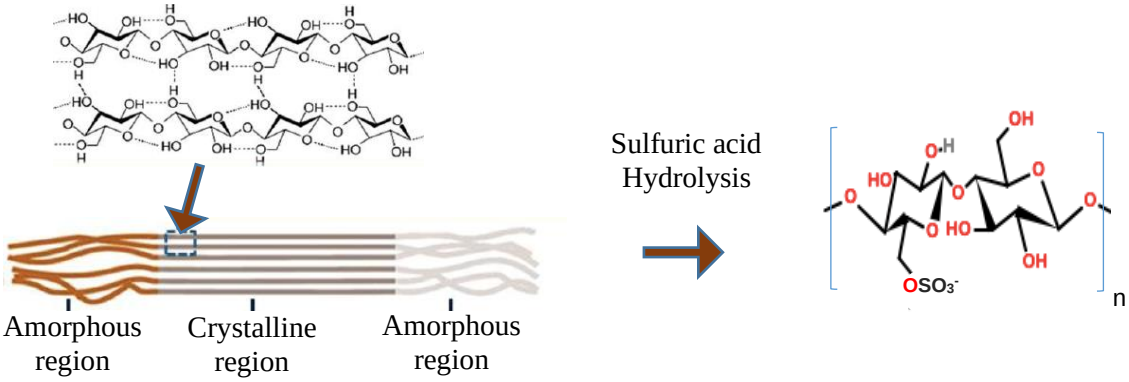

Figure 2 Schematic showing the interaction between cellulose molecular chains within the crystalline regions, sulfuric acid hydrolysis on CNC, and nucleophile substitution (OSO_3^-).[48]

The surface of CNC is highly tuneable, due to the rich availability of hydroxyl groups (-OH) groups. Each pyranose ring unit of CNC has one primary and two secondary -OH groups which provide an ample number of sites to introduce numerous functionalities. This property comes in handy to develop advanced materials for application in diverse fields. For example, CNC

resulting from sulfuric acid hydrolysis CNC readily disperse in water and other polar media due to the presence of negatively charged sulfate half ester groups on the surface creating electrostatic repulsion between CNC.[49-53]

2.3. Biosensors

Biosensors are analytical devices that can detect the presence of specific biomolecules in a given system via physical or chemical transduction. Predominantly, a biosensor houses a biological material or its mimic (e.g., model antibodies) that is integrated within a transducer (Figure 3) which can be piezoelectric, optical, electrochemical, thermometric, or magnetic.[54, 55] The transducer generates an electronic signal corresponding to the analyte(s) of interest. Therefore, a biosensor essentially has a bio-receptor (sensory element), transducing element, and readout modality (physical output) relating the desired analyte's quantification. And they have numerous applications in various fields as presented in Figure 4.

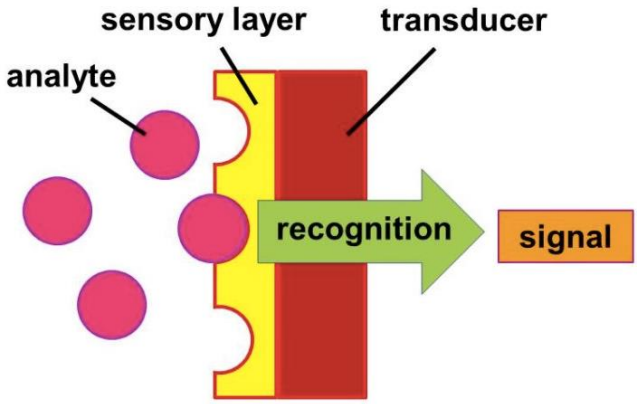

Figure 3 Biosensor elements.[56]

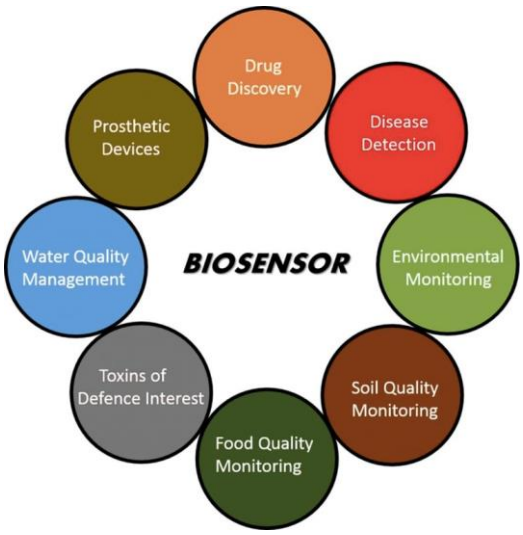

Figure 4 Major application domains of biosensors.[57]

2.3.1. POC biosensing platform

POC biosensing systems facilitate access to advanced technologies available in major healthcare centers to a greater population pool. They can be particularly advantageous to the patients whose conditions warrant constant screening or close surveillance of disease recurrence; and who live in remote areas with a very few or no healthcare providers in the nearest vicinity. It is desirable that POC technologies are low-cost and large-scale in their implementation.[55] They can play a very crucial role in the early diagnosis of a disease to reduce the risk of disease progression to a non-curable, irreversible stage. This is explicitly true for diseases such as cancer. POC biosensor systems can investigate the clinical samples of patients for the presence of several target biomarkers in various habitats, such as clinical laboratories, doctors' offices, etc.

2.3.2. Classification of biosensors

The biosensors classification based on three different categories is presented in the chart (Figure 5). The encircled areas in the figure correspond to the techniques explored in this current research. There are numerous transduction mechanisms used in biosensors today which can convert the signal in one form of energy to a signal in another[58] form that is quantifiable. Among the various transduction mechanisms, the electrical and optical biosensors are the most widely known and researched in biomolecules detection. However, they do have some drawbacks, especially in the point-of-care diagnostics application perspective.

Electrical biosensors necessitate fabrication with very high complexities and limited to developing sensors only in particular sizes and geometries with fewer materials. Optical sensors are known for their high sensitivity detection of the biological target analytes. The optical sensors have an optical transducer element which detects the target analyte. Unlike electrical sensors, optical sensing mechanisms are very flexible in their application enabling a wide scope for various materials that can be used. However, this scheme requires high precision and alignment that comes at a huge cost. There could be thermal management issues as well which may lead to faulty readings. Therefore, there has been a growing demand for biosensor research to look for alternatives especially in the field of POC diagnostics. In the past decade, mechanical and nanomechanical biosensors have gained popularity as the research community realized the mechanical nature of many biological processes.

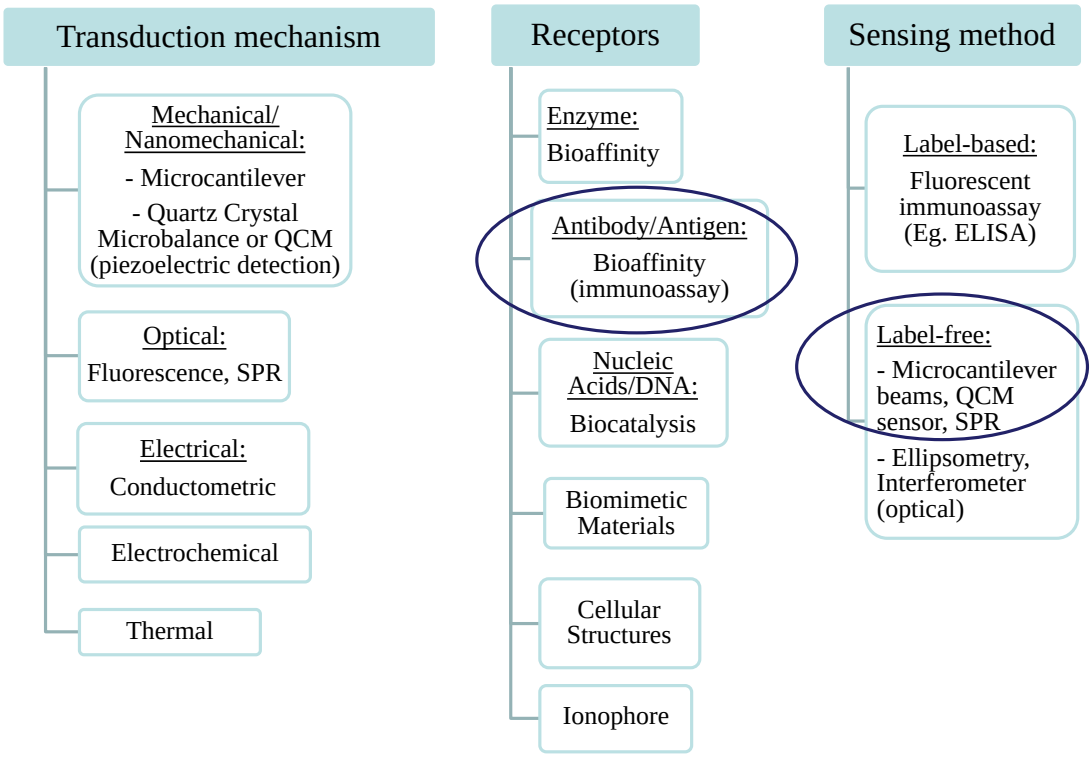

Figure 5 Classification of biosensors based on transduction mechanisms, receptors and sensing strategies.

Several nanomechanical tools have been invented to sense and actuate on biomolecular systems. Among mechanical biosensors, quartz crystal microbalance has become one of the most widely researched and proven technique.[59-61] Such devices are based on piezoelectric quartz crystal resonators and enable the direct measurement of the target analyte attachment to the bio-recognition element by the changes in voltage as a result of crystal deformation. Nanomechanical sensors are a branch of mechanical sensors and as the name suggests, they have at least one of their dimensions in the nanoscale (100 nm).[62-68] These emerged as a result of tremendous advances in the semiconductor industry. Nanomechanical biosensors are usually cantilever-shaped and arrays of hundreds of them can be conveniently produced by micro- and nanofabrication technologies. Nanomaterial based cantilevers have a thickness in the size range of the biomolecules which make them highly sensitive in detecting the mechanical and physical

properties of the adsorbed biomolecules layer. In addition, nanomaterials are being used in sensors including the microcantilever beams that have thicknesses and widths of a few microns and length on the order of 100 microns.

Nanomechanical biosensors exhibit flexible mechanisms and they can translate biomolecular interaction events into measurable displacements. These displacement deflections could be somewhere in the range of few angstroms to hundreds of nanometers and can be measured by various optical and electrical techniques. Among electrical techniques, piezoresistive detection is the most commonly used tool. A piezoresistive microcantilever uses a loop of piezoresistive material (silicon, polysilicon, germanium, etc.) which is implanted onto the cantilever surface. Any surface mass changes due to biomolecular reactions cause the cantilever to bend. This, in turn, causes stress in the piezo material that causes deflections (see Figure 6). Thus, the deflections can be translated into the change in its resistance by a Wheatstone circuit bridge.[65] The piezoresistive method of detection, though less sensitive (order of nanometers) was considered a surpassing tool for application in portable sensors. They are also more appropriate for use as wearable sensors for this very reason.

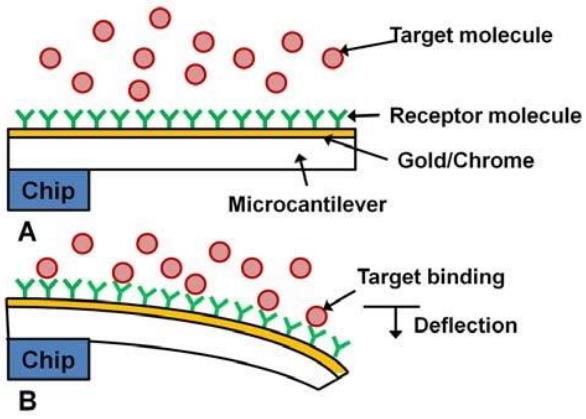

Figure 6 Microcantilever response: (A) initial state and (B) sensing state.[5]

Another biosensor classification is based on two major strategies for the detection of biomarkers: label-based and label-free detection. Label based detection systems mostly rely on the optical transduction mechanisms and mainly on fluorescent labeling methods. Fluorescent dyes are attached to the bio-recognition elements or biomarkers. The concentration of biomarker adsorbed is determined either by labeling of the attached biomarkers or unbound bio-recognition sites. One common and best example of label-based detection technique is enzyme-linked immunosorbent assay (ELISA), which can detect the analyte concentrations in the range of few femtomolars. The common labels/tags used are fluorescent dyes and radioisotopes. These methods are usually highly sensitive, selective with high spatial resolutions[69] as discussed earlier under optical methods. However, the labeling procedures are laborious and most often they alter the surface characteristics and therefore properties of the query molecules (bio-recognition elements) which make them unattractive. This along with their expensive nature makes then unfeasible in POC applications.[70, 71] On the other hand, label-free detection techniques depend merely on the measurement of an inherent physical property of the query molecules, such as mass (quartz crystal), stress, electrical (piezoelectric), optical properties (surface plasmons) etc. and enables sensitive detection of reactions or biomolecular interactions in real-time.[72-74] So, label-free detection techniques are highly preferred and possess the potential for rapid diagnosis in POC applications.

Finally, biosensor can also be classified based on the bio-receptors or bio-recognition elements as they form major components in the making of a biosensor. There are a countless number of bio-receptors and the most common ones being the antibodies, enzymes, and nucleic acids such as DNA. The bio-receptors can exhibit either bio-affinity type or biocatalytic type reception.[75] In the bio-affinity based reception, the receptor does not interact/modify the target

material, antibodies come under this category. Whereas the enzymes or similar receptors catalyze the immobilization reaction and thus come under the biocatalytic type.

2.3.3. BioMEMS based on label-free detection

BioMEMS (Biological Micro-Electro-Mechanical Systems) is a category of miniature biosensor devices which are developed using micro/nano-scale fabrication. This broad area is considered a separate category in biosensor classification. They are useful for performing numerous functions such as sensitive detection, immobilization, purification, growth, and manipulation of analytes.[76-78] The growing boom in BioMEMS for biosensing applications is attributed to their small size and facile construction. Hence, they are ideally suited for application in POC lab-on-a-chip biosensing systems that are capable of multi-analyte detection in humans or in the environment. The design and fabrication modalities of BioMEMS used in diagnostics depend on the nature of the application it caters to. BioMEMS have their own set of challenges for application in diagnosis, sensing, and detection namely

- Lack of technologies to develop and characterize the BioMEMS with lower detection limits (few femtomoles per ml), high sensitivity, and specificity[79]
- Reproducibility
- Accurate identification of chemical and biological analytes
- Biocompatibility issues - since the wearable POC biosensors directly contact the human body, it is necessary to ensure there will not be any detrimental effects on the patients
- Rapid degradation of sensor materials with time
- Failure of biocompatible sensors due to biofouling and limited lifetime of immobilized proteins.

The most commonly employed BioMEMS sensors using label-free detection techniques are constructed based on micro-/nano-scale fabrication. Some examples of the techniques are as follows: surface plasmon resonance (SPR), microcantilevers, quartz crystal microbalance (QCM), etc.

2.4. QCM-D

QCM-D is a real-time, nanoscale technique for probing various surface phenomena such as a thin film formation, molecular interactions and reactions. QCM-D uses a thin quartz disc, a piezoelectric material which is sandwiched between a pair of electrodes. An alternating voltage can be applied to excite this crystal so that it oscillates at its resonance frequency. The resonance frequency could be related to the total oscillating mass of the sensor and surface adhering layers. Whenever there is mass adsorption on the surface (e.g. antibody-antigen binding) as a result of surface interactions and bonding, the frequency decreases (Figure 7).[80, 81] For a rigid and thin film formation, the decrease in frequency is proportional to the mass addition on the film. The particular nature of the film and its structural properties can be determined from the dissipation shifts. The dissipation is measured based on the time of oscillation of the crystal after the power is disconnected. A decrease in dissipation is usually accompanied by the formation of a rigid, cross-linking layer whereas the increase denotes a soft layer formation. As compared to QCM, QCM-D generates more accurate and faster results.

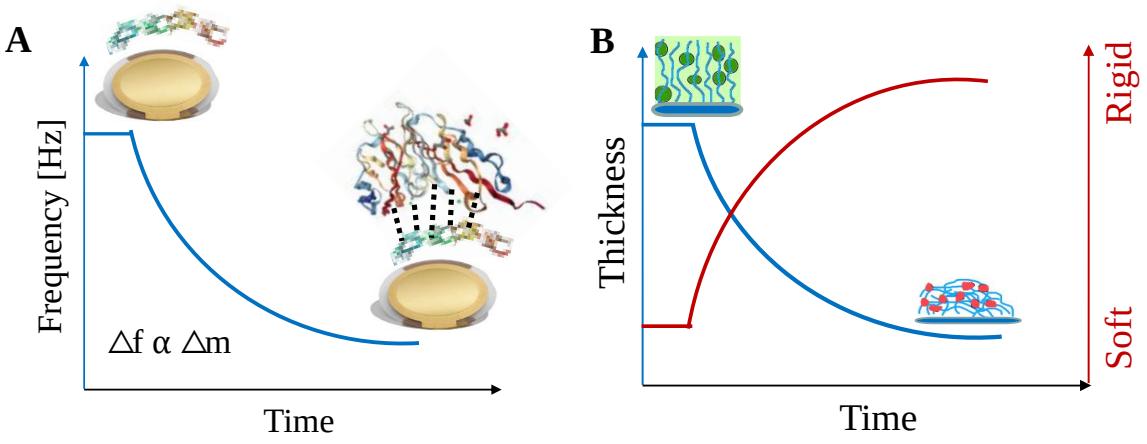

Figure 7 An illustration of A. Antibody-antigen binding in QCM-D resulting in frequency decrease, B. An upward shift in dissipation corresponds to rigid layer formation and vice-versa.

Sauerbrey determined a quantitative relationship for rigid layers (D > 0), uniformly distributed on the surface and with lower values of mass than the mass of the crystal with the following equation (Equation 1):

$$\Delta m = C * \Delta f * n^{-1} \quad (1)$$

Where, C is -17.7 ng/cm^2 and is a constant for 5 MHz crystals, that depends on the density and viscosity of the silica crystal, Δf is the change of frequency, and n is the overtone number. However, most of the polymeric systems do not generate a rigid layer, then this equation underestimates the adsorbed mass. For these cases, some other models have been generated to address the changes of mass, such as Voigt's and Maxwell's that considered the density, dynamic and static viscosity of the adsorbed materials as well as that of the crystal.[82]

The dissipation factor is related to the viscoelastic properties of the layers formed on the crystal, as it translates the relationship of energy dissipation from the sensor to the fluid and the energy stored (Equation 2). It is inversely proportional to the decay time constant (τ) and the resonant frequency (f) as shown in Equation 3.[82]

$$D = \frac{E_{dissipated}}{2\pi E_{stored}} \quad (2)$$

$$D = \frac{1}{\pi f \tau} \quad (3)$$

If the generated film is viscoelastic instead of a rigid surface, energy would be dissipated due to the oscillation of the layer. Thus, more energy is lost, and longer decay times are present which translates to an increment in the D factor. When the surface is rigid, more energy is stored and decrements in the D-factor are observable.[83] In Figure 8, these behaviors are presented, the change is frequency is proportional to the mass that is adsorbed on the surface, while this change on rigidity also carries an increase in the dissipation measurement as more elastic behavior is presented by the surface.

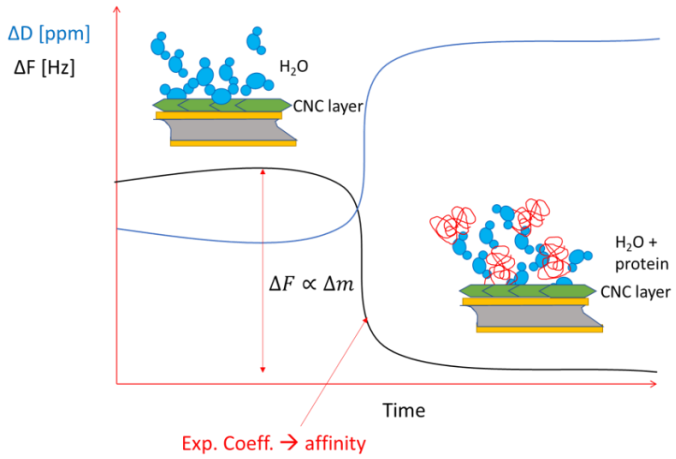

Figure 8 Scheme of formation of layers on QCM-D and graph behavior (art by Diego G Maldonado from an unpublished manuscript).

2.5. Antibody-antigen interaction

An antibody is a protein with a unique structure that enables it to bind specifically to its corresponding antigen. They are produced by white blood cells as an immune response to fight

infection. They have complex molecular structures and comprised of hundreds of individual amino acids arranged in a highly ordered sequence. Biosensors that depend on antigen-antibody binding are called immunosensors; one of the best well known is enzyme linked immunosorbent assay (ELISA).[84] The biological function of antibodies is to bind to the disease-causing pathogens and wipe them off from our body. Usually, an antibody recognizes a very small portion on the surface of a large antigen molecule and attaches to it by a variety of noncovalent forces such as hydrophobic, electrostatic, hydrogen bonds, etc. Most of the time, the antigens that elicit such an immune response in the body proteins or polysaccharides. This conformational structure on the antigen that is recognized by an antibody is called an epitope. The pathogens have polysaccharide coats, for example, antibodies produced against viruses recognize viral coat proteins. The epitope consists of amino acid sequences from the different parts of the protein polypeptide chain that are grouped together as a result of protein folding. Such epitopes are called discontinuous epitopes. The antibodies recognize such discontinuous epitopes and bind to their peptide fragments. An antigen molecule that can provoke an adaptive immune response upon injection into a living body is called an immunogen. Only proteins can be recognized by the T-cells (white blood cells) and therefore proteins alone are considered fully immunogenic. And the Specificity of an antibody is determined by its capability to distinguish its immunogen from the other antigens.[85] Cross-reactivity occurs when an antibody recognizes and binds to other antigens with competing affinities as its immunogens.

2.5.1. Monoclonal antibodies

Monoclonal antibodies are produced under highly controlled environment from animals such as mice. Mice are first made immune to an antigen and given an intravenous

booster injection three days before they are killed, to facilitate some time for the spleen cells to produce considerable amounts of that specific antibody (Figure 9). During culture, the spleen cells die in a few days. In order to make the production continuous, they are fused with immortal myeloma cells with support of polyethylene glycol. The produced hybrid cell line is called hybridoma. Each hybridoma cell is screened to identify the cells that make antibody of the desired specificity and they are cloned (grown from a single antibody-producing cell) in bulk culture. Since each hybridoma cell is derived from a single cell, the same antibody molecule is produced by all, which then becomes a monoclonal antibody.[86, 87] A medium made of hypoxanthine-aminopterin-thymidine (HAT) ensures that the myeloma cells are not secreting antibody themselves. This is achieved because HAT is sensitive to an enzyme called hypoxanthine: guanine phosphoribosyl transferase (HGPRT) which is a gene contributed by the spleen cells and only these can survive in HAT. As a result, the unfused myeloma spleen cells die in the HAT medium. Further, the monoclonal antibodies can be labeled with fluorescent probes to enable for their application in fluorescent immunoassays.

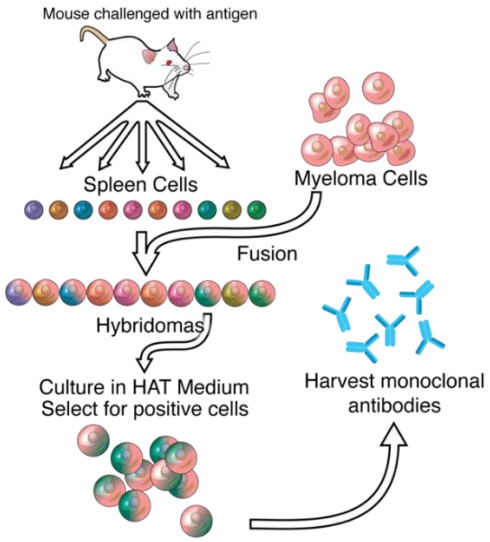

Figure 9 Methodology for the production of monoclonal antibodies.[88]

Typically, the antibodies are stored in a buffer composed of bovine serum albumin (BSA), glycerol, and sodium azide to ensure stability. Buffers are fundamental in the biological systems as a natural occurring ionic force is always present. The weak and strong interactions of ions, mainly hydrogen concentrations (pH) are primordial to any biological process as the integrity of hydrophilic molecules such as proteins. Buffers should simulate the environment in which the process naturally occurs. Phosphate buffered saline (PBS) is the one such standard buffer for blood plasma and interstitial space simulation. The pH of PBS is normally between 6.8 and 7.4, and the absence of interactive ions such as ammonium, sulfates or carboxyl groups in any of the components, make it resistant to enzymatic degradation and absorption of UV or visible light.[89, 90]

2.6. CNC in QCM-D biosensing

In the past decade, there has been a significant amount of interest on piezo-based mechanical biosensors in cancer research. Su *et al.* (2013)[91] has developed a novel piezoelectric biosensor using lead titanate zirconate (PZT) ceramic resonator and successfully detected target cancer biomarkers chosen for detection are AFP and PSA. The device was reported to have a sensitivity of 0.25 ng/ml, within 30 min time using a small amount of sample (1 μl). Ding *et al.* (2007)[92] used an assembly of gold nanoparticles on nano-hydroxyapatite for the interface design of QCM immunosensor, on which the antibodies were immobilized for the detection of AFP in the concentration range of 15.3-600 ng ml^{-1}. Kosaka *et al.* (2014)[93] developed silicon cantilevers and demonstrated both plasmonic and nanomechanical detection of the cancer biomarkers CEA and PSA (detection limit: 10^{-16} g ml^{-1}). Etayash *et al.* (2015)[94] developed a microcantilever functionalized with a breast cancer-specific peptide and showed significant deflection on cancer tumor cell (MCF7 and MDA-MB-231). Similarly, there have been multiple studies using the

microcantilevers and QCM resonators to detect target analytes.[95-101] Several researchers have also demonstrated the use of promising nanoparticles in biosensing such as graphene, gold, titanium, etc.[102-111] Very few studies in the past have addressed cancer detection using CNC based sensors and none utilizing the surface-functionalized CNC obtained from the facile APTES-GA chemistry. There is also a significant gap in terms of exploring the promising piezoelectric based QCM-D technique for the detection of cancer biomarkers namely CEA, AFP and PSA by performing a multi-step reaction on the CNC. Practically, QCM-D can be more relevant biomarker sensing tool in case of such multi-step reactions due to its real-time sensitivity. In addition to the biomarker detection, QCM-D was also used to confirm the successful antibody immobilization on the modified CNC surfaces.

Chapter 3. Experimental

3.1. Materials and chemicals

An 11.3 wt. % aqueous CNC suspension (batch 2018-FPL-CNC-126) with Na^+ as the counter ion was produced by the U.S. Forest Products Laboratory (FPL) and supplied by the University of Maine (USA) with a specified sulfur content of 0.58 wt. %. Based on polarized optical microscopy, the onset of biphasic (Φ_I) and liquid crystalline (Φ_{LC}) regimes was observed around 3.52 % and 7.1 % respectively. Characterization of electrolytic properties of the dispersions was obtained on the stock gel dispersion using a VWR International (Radnor, Pennsylvania) Traceable Expanded Range Conductivity Meter, yielding conductivity of 1055 µS/cm, pH: 6.28 and Charge density: 39.9 µeq/g. Based on atomic force microscopy (AFM) measurements of the air-dried CNC samples, the size average CNC length was 165 nm with a standard deviation (σ) of 48 nm, the average width was 29 nm (σ = 5.6 nm), and the average height was 5 nm (σ = 2 nm). The width measurements included blind tip estimation using Gwyddion. Conductometric titration with 10 mM sodium hydroxide showed there was 180 mmol of R-SO_3H per kg of CNC. A few of the experiments were conducted using CNC suspension (batch 2016-FPL-CNC-098) which was also obtained from the University of Maine in 2016 and all the various properties were described in Pospisil *et al*., 2018.[112] For a trial, CNC spray-dried powder (batch 2012-FPL-CNC-051) with a specified sulfur content of 1.05 wt. %

APTES [$H_2N\ (CH_2)_3Si\ (OC_2H_5)_3$], ≥ 98% and GA ($C_5H_6O_3$), 95% were obtained from Sigma-Aldrich, used without further purification. Glacial acetic acid ($C_2H_4O_2$) and ethanol (C_2H_6O) were purchased from VWR (USA) and used without further purification. CEA (3G7) Monoclonal Antibody, Alexa Fluor® 555 Conjugated (Catalog # bsm-4792M-A555), AFP (A2)

Monoclonal Antibody, Alexa Fluor® 350 Conjugated (Catalog # bsm-1621M-A350), and PSA (Pa3) Monoclonal Antibody, Alexa Fluor® 488 Conjugated (Catalog # bsm-1625M-A488) of concentration 1 µg/µl were obtained from Bioss, USA. CEA (#30002100; Concentration: 1-5 mg/mL; Purity: >95%), AFP (#13752600; Concentration: 2-5 mg/mL; Purity: >95%), Native Human PSA (#7820-0504; Concentration: 1 mg/mL; Purity: >96 %) were procured from Bio-Rad (USA). Phosphate-buffered saline (PBS) with a pH of 7.4 was synthesized by dissolving 137 mM Sodium chloride (2.015 g), 2.7 mM potassium chloride (0.055 g), 10 mM disodium phosphate (0.287 g) and 1.76 mM monopotassium phosphate (0.050 g) in 250 ml water. If required, pH was adjusted with 0.1 M NaOH (sodium hydroxide) or HCl (hydrochloric acid).

3.2. Characterization techniques

3.2.1. Optical Microscopy

A Nikon (Melville, NY), Eclipse 80i microscope with imaging workstation and Nikon Elements, was used to capture all of the optical microscopy images using 4X/0.1, 10X/0.30 and 20X/0.45 (magnification/numerical aperture) LU Plan Fluor objectives. The camera used was a Nikon DS-Ri2. Transmitted cross-polarized (CP) and non-cross polarized (non-CP) OM techniques were used as a preliminary characterization to investigate the microscale artifacts, defects, dispersion state and aggregation in the CNC-APTES-W, CNC-APTES-E, CNC-APTES-E2, CNC-APTES-P, CNC-APTES-R, CNC-GA-R, and CNC-aCEA-R dispersions.

Long-chain polymers and liquid crystalline materials such as CNC exhibit a positive uniaxial birefringence, which is also called optical anisotropy. Sheared or ordered solid samples can maximize this anisotropy. CNC have two distinct refractive indices along parallel and perpendicular directions to their long axis. Based on the ordering of their long axes, CNC can split

the polarized light in these two directions. The light from these two directions, due to the phase difference tend to interfere with each other (constructive or destructive). When they are passed through another polarizer, birefringence colors appear. The birefringence is the difference between these refractive indexes of light polarized parallel (extraordinary) and perpendicular (ordinary) to the optical axis, $\Delta n = n_e - n_o$, where n_e and n_o are the refractive indexes of the extraordinary light and ordinary light. The birefringence of cellulose ranges from 0.045 to 0.062 depending on the source; for cellulose derived from cotton, the range of n_e was reported in the range of 1.576–1.595 and n_o in the range of 1.527–1.534.[113, 114] Birefringence induced interference colors depend on ordering, retardation of the elliptically polarized lights, and thickness of the sample.[15] The CNC-APTES-P was investigated for the presence of birefringence property by rotating the stage at different angles using cross-polarized light.

To confirm the successful antibody immobilization, fluorescence microscopy imaging was performed on the samples CNC-GA-R (non-labeled) and CNC-aCEA-R (labeled). The fluorescence images were acquired using an inverted Nikon Eclipse Ti microscope fitted with an Andor Luca S camera. The fluorescence images were analyzed using ImageJ software, version 1.48q (NIH) in order to generate the area, mean intensity or gray values. The fluorescence intensities were measured using the TRITC filter before and after the antibody CEA immobilization.

3.2.2. SEM/EDS Analysis

An environmental SEM (Zeiss EVO 50, Carl Zeiss Meditec, Oberkochen, Germany) was used to examine the morphology and size of CNC-APTES-W dispersions. The samples were drop cast on a small piece of silicon wafer and attached to an SEM stub with conductive carbon tape.

When drop-casting, in order to ensure uniform drying of the layers and avoid coffee ring formation, the silicon substrate was placed on a preheated hot plate at 80 °C. The sample was then dropped using a glass stirring rod by dipping sufficient amounts for once and repetitive dropping was avoided. The sample was allowed to vacuum dry for at least three hours before the SEM analysis. Then the stub was sputter-coated with gold using a sputter coat device (EMS 550x, Carl Zeiss Meditec, Oberkochen, Germany). An EDS analysis was also conducted to know the atomic composition using an Inca EDS system which is configured with this SEM. All the SEM images from secondary electrons were taken at 2000x magnification, 20 kV EHT (electron high tension), and a working distance of 8.5 mm. For higher magnification purpose, a JEOL (Peabody, MA) JSM-7000F SEM was used for analysis with 20 kV EHT and a working distance of 8.5 mm for a range of magnifications from 5000x until 75000x. The sample CNC-APTES-E2 was prepared for imaging by using the same method as discussed earlier for the CNC-APTES-W dispersions on a Si wafer piece and attached to a suitable SEM stub via carbon tape. Prior to SEM imaging, the gold sputtering was performed on the prepared sample stub using a PELCOSC-6 SPU system run by argon with 0.08 mbar plasma sputter pressure.

3.2.3. Water contact angle measurements

A ramé-hart Instrument Co. (Succasunna, NJ, Model 200-00-115) standard goniometer with a measurement reproducibility of ±2° was used to measure static water contact angle. The setup was equipped with a CCD digital camera, a backlight source, movable sample stage, and a water injection syringe calibrated to drop the liquid in a controlled manner (4 μL) on the solid surface. The static water contact angle was measured for the CNC-APTES-E2 shear cast film on a Si wafer in order to determine the wettability. The hydrophobicity of the film was judged based

on the water contact angle values taken after 30 seconds. From the Figure 10, the contact angle θ_C is the angle measured between the wetted surface and sessile droplet; γ_{lv}, γ_{sl}, and γ_{sv} are liquid-vapor, solid-liquid, and solid-vapor interfacial tensions, respectively. For a water droplet, θ_C values above 90° are considered hydrophobic in nature. The analysis of the droplet image and contact angles were done using DROP image software.

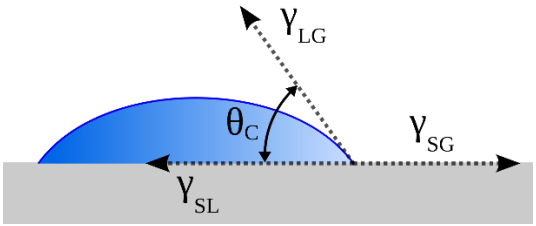

Figure 10 Sessile drop technique illustration with a liquid droplet partially wetting a solid substrate.[115, 116]

3.2.4. TGA–FTIR

Thermal stability analyses used a TA Instruments (New Castle, DE) Q50 thermal gravimetric analyzer (TGA) at 10 °C/min interfaced with a Thermo Scientific (Waltham, MA) Nicolet iS 10 Fourier Transform Infrared Spectrometer (FTIR) equipped with an attenuated total reflectance (ATR) universal accessory. The transfer line which is glass-lined and made of stainless-steel connects directly to the TGA furnace, enabling an inert passage of evolved gases (decomposition products) into the gas cell for IR detection. The transfer line and the gas cell were kept at 225 °C and 250 °C respectively to prevent gas condensation. The evolved gases from sample degradation pass through the TGA-IR interface transfer line and reach the FTIR. IR spectra were recorded in the spectral range of 4000-400 cm^{-1} with a 4 cm^{-1} resolution and after 16 scans for each sample. Two to four spectra were obtained for each sample. The solid masses of the

samples ranging around 8-20 mg were used. The TGA Q-series software was used to set the conditions of the experiments. For all the samples, the balance gas used was argon at a flow rate 10 ml/min and for the sample gas either air or argon was used at a flow rate of 90 ml/min. An external event to start FTIR acquisition was triggered after the isothermal hold at 120 °C; this hold was intended to remove residual moisture. The temperature was then ramped at 10 °C/min to 700 °C followed by a 10 minutes isothermal hold. OMNIC software was used to collect the FTIR Gram-Schmidt plot data and the associated spectra for all the times (starting from the external event until 700 °C). This software was to extract the FTIR raw data as well whereas a software called TA Universal Analysis was used to extract the TGA data. The dispersions namely, CNC, CNC-APTES, CNC-GA, CNC-antiCEA, CNC-antiAFP, CNC-antiPSA, CNC-CEA, CNC-AFP, and CNC-PSA were all investigated for their thermal stability, and mass losses as a function of temperature. The linked FTIR spectra was used to identify the evolution of gaseous vapors as the sample was heated in TGA.

In addition to TGA-FTIR analysis, ATR-IR spectroscopy was performed on CNC, CNC-APTES, CNC-GA and CNC-antiCEA samples to confirm that the proposed chemistry was working. This served as a starting point for further characterizations. This technique was also used to compare the film modified and dispersion modified CNC-APTES. The ATR-IR spectra were also taken for the two different batches of CNC-APTES-W to check for the reproducibility and understand the functional groups present in the resulting product. Further, this technique was used to compare the functionalities present in CNC-APTES-W and CNC-APTES-E.

3.2.5. QCM-D

Gold-coated crystal Qsensors (QSX 301 Gold) were obtained from Biolin Scientific. They were placed in Novascan PSD Series Digital UV Ozone System (Iowa, US) for 30 min to eliminate dust and activate the surface. Sensors were immersed in a 0.1% wt. polyethyleneimine (PEI) solution that served as an anchoring solution. Then surfaces were prepared on a spin coater from Laurell technologies corporation (model WS-650MZ-23NPPB, Pennsylvania, US). Both film and dispersion modification reactions on CNC were analyzed in real-time for each step. For this, 180 µL of 0.1% wt. CNC (to follow film modification reactions) or CNC-antibody dispersions (for dispersion modification reactions) were used at 3000 rpm for 1 min. In the case of CNC-antibody dispersions, the sensors were left to stabilize in PBS overnight before QCM-D. This step also ensured to check if the coating was strong enough and not detaching from the sensor surface. In the other case, i.e. for the CNC coated sensors, all the reactions were performed immediately such as APTES reaction or even GA and antibody reactions in a different study before introducing them into QCM-D for the respective antigen detection reactions. The APTES reaction on the CNC sensor was always performed outside of the QCM-D, as the APTES reaction involves using ethanol as a solvent which is not a compatible material with the tubing used on the QCM-D.

The capture of the respective antigen was then followed with a QSense Analyzer from Biolin Scientific (Västra Frölunda, Sweden). Measurements were carried out at 25 °C with a constant flow of 50 µL/min. Data were collected in all the overtones, however only the third overtone is presented on sensorgrams to facilitate analysis. Mass was calculated using the Composite Sauerbrey model (which averages all overtones calculations), using DFind Software from Biolin Scientific (Västra Frölunda, Sweden).

3.2.6. Fluorescence Anisotropy (FA) and microscopy

To confirm the successful antigen-binding reaction with the antibody immobilized CNC, FA was used. This is because there was no observed change in the fluorescence intensities between the antibody immobilized CNC (labeled) and the antigen-antibody immobilized dispersions. It could be possible that both of these samples have fluorophores in them with almost similar intensities. A labeled sample is the molecule to which the fluorophore is attached which in this case is the antibody immobilized CNC. In FA, a labeled sample with a group of randomly oriented fluorophores is excited with vertically polarized light of an appropriate wavelength. Only the molecules with fluorophores oriented within a particular range of angles to the applied direction of polarization will get excited.[117-119] The fundamental principle of FA is that the macromolecular tumbling time and fluorescence lifetime of fluorophores match.[120] Thus, when an antigen binds to the antibody immobilized CNC, the tumbling or rotational mobility of the overall molecule becomes low. So, if they do not move, the fluorophores emit light in the same direction as the direction of polarization i.e. vertical. Therefore, the measured emission intensity in the vertical direction will be more than the horizontal direction as compared to the labeled sample. The labeled sample has relatively higher mobility which means more tumbling of the molecules/fluorophores. The FA is defined in Equation (4):

$$\text{Anisotropy } (r) = (I_{VV}-GI_{VH})/(I_{VV}+2I_{VH}) \quad (4)$$

Where, I_{VV} and I_{VH} are the fluorescence intensities of the vertical and horizontal components, respectively. The $2I_{VH}$ in the denominator is because the mobility of a fluorophore will be the same in either of the perpendicular directions, so the perpendicular components are assumed to be equal. If the antigen binds, the anisotropy should increase because of the low

tumbling, which implies that I_{VV} (antigen immobilized CNC) > I_{VV} (antibody immobilized CNC). And G is the instrument sensitivity ratio towards vertically and horizontally polarized light. It is measured by the instrument by exciting the sample using horizontally polarized light and subsequently measuring the horizontal and vertical components of the emission intensity (HH and HV). Generally, G is calculated as the ratio between the measured total intensities (counts) in each channel or $G = (I_{HV}/I_{HH})$.

Anisotropic fluorescence data were collected at an excitation wavelength of 555 nm with an emission wavelength of 580 nm for all the samples using CNC-antiCEA, which corresponds to its conjugated fluorescent dye Alexa Fluor 555. Similarly, the excitation and emission wavelengths were set to 346 nm and 442 nm for the CNC-antiAFP samples; 490 nm and 525 nm for the CNC-antiPSA samples to probe the successful antibody immobilization onto CNC-GA and the ultimate antibody-antigen binding. All the washed/centrifuged samples were directly diluted 10 times in PBS and dispersed uniformly via vortex mixing before the analysis. The concentrations were within the range of 0.5-1 wt. %. The cuvette used for the emission fluorescence testing was a 400 µL cylindrical cuvette made of polycarbonate with a 1 cm path length. The excitation and emission slits were each maintained at 5 nm and 15 nm respectively. The integration time was set to 1 second and the G-factor was calculated separately for each sample and the values were in the range of 0.2 to 1.3. The G-factor was close to 1 in most cases with a deviation of ±0.3. In very few cases the deviation was ±0.7 from 1. A total of 45 anisotropy measurements were performed with a 5 mm path length along with a few repetitive runs. After antibody immobilization, the exposure of the samples to light and subsequent quenching was avoided by wrapping the samples with aluminum foil and covering them with an opaque box while washing, diluting, and measurements. To avoid

quenching while taking measurements of multiple loads on a single sample, the sample was distributed into multiple vials. Before taking the anisotropy measurements, the fluorescence intensities were measured for all of the dispersions starting with the blank PBS solution, CNC-GA, CNC-antiCEA, CNC-antiAFP, CNC-antiPSA, CNC-CEA, CNC-AFP, and CNC-PSA. This was mainly to confirm if there was an upward shift in intensities for the antibody immobilized samples as compared to CNC-GA. After confirmation, the anisotropy measurements were taken for the antibody immobilized and finally, antigen immobilized CNC dispersions. In addition, cross-reactivity behaviors of the CNC-antibody dispersion when reacted with other antigens was also tested using FA.

A Perkin-Elmer (Waltham, MA) LS 55 Luminescence Spectrometer was also used for fluorescence intensity measurements on the CNC-GA-R, and CNC-aCEA-R. Emission spectra were taken at room temperature scanning from 300 to 500 nm with a 0.5 nm resolution and a scan rate of 500 nm/min with an incident angle of 90°.

Chapter 4. Results and Discussion

The first attempt at surface modification of CNC with APTES in dispersion resulted in substantial aggregation. This is believed due to be due to cross-linking of CNC by the APTES. After multiple trials, the reaction conditions were identified that resolved the aggregation issue was resolved to a considerable extent. All these reaction trials are discussed comprehensively in the following sections. In each of these trials, at least one parameter was varied such as the form of the CNC (powder and suspension), the concentration of CNC, type of solvent etc.

4.1. APTES modification on CNC – Methodology 1

This procedure was adapted from Khanjanzadeh *et al.* (2018).[14] In this method, the CNC (batch 2016-FPL-CNC-098), APTES and water were added in a 1:5:100 w/v/v relation. First, 5 ml of APTES was added to 100 ml of water in a 300-ml beaker. This aqueous solution was adjusted to pH = 4 by adding glacial acetic acid under constant magnetic stirring. The CNC were then added into this solution and the reaction was allowed to proceed at ambient temperature for two hours. The resulting dispersion was washed twice by centrifugation (Beckman Coulter Allegra X-12R with a SX4750A rotor, 2100g, and 20-minute cycles). The centrifuged bottoms were collected and re-dispersed in water to give a concentration to approximately 3-4 wt. %. This sample was labeled as 'CNC-APTES-W B1'. A second batch was synthesized following the same procedure but with an additional bath sonication for 20-30 minutes that was performed towards the end (after re-dispersing the washed sample in water) and labeled as 'CNC-APTES-W B2'.

4.1.1. Characterization analysis of CNC-APTES-W samples

The dispersions of CNC-APTES-W from the two batches were dropped slowly onto two clean and dry microscope glass slides. They were then sealed with the cover slip and the dispersions were observed with cross-polarized light. Figures 11A and 11B show the areas of CNC-APTES-W B1 at magnifications 4x and 20x respectively, while the Figures 11C and 11D show the areas of CNC-APTES-W B2 at magnification 20x under the optical microscope.

Some of the aggregates in the CNC-APTES-W B1 were more than a 100 μm in diameter. In the CNC-APTES-W B2, the particle size distribution was in the range of 5-25 μm along with a very few 50-100 micron-sized aggregates. Hence, the aggregate sizes were small for the bath-sonicated dispersion i.e. CNC-APTES-W B2 as compared to CNC-APTES-W B1. The samples were further analyzed using SEM to visualize the particle size distribution and morphology. They were also scanned with EDS to confirm the elemental composition of different portions. Figure 12A and 12B correspond to the SEM images of the CNC-APTES-W B1 and CNC-APTES-W B2. The Figures 12C and 12D are their corresponding EDS spectra in the highlighted/marked regions (on the SEM images) with the elemental composition data. The aggregates in the CNC-APTES-W B2 were in the range of 1-50 μm and >250 μm for the CNC-APTES-W B1. In both of these dispersions, there were no traces of the element nitrogen (N); this could mean that the amino group introduction into CNC was unsuccessful. There were however significant amounts of silicon (Si) coming from the APTES reaction; the percentage increased a great deal in the CNC-APTES-W B2. This could be due to the reduced access to the areas in the CNC-APTES-W B1 as a result of aggregation. Since most of the aggregates were broken down in the CNC-APTES-W B2, the surfaces with the silane groups attached were supposed to have exposed better which might have resulted in the increase in the amounts of silane.

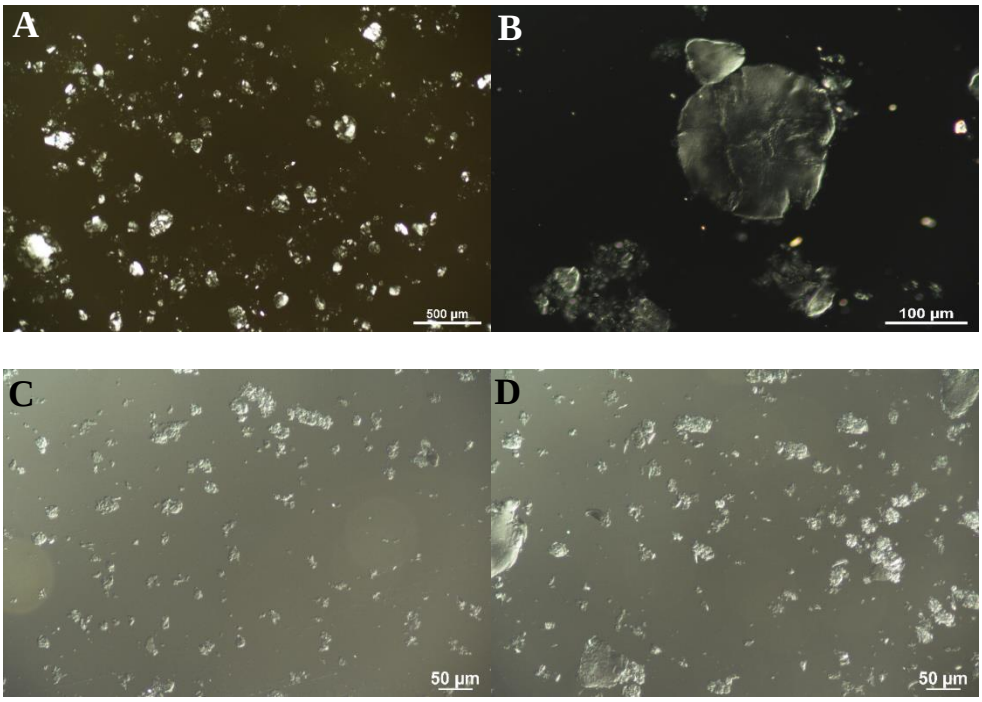

Figure 11 Cross polarized optical microscopy images at magnifications, A. 4x, and B. 20x, of CNC-APTES-W B1; C. & D. Both taken at 20x, for CNC-APTES-W B2.

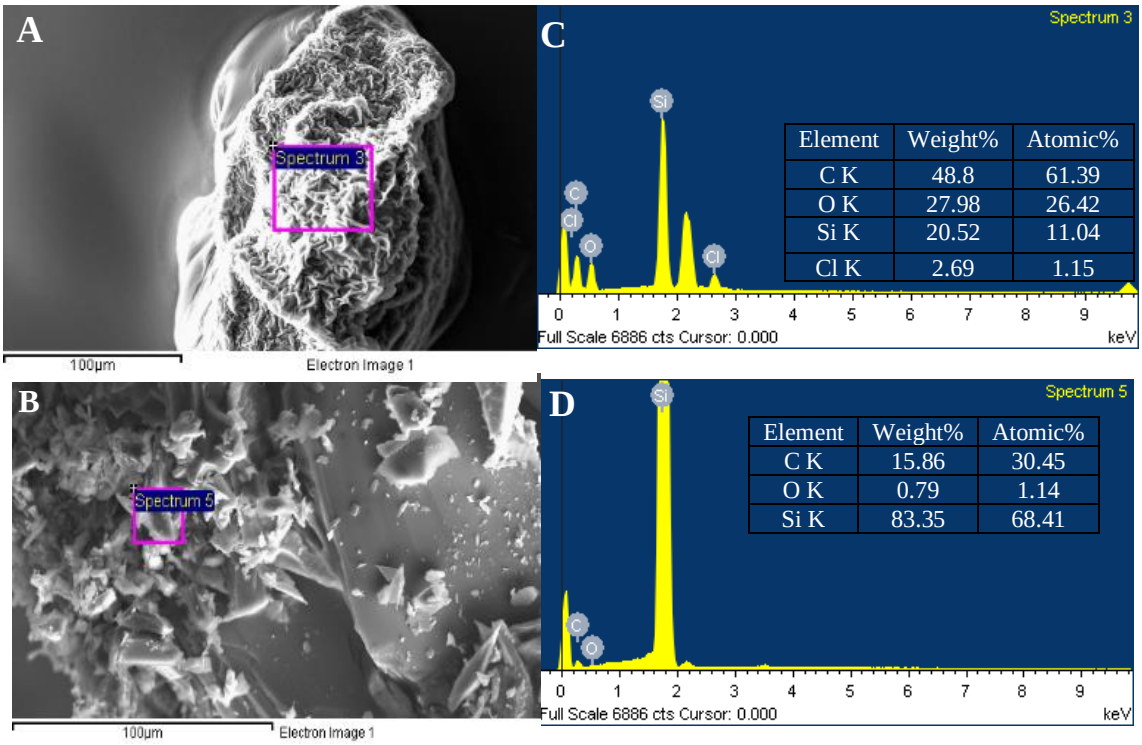

Figure 12 SEM images of CNC-APTES-W at concentrations, A. CNC-APTES-W B1, and B. CNC-APTES-W B2; C & D. Corresponding EDS spectra of marked regions on images A & B.

As a support for the results obtained from SEM-EDS, FTIR overlay was taken for two different batches of CNC-APTES-W (Figure 13). The dispersions were completely allowed to dry to form films before collecting the FTIR spectra. This analysis also served as a test to check the repeatability and reproducibility of CNC-APTES-W. N-H stretching vibrations due to the primary amines on the surface usually occur in the range of 3200-3400 cm^{-1} and the corresponding N-H bend occurs around 1640 and 1459 cm^{-1}. However, neither of the batches had absorption bands in this range, which indicates the absence of amino group. Instead, there was an alkyl C-H stretch around 3000 cm^{-1} combined with the strong, broad O-H stretching vibrations covering a wide range between 2800 and 3500 cm^{-1}. The corresponding C-H bending vibrations were observed in the range of 1350-1500 cm^{-1}. The sharp, strong peaks in the range of 1000-1100 cm^{-1} could be positively attributed to the C-O stretching vibrations of primary alcohol. Since there was no trace of the amino functionality, the NH_2 groups on the APTES were assumed to have been substituted by the OH groups and formed primary alcohol ($R\text{-}CH_2\text{-}OH$) as seen from the FTIR peaks due to C-O vibrations. There could also be few overlapping peaks due to the vibrations of Si-O-Si and Si-O-C bonds in the 1000-1100 cm^{-1} range as the EDS spectra showed considerable amounts of Si. Since, our main goal was to functionalize the CNC surface with amino groups, the formation of alkyl C-H groups or primary alcohols was totally undesirable. This approach of surface modification of CNC was therefore considered ineffective as evident from various characterizations and successive repetitions.

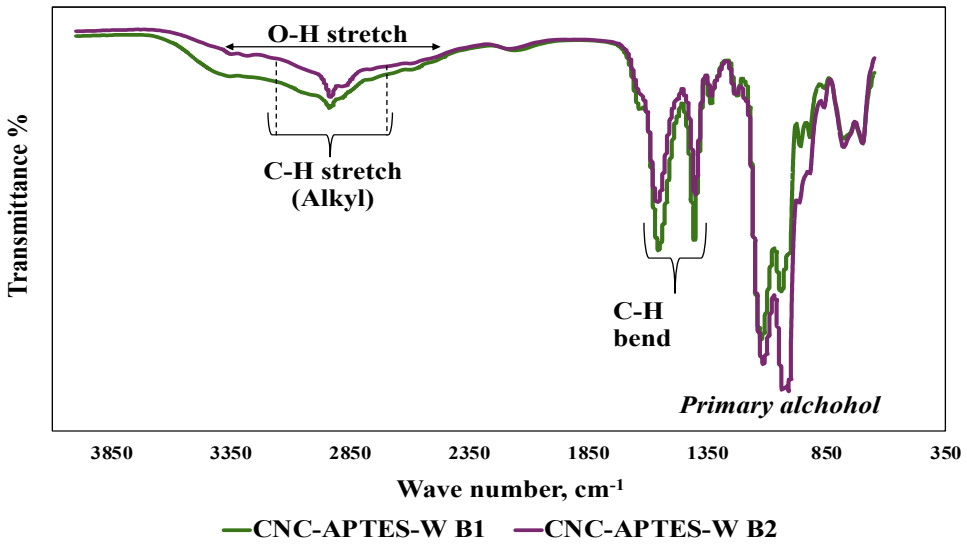

Figure 13 FTIR overlay of CNC-APTES-W samples from batch 1 and batch 2

4.2. APTES modification on CNC – Methodology-2

The method to produce surface-functionalized CNC using APTES in ethanol was adapted from Saha, 2018.[15] The procedure involved dispersing 8 g of 12 wt. % (7.8 vol.%) sulfonated CNC (batch 2016-FPL-CNC-098) in 10 g of ethanol and 1 mL of APTES in 10 mL of ethanol separately. The CNC-water-ethanol dispersion was introduced into a three-neck round bottom flask and placed in an oil bath under magnetic stirring on a hot plate. The first neck was sealed with a glass stopcock, the middle neck was connected to the condenser and the third neck was connected to the argon gas cylinder (flow should be minimum). The water flow to the condenser jacket, as well as the argon flow, was turned on. The oil bath temperature was set to 50 ^{0}C and the temperature probe was immersed in oil. A magnetic stirrer was also placed in the oil bath to distribute the temperature uniformly. Once the set temperature was reached, the APTES-ethanol solution was added through the first neck, and the reaction was allowed to take place for an hour. After the reaction, the flask was lifted above the oil bath to cool down to room temperature. The resulting product was labeled

as ‘CNC-APTES-E’. However, this method resulted in intense aggregation evidently due to the high concentrations of CNC. Hence, this method was slightly modified with respect to the amounts of CNC and ethanol to be used. In this modified procedure, 4 g of CNC was taken instead of 8g dispersed in 40 ml of ethanol. The rest of the details and conditions in the procedure were the same as the previous method. The resulting product was labeled as ‘CNC-APTES-E2’.

4.2.1. Characterization analysis on CNC-APTES-E and CNC-APTES-E2

The dispersions CNC-APTES-E and CNC-APTES-E2 were dropped carefully onto two clean and dry microscope glass slides. They were sealed and covered using a microscope cover slide. Figures 14 A and 14B show the cross-polarized optical microscopy images for the CNC-APTES-E and Figures 14 C and 14D correspond to CNC-APTES-E2. The aggregation in the CNC-APTES-E dispersion was very high ranging from 200-500 µm. Although the size of aggregates reduced to a greater extent, CNC-APTES-E2 cannot still be a good quality dispersion. It had a few 300 µm long aggregates while most of them were in the size range of 25-100 microns long. The aggregates in CNC-APTES-E2 have a cylindrical geometry instead of large nearly spherical entities in case of CNC-APTES-E. They also looked like flowing or oriented in one direction (Figure 14D) which might be because of some possible accidental shearing of the sample while dropping the cover slide on the sample.

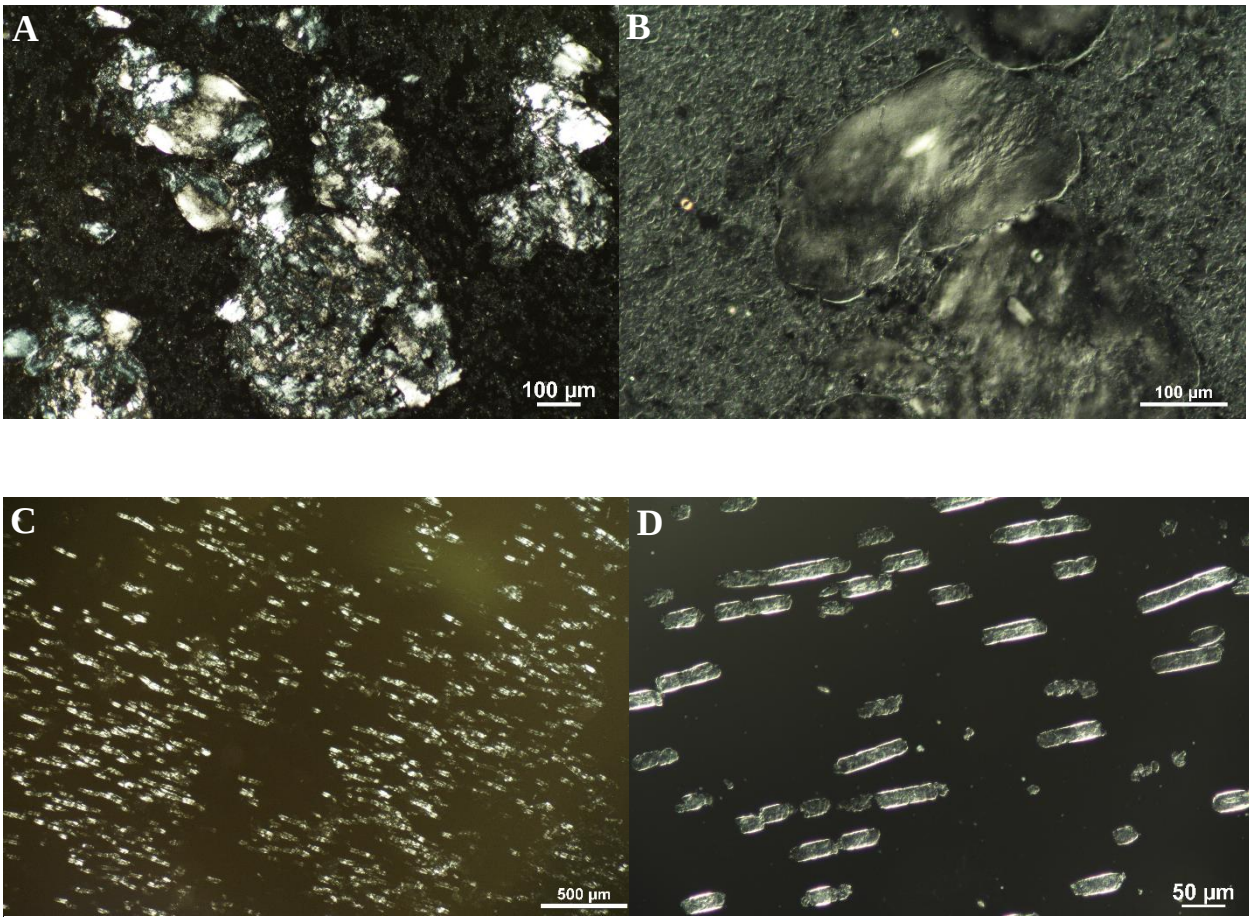

Figure 14 Cross polarized optical microscopy images at magnifications, A. 10x, and B. 20x, for CNC-APTES-E; C. 4x, and D. 20x, for CNC-APTES-E2

The Figures 15A-D show SEM images of the CNC-APTES-E2 dispersion taken at various magnifications starting from 5000x up to 75000x. It is evident that the particle sizes are less than a micron (1 µm), and these particles aggregated to form clusters resembling a cylinder or rod-like morphology. Similar cylindrical structures were also seen under the cross-polarized optical microscopy (from the optical microscopy). The CNC and APTES cross-polymerized to form a dense network.

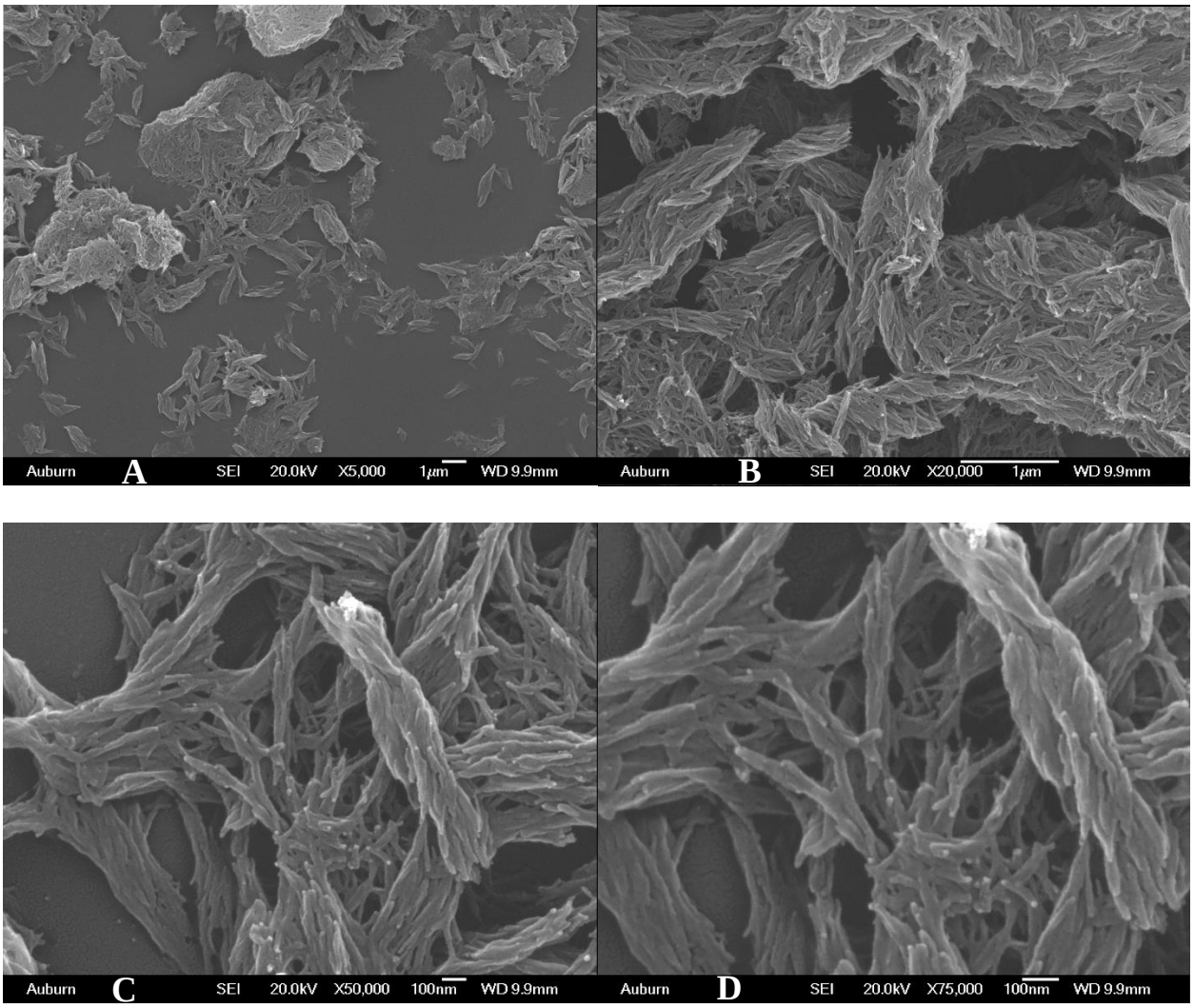

Figure 15 SEM images of CNC-APTES-E2 at magnifications, A. 5000x, B. 20000x, C. 50000x, and D. 75000x.

The water contact angles were measured on the films formed from CNC-APTES-E2 dispersions. To enable this, the CNC-APTES-E2 dispersion was sheared on top of clean and dry silicon (Si 100, 4″ diameter) wafer using a doctor blade coater. It was allowed to air-dry overnight before measuring the coating's contact angle. The results were tabulated in Table 2. A total of 5 runs were performed on the sample on the Si substrate at 5 different locations on the surface. The first 3 readings were taken instantaneously as soon as the water was dropped and the next readings were taken after 10, 20 and 30 seconds. Each value on the table is a mean of the contact angles on

the right and left sides to the water droplet. As observed, the contact angle started at quite high angles owing to the hydrophobicity of the sample. The contact angles gradually dropped down after a few seconds and became quite stable after 30 seconds. So, this value after 30 seconds could be taken as the water contact angle for the sample which is around 47 °. The water contact angles in this range (~50 °) were considered as satisfactory[15] for this kind of application (biosensors) as it is not completely hydrophobic (> 90 °). Truly hydrophobic materials can interfere with the wettability and reduce the interactions with the antibodies, antigens or other reagents present in biological media.

Table 2 Water contact angle measurements for CNC-APTES-E2

Time lapsed	**Mean 1**	**Mean 2**	**Mean 3**	**Mean 4**	**Mean 5**	**Average**
Initial angles	76.4	74.6	69.7	67.5	72.4	72.12
	75.2	73.3	69.8	67	71	71.26
	75.2	71.5	68.3	66.3	68.4	69.94
10 sec	53.8	51.4	49.8	54.2	56.2	53.08
20 sec	53.2	48.3	47.5	47.7	48.6	49.06
30 sec	51.9	46	45.5	45	47.2	47.12

To confirm the successful functionalization with APTES in case of CNC-APTES-E and compare with CNC-APTES-W, an FTIR overlay was produced (Figure 16). CNC-APTES-E confirmed the presence of amino peak from the wide stretch in the range of 3400 cm^{-1}. The O-H stretch occurs over this same range and so they overlap. Also, the sharp high-intensity peaks in the range of 1000-1100 cm^{-1} were attributed to the Si-O-Si and Si-O-C bond vibrations. CNC-APTES-E was able to impart the desired amino functionalization to the CNC as against CNC-APTES-W. But there was a scope for improvement in terms of the aggregation state or achieving a reasonable quality dispersion. Additionally, the process for producing CNC-APTES-E was complicated.

Hence, there was a compelling need to look for alternative processes that were relatively simple, and efficient. This pursuit has led to the development of APTES functionalized CNC adapting the procedure of Kargarzadeh *et al.* (2015)[19] with slight modifications to better suit the needs of this research which will be discussed in the following sections.

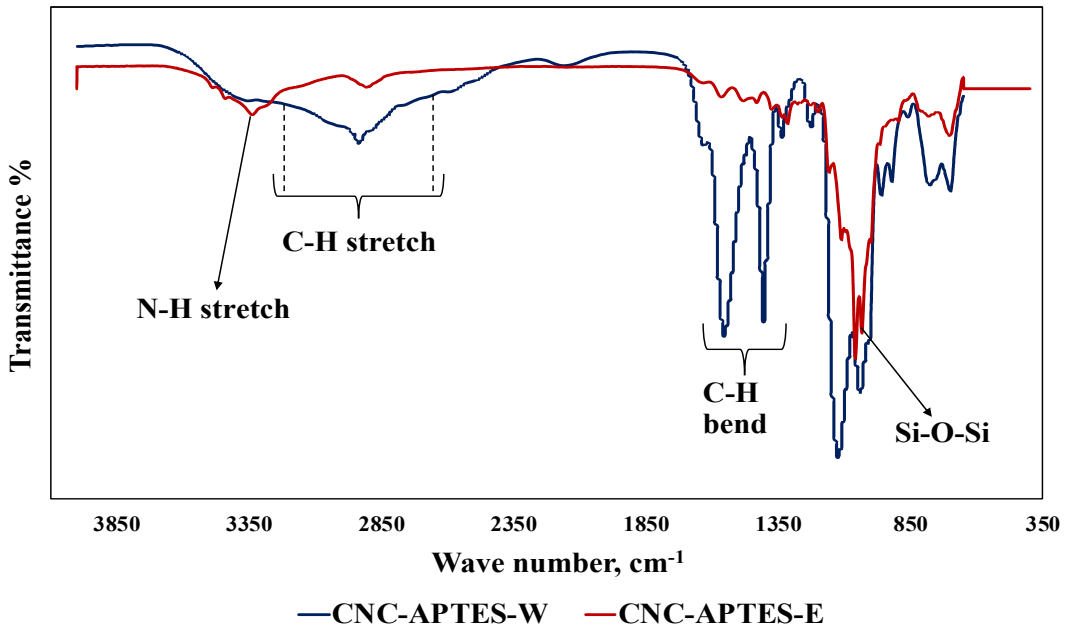

Figure 16 Comparison of FTIR spectra for CNC-APTES-W and CNC-APTES-E

4.3. APTES modification on CNC – Methodology-3

This was generally the same procedure followed for CNC-APTES-E2. However, CNC spray-dried powder was used instead of CNC suspension. The resulting sample was labeled as CNC-APTES-P. This approach was followed mainly to decipher the changes in morphology and any improvement in terms of aggregation state/dispersion quality.

4.3.1. Optical Microscopy and birefringence studies on CNC-APTES-P

The sample CNC-APTES-P showed interesting morphology as observed below from the optical microscopy images (Figures 17A and 17B). The size of the aggregates was almost in the same range as CNC-APTES-E2 i.e. 25-50 µm. The particle diameters were around ~10 µm or less (1-5 µm). The cluster or aggregates of particles assumed a circular shape geometry as against cylindrical geometry in the previous case.

There were various colored regions inside these structures and so it appeared to possess the birefringence property. The presence of birefringence was tested under cross-polarized optical microscopy by rotating the stage at different angles at a magnification of 40x and the images were presented in Figures 18 A-I. The focus was held on the circular aggregate clump which was marked with a dotted line in Figure 18A. However, it was difficult to tell from the images if the samples were truly birefringent. Since this was not the main objective of this study, no further experimental trials were pursued in order to understand the optical properties of CNC-APTES-P.

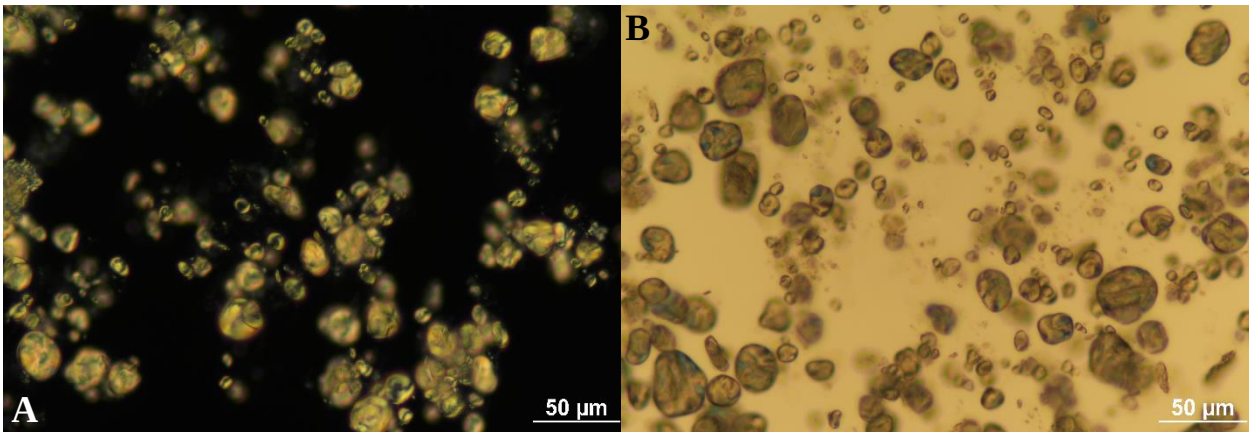

Figure 17 A. Cross polarized optical microscopy image, and B. Non-cross polarized OM image; of CNC-APTES-P at 40x magnification

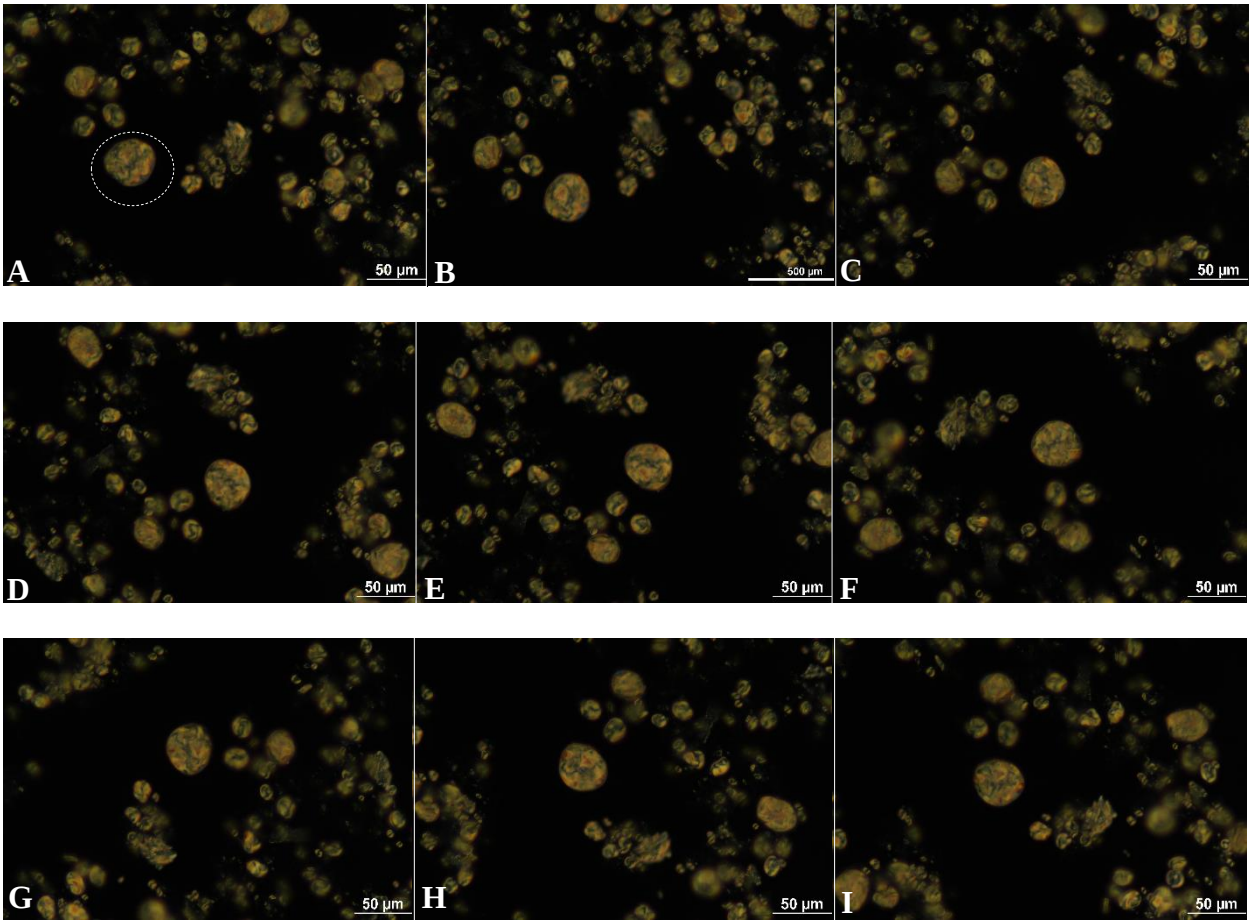

Figure 18 Cross polarized optical microscopy images of CNC-APTES-P at 40x magnification with the stage at – A. 0 degrees, B. 30 degrees, C. 60 degrees, D. 90 degrees, E. 120 degrees, F. 160 degrees, G. 240 degrees, H. 300 degrees, and I. 330 degrees; to the analyzer.

4.4. Dispersion modification trial on CNC until antibody (CEA) immobilization

This method was modified from the synthesis procedure followed by Kargarzadeh *et al.* (2015).[19] An aqueous solution was prepared by adding 0.5 % APTES to a mixture of ethanol-water, 80/20 (v/v %), under stirring, followed by acidification to pH 3-4.5 with glacial acetic acid to improve the extent of amine functionalization on the CNC surface. To this solution 1.5 % spray-dried CNC was added and the dispersion was ultrasonicated for four minutes (amplitude ~ 30%) to prevent the aggregation of the CNC and produce a homogenous suspension. The mixture was kept for 2-3 hours at room temperature. The resulting reaction mixture was washed with distilled

water via vacuum filtration twice making sure the slurry did not dry but had a paste-like consistency. The filtered paste left on the filter paper was transferred into a beaker and PBS was added immediately. The quantity of PBS used was just enough to submerge the sample and it was allowed to settle overnight. This resulting product after APTES modification, in this case, was labeled as CNC-APTES-R.

The GA modification was performed on the CNC-APTES-R in PBS solution. For this reaction, 2.5 % of GA was dispersed in 10 ml PBS and this solution was added to the CNC-APTES-R (which is already in the little amount of PBS). The mixture was ultra-sonicated for 2 minutes (Amplitude ~ 20%, pulse time - 5 seconds) and the reaction was allowed to take place for an hour under gentle magnetic stirring. The resulting product was washed with PBS via centrifugation twice (Conditions: Time - 30 minutes, 1800g) and the bottoms were immersed in just enough PBS to submerge the sample. The resulting product was labeled as 'CNC-GA-R'.

For the antibody immobilization, 4 µl of the AntibodyCEA was dispersed in 5 ml of PBS. This solution was added to CNC-GA-R and the reaction was allowed to take place for an hour at room temperature under gentle magnetic stirring. The product was washed with PBS via centrifugation twice (Conditions: Time - 15 minutes, 1800g) and the bottoms were immersed in just enough PBS to submerge the sample. The resulting product was labeled as 'CNC-aCEA-R'.

4.4.1. Optical Microscopy on CNC-APTES-R, CNC-GA-R, and CNC-aCEA-R

The concentration of the dispersion CNC-APTES-R used for imaging was around 6 wt. %. Figures 19A, 19B and 19C represent the optical microscopy images for CNC-APTES-R taken at magnifications 4x, 10x and 20x respectively. Figure 19B was a non-CP image while the other two were CP images. The aggregates were <50 µm in size and showed interesting colors especially

towards the outer rings. Figures 19D and 19E correspond to the non-CP optical microscopy images of 4 wt. % CNC-GA-R and CNC-aCEA-R respectively. The magnification was maintained at 20x in both of these images. The CNC-GA-R and CNC-aCEA-R had aggregates with maximum sizes up to 25 µm. It was observed from several reaction repetitions that the aggregation state did not worsen after the GA and antibody reactions from the size of aggregates when sonicated for shorter time periods (1-2 minutes) under dilute conditions.

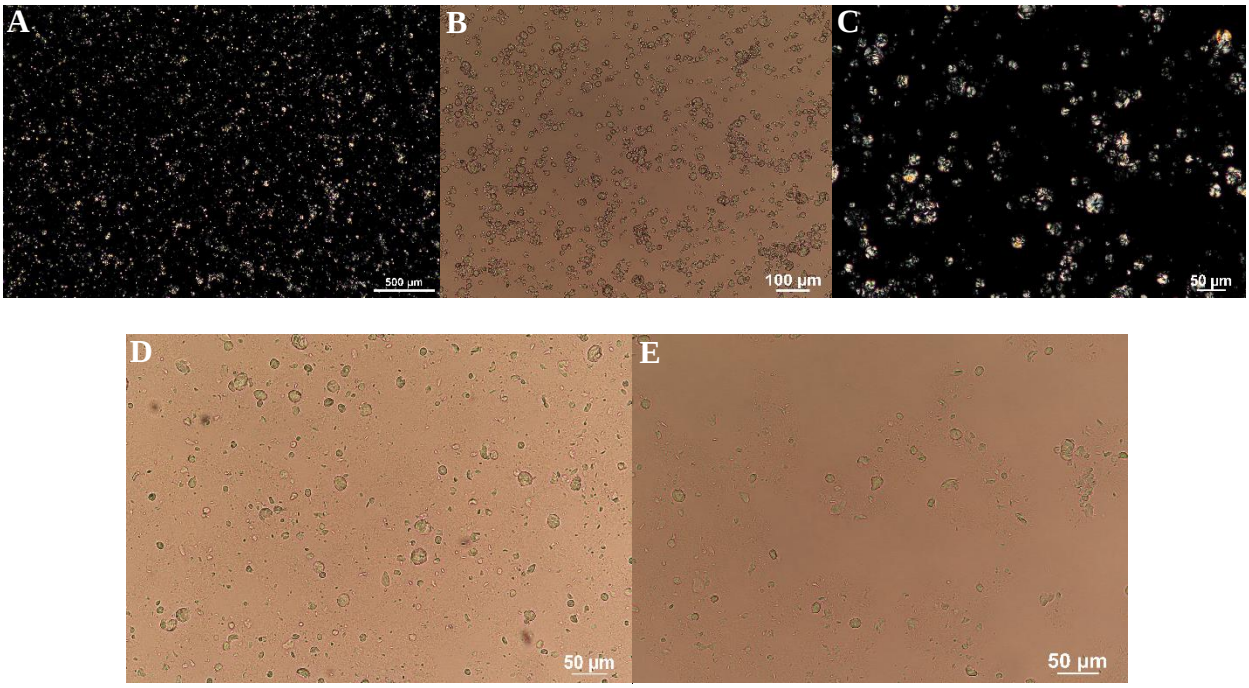

Figure 19 A. Cross polarized optical microscopy image at 4x magnification of CNC-APTES-R, B. Non-CP image at 10x magnification of CNC-APTES-R, C. CP image at 20x magnification of CNC-APTES-R, D. Non-CP image of CNC-GA-R at 20x magnification, and E. Non-CP image of CNC-aCEA-R at 20x magnification

The antibodies have fluorescent probes directly conjugated to them which enabled to confirm the successful antibody immobilization reaction using fluorescence microscopy imaging. The fluorophore that is attached to the antibody CEA is the Alexa Fluor 555 dye which has an excitation maximum of 555 nm and an emission maximum of 580 nm (orange light). The common

filter set used when imaging a sample labeled with this dye is TRITC (Tetramethylrhodamine). The samples were imaged in dispersion form. Figures 20A and 20B show the fluorescence microscopy images of the CNC-GA-R (reference/non-labeled) and CNC-aCEA-R (labeled) respectively. The sample CNC-GA-R did not emit any light back to the detector or show a positive signal with significant intensity as observed from the blank image. On the other hand, the CNC-aCEA-R showed a large increase in the fluorescence intensity. As seen from the respective images for CNC-aCEA-R, the sample is emitting light in orange red which corresponds to the presence of Alexa Fluor 555. Therefore, the antibodies were successfully immobilized onto the CNC-GA-R.

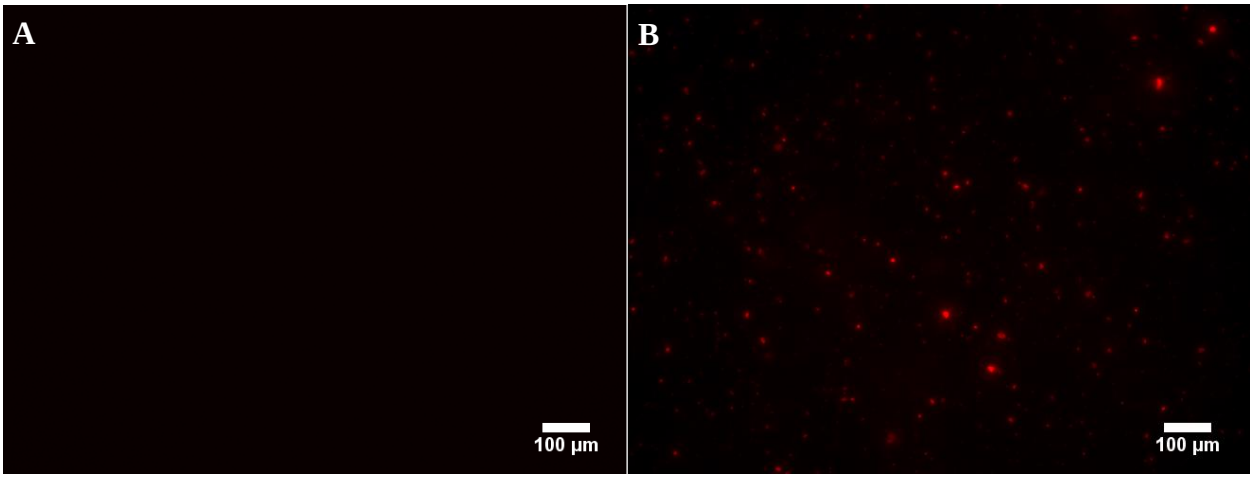

Figure 20 Fluorescence microscopy images for A. CNC-GA-R, and B. CNC-aCEA-R; taken with TRITC filter at 10x magnification

The background intensity in case of non-labeled should always match the background or minimum intensity in case of labeled sample. From Table 3, the minimum intensities for both the samples of observation are within the same range, denoting the same reference intensity but the maximum intensities varied as a result of the antibody immobilization reaction. The maximum intensity of CNC-aCEA-R increased at least by 25-fold as compared to the non-labeled one, but the mean intensity increase was only 3-fold. This could imply that the maximum intensity was as

a result of a few brightest spots in the sample while most of them were less bright. However, the light emission intensity by the fluorophores depends on several factors such as their lifetime, orientation, steric hindrance, viscosity etc.

Table 3 Fluorescence intensities of CNC-GA-R and CNC-aCEA-R

Sample name	Mean Intensity	Fluorescence Intensity	
		Min	Max
CNC-aCEA-R	1923	511	16383
CNC-GA-R	567	481	621

4.5. Surface modification and biomarker immobilization on CNC - A final/optimized procedure

In this method, an aqueous solution was prepared by adding APTES (0.5%) to a mixture of 50 ml of water-ethanol, 80/20 (v/v %). Under stirring, the solution was acidified to a pH 4 using glacial acetic acid. This step was performed to improve the functionalization of the resulting surface-modified CNC.[19, 121] 4g of 11.3% CNC suspension in water (batch# 2018-FPL-CNC-126) was added to the APTES solution and ultrasonicated for 4 minutes (amplitude ~ 30%) to prevent the aggregation of the CNC. The mixture was kept for 2 hr (overnight could be preferred to achieve higher yields while washing) at room temperature under magnetic stirring. The resulting product was washed twice with ultrapure water via centrifugation (Beckman Coulter Allegra X-12R with an SX4750A rotor, 2200g, and 50-minute cycles). The bottom product was collected and labeled as CNC-APTES. For the second surface modification, 2.5% GA was dispersed in 10 ml of water and added to CNC-APTES. This reaction was allowed to take place for 1 hour (overnight could be preferred to achieve higher yields while washing) under gentle magnetic stirring at room temperature. The resulting mixture was washed twice with ultrapure water (40-minute cycles at

1800g). The bottoms were collected and labeled as CNC-GA. Then, 4 µl of each of the antibodies was diluted 5 ml of PBS and reacted with CNC-GA for an hour at room temperature under gentle magnetic stirring. This reaction was conducted in a dark environment to enable fluorescence analysis. Post reaction, the mixture was washed twice with PBS (30-minute cycles, 1700g). The resulting sample was wrapped in aluminum foil ensuring minimal light exposure while using it further. The samples were labeled as CNC-antiCEA, CNC-antiAFP and CNC-antiPSA. The antigen immobilization reactions were performed on the aforementioned samples using the respective antigens CEA, AFP, and PSA in PBS under the exact same conditions as the antecedent process. The resulting samples after washing steps were labeled as CNC-CEA, CNC-AFP and CNC-PSA.

In this optimized procedure, a change back to the CNC suspension from the spray-dried powder used in the dispersion modification trial on the CNC method (Section 4.4) was made. This is because the fine powder has spherical shaped or donut-shaped particles with CNC already aggregated to each other.[122] Whereas, the individual CNC are rod-like with high-aspect ratios,[112] which will give access to their nanoscale surface and exceptional properties. The surface modification and immobilization reactions of the CNC in dispersion state were presented in the scheme below (Figure 21). A similar scheme was used on solid aligned CNC films, with the shear aligned CNC film as the starting material. The film modification process was the simplest while the dispersion modification involved complex reaction conditions to account for the challenges posed in dispersion state.

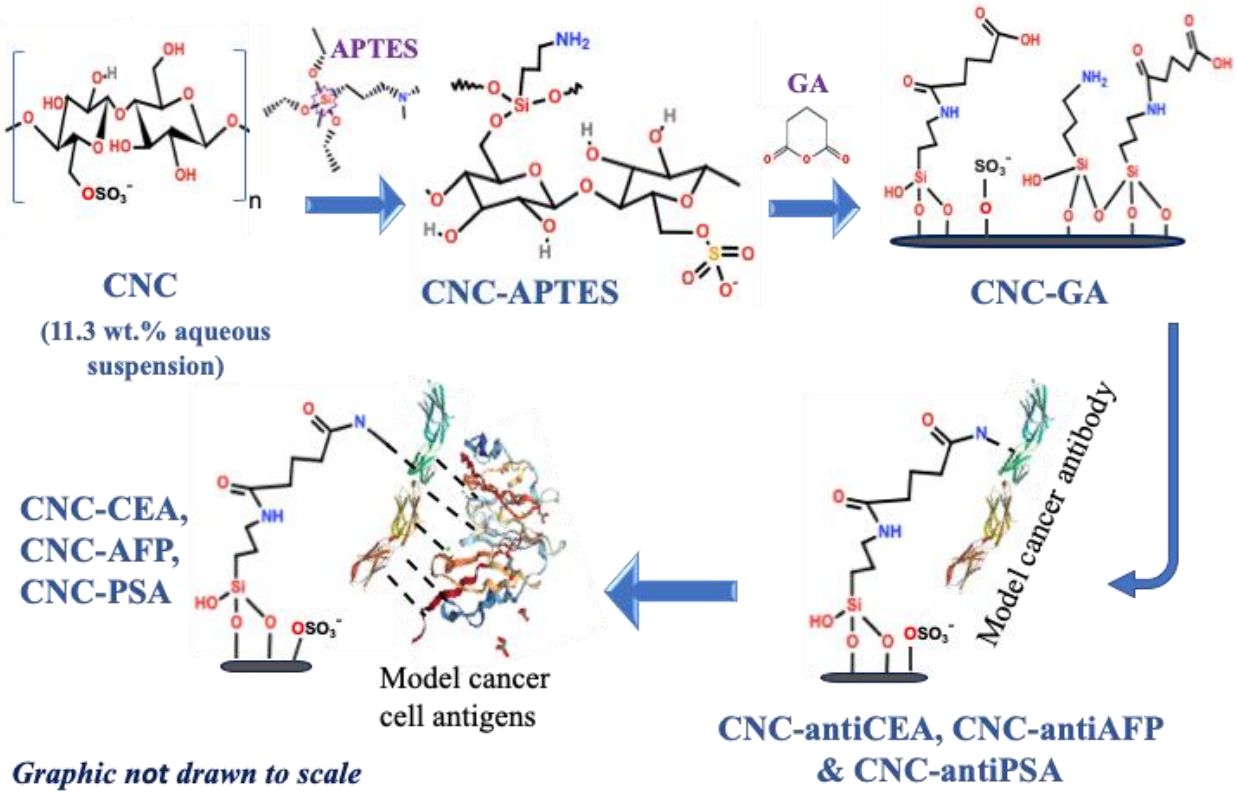

Figure 21 Antibody-antigen immobilization reaction mechanism on CNC

4.5.1. ATR-IR spectroscopy analysis

The reaction chemistry at each step until antibody immobilization was validated preliminarily using ATR-IR spectroscopy for one antibody namely antiCEA (since all the antibodies/antigens have similar functionalities). ATR-IR was performed to confirm each step of the reaction scheme (Figure 22). The initial CNC shows the absorbance peaks in the range 3400-3300 cm^{-1}. These are attributed to the stretching of the OH groups of cellulose. The peaks observed at 1426 and 1315 cm^{-1} in the spectra of both CNC and CNC-APTES were attributed to the symmetric bending of CH_2 and the bending vibrations of the CH and CO groups of the rings in polysaccharides, respectively. The absorbance peaks in the range 1030-1161 cm^{-1} attributed to C-O stretching and C-H rocking vibrations of the pyranose ring skeleton.

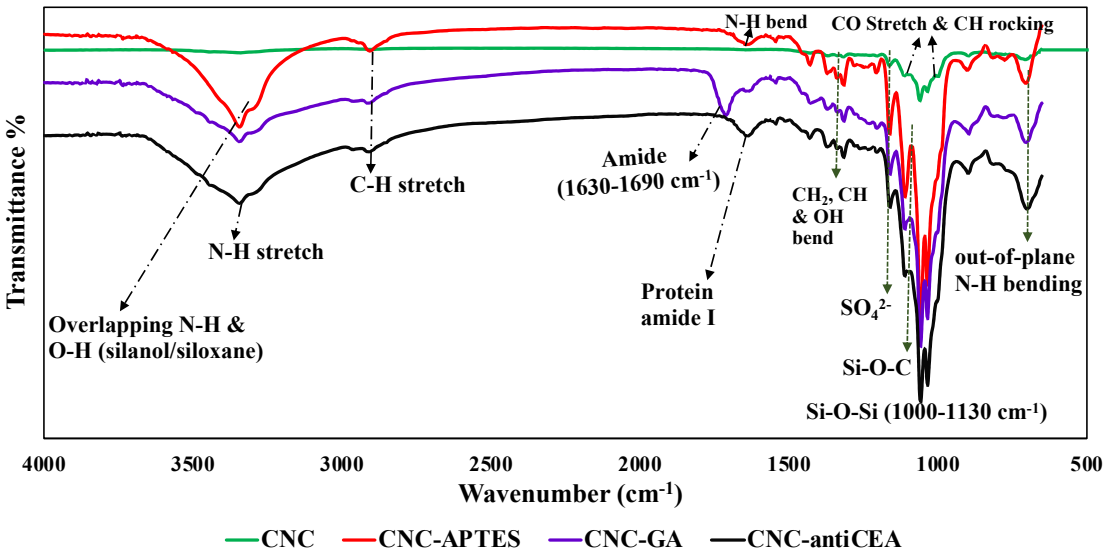

Figure 22 FTIR spectral overlay for CNC, CNC-APTES, CNC-GA and CNC-antiCEA

For the CNC-APTES, the peaks at 1640 and 1459 cm^{-1} correspond to NH_2 groups. The strong absorption of the two bands in the region 1000-1200 cm^{-1} assigned to Si-O-Si and Si-O-C bonds. The peak at 780 cm^{-1} is due to out-of-plane bending absorption of the amino group. The peaks in the range 3200-3400 cm^{-1} were assigned to OH free hydroxyl groups, from the silanol groups, and also to the N-H bending vibrations due to the primary amines on the surface (overlapping region of N-H and O-H bond stretches). For the CNC-GA, the absorbance peak in the range of 1630-1690 cm^{-1} corresponds to the amide (C=O stretch) functional group. The peaks in the range of 3200-3400 cm^{-1} are flattened as compared to the sharper peaks observed in the case of CNC-APTES. This could be due to the increase in the hydroxyl groups (from COOH) of the GA, and the overall decrease in primary NH_2 groups as a result of GA reaction.

After the antiCEA immobilization, the absorption at around 1600-1700 cm^{-1} was observed which corresponds to the protein amide (Amide I) band. The Amide I band is due to C-N stretching vibrations in combination with C=O bending. The corresponding N-H stretch in the range of 3200-

3400 cm^{-1} is seen becoming sharper as compared to the previous step. This confirms the successful immobilization of the antibody.

A comparison of the functionalization between the dispersion modified CNC-APTES and the film modified CNC-APTES was also performed using ATR-IR (Figure 23). It can be inferred that the dispersion modified CNC have sharper, high-intensity peaks at the wavelengths corresponding NH_2, Si-O-Si and Si-O-C bonds, indicating superior surface modification as against the film modified counterparts.

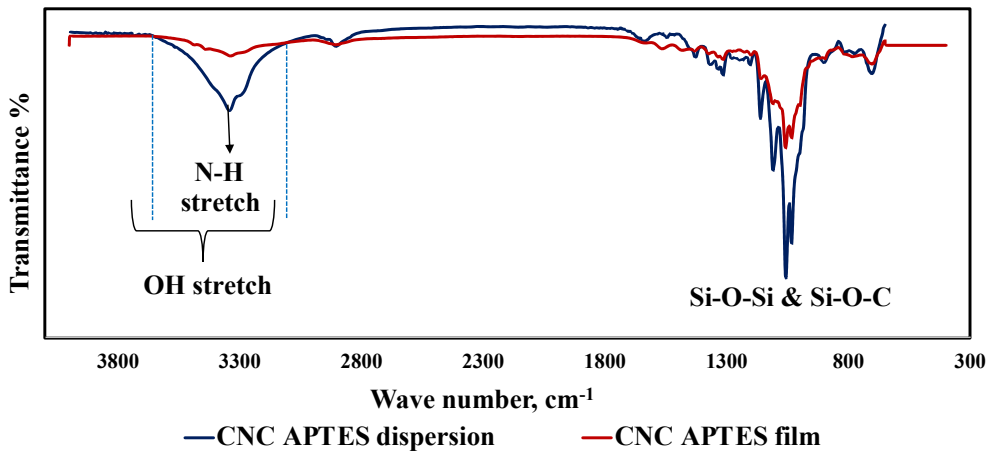

Figure 23 FTIR spectral overlay of dispersion and film modified CNC-APTES

4.5.2. Thermal degradation studies

The TGA coupled FTIR analysis or TGA was performed on various dispersions. Tests on CNC, CNC-APTES and CNC-GA and also the GA were conducted in both air and argon (Ar). Characterization of CNC-antiAG and CNC-AG, the TGA-FTIR analysis was performed in air. The amounts of antibody and antigen attached were very low compared to the bulk CNC-GA; therefore, it was challenging to accurately quantify the residual weight contributions of the functional groups due to antibody immobilization and antigen binding. When analyzing the TGA

data, the weight loss at the end of 120 °C hold was considered as 100 % mass and the rest of the data until 700 °C was recalculated. The TGA data was plotted with temperature on X-axis and the weight % on the Y-axis. The FTIR Gram-Schmidt data was plotted with the FTIR time in minutes and the intensity on the axes. This FTIR times can be correlated to the TGA times and temperatures which further gives information about the weight percentages and the gaseous evolution.

The TGA analysis was performed on the ~11.3 wt.% CNC aqueous suspension (batch # 2018-FPL-CNC-126) in both air and Ar atmosphere. The runs on the CNC in air were repeated for at least four times to check errors. The TGA may sometimes produce unreliable data if the loaded solid mass was very low (say less than 2 mg). In all of the repetitions, the results were very similar and the results from two of the runs were discussed here. In the final run (Figure 24), the initial weight of CNC that was loaded into the sample pan was 120 mg. The weight loss for the temperatures <120 °C was attributed to loss of free water. After the hold the remaining mass was 13 mg of CNC. This was used as 100 wt. % and applied to all the weights until 700 °C. The CNC as showed good thermal stability, the material maintained at least 95 % mass at 240 °C; 95% mass retention was used to define the thermal degradation temperature, T_d. Wang *et al.* (2007)[123] and few others studied correlation between TGA residual masses, T_d etc. to the amount of sulfate groups present on the surface of CNC. According to their studies, higher T_d values (~240 °C) and low residual masses indicate the presence of very low amounts of sulfate groups on the CNC surfaces.[13, 123, 124] Therefore, the presence of low amount of sulfates was justified from the low residual weights of CNC that were obtained in this study (~2 wt.%).[123] The mass at 500 °C was 0.6 mg where the oxidation of the char residue was supposed to begin. Finally, the mass at the end of isothermal hold at 700 °C was 0.24 mg; in all cases the residual mass was approximately 2 wt.%.

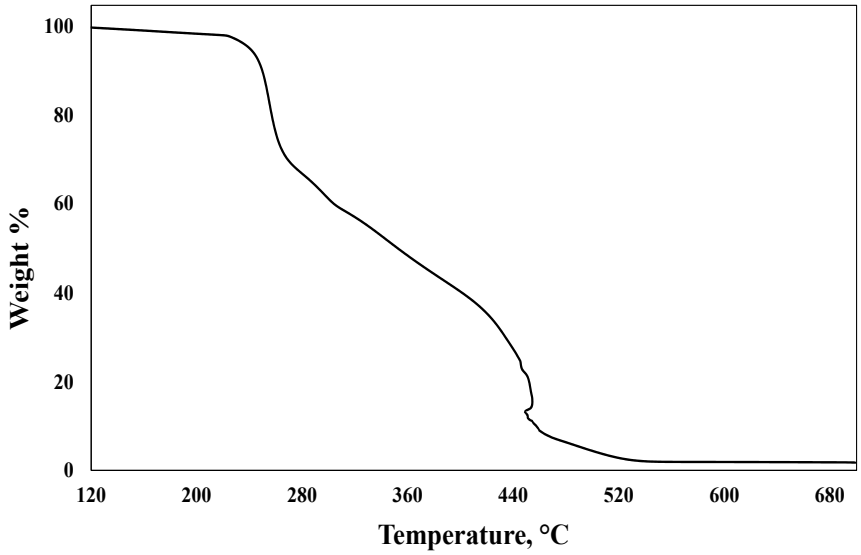

Figure 24 TGA plot of CNC conducted using air as sample gas

Figure 25 corresponds to the TGA-FTIR run on the CNC in air. This was performed to obtain more information on the decomposition products of CNC at various temperatures. For this sample, vacuum drying (30 min at 80 °C) was performed prior to the TGA-FTIR to increase the solid mass content. The FTIR started collecting data 50 minutes after the start of TGA data collection; this corresponded to the end of the 120 ºC isothermal hold. Therefore, 50 min. was added to the FTIR linked spectrum times to locate the corresponding temperature on the TGA.

The weight loss was around 5 % up to 240 °C. The sharp weight loss (~73 wt.%) between 240-450 °C corresponds to simultaneous degradation processes such as depolymerization, and decomposition of glycosyl groups of CNC to form a solid residue. The weight loss above 450 °C-700 °C (~ 20 %) represents the oxidation and breakdown of the charred residue to lower molecular weight gaseous products (accompanied decomposition of residue).

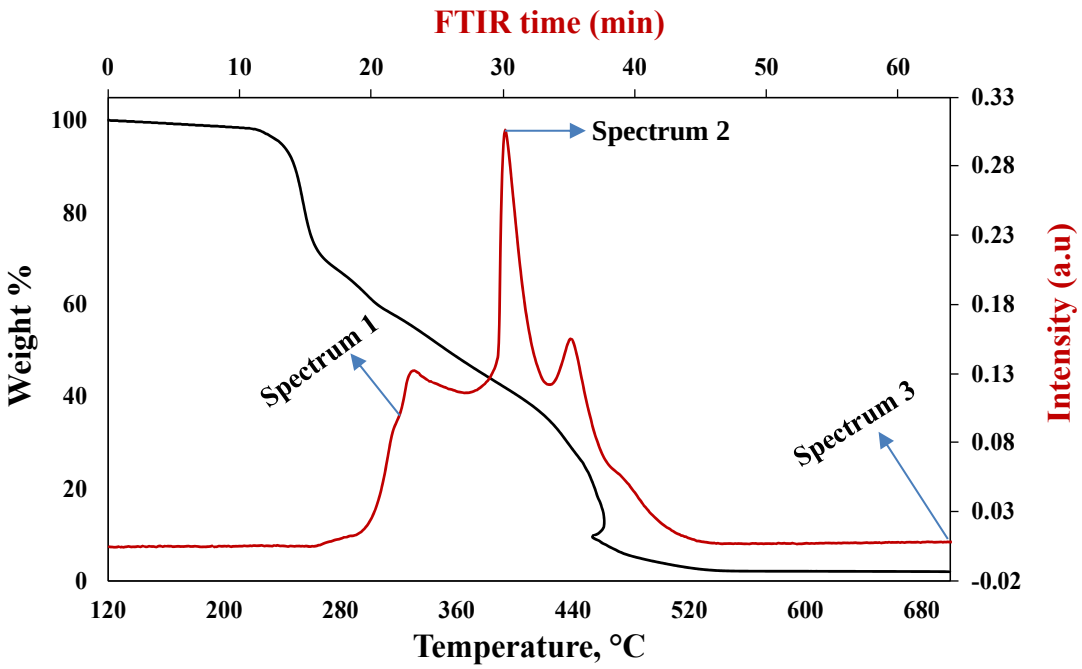

Figure 25 TGA and Gram-Schmidt plots for CNC in air

The FTIR linked spectrum at around 23 min (Figure 26A) which corresponds to 73 minutes from the TGA data showed the evolution of carbon dioxide (CO_2) and water (H_2O) along with some organo-sulfates presumably. The corresponding temperature range from the TGA marked for this evolution was around 335 °C. Since the sample was in gel form and vacuum drying stripped away the majority of the moisture, the acid moisture along with the sulfates were assumed to be evolved.[125] The absorption bands at 1200 cm^{-1} and 1000 cm^{-1} could be attributed to -OSO_3^-; 810 cm^{-1} to acid sulfate, -HSO_4^- [126, 127] and the sharp absorbance peak at around 2350-2400 cm^{-1} could be attributed to CO_2. Figure 26B shows the spectrum at 31 minutes and the corresponding temperature was around 413 °C. The broad bands at around 600-700 and 3550-3700 cm^{-1} could be attributed to CO_2.[127, 128] The sharp high intensity peak close to 2400 cm^{-1} could be attributed to CO_2 and the two small peaks around 2200-2300 cm^{-1} could be attributed to the evolution of carbon

monoxide (CO) gas. Figure 26C shows the spectrum at 85 minutes which was collected at 700 °C during the isothermal hold, the products from the oxidation of the solid residue were observed evolving. The broad bands at 1300-1900 cm^{-1} and 3500-3900 cm^{-1} could be attributed to H_2O. The double peak at 2300 cm^{-1} corresponds to CO.[128]

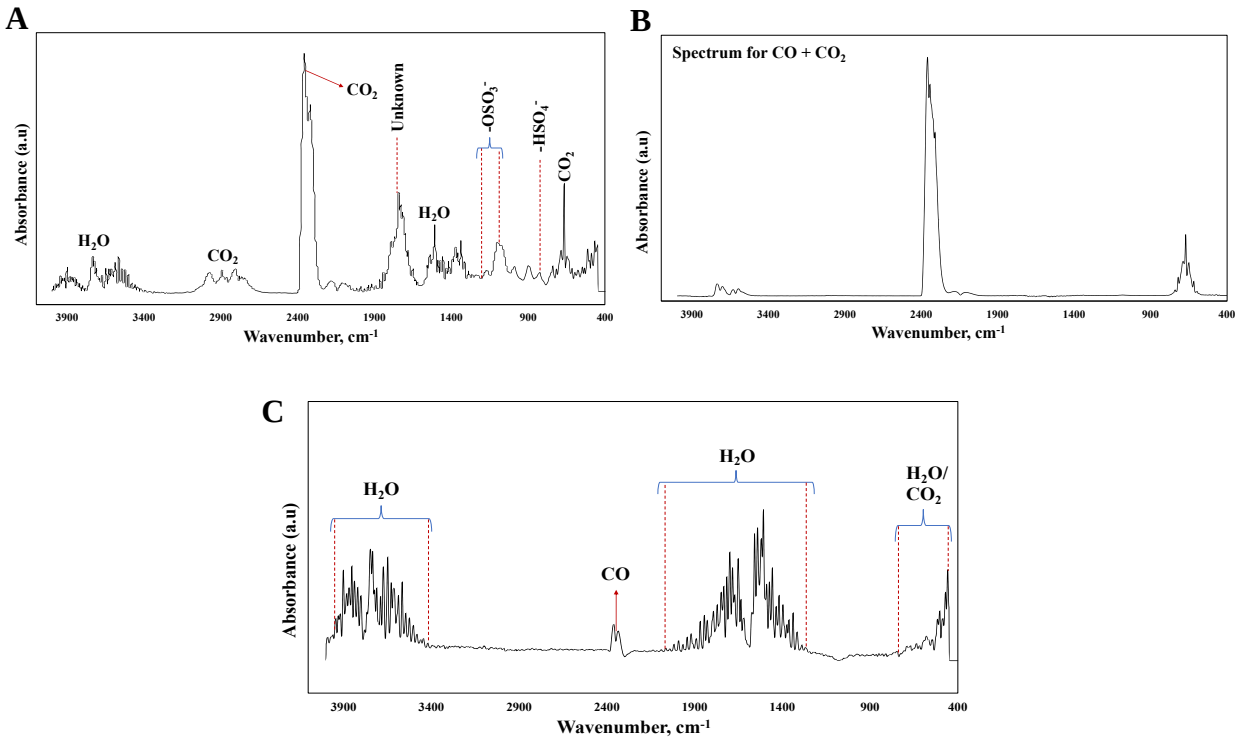

Figure 26 A, B, and C. FTIR linked spectra of CNC corresponding to the evolution of various compounds at 335 °C, 413 °C, and 700 °C respectively.

Figure 27 corresponds to the TGA plot of CNC conducted using Ar as sample gas. The T_d was similar to the value obtained for the CNC in air i.e. 242 °C. However, the residual wt.% in Ar increased significantly to 26 wt. % as compared to the 2 wt. % in air. This could be mainly attributed to the char residue from the formation of carbides in the presence of Ar whereas in air there would be higher gaseous evolution with accompanying mass loss due to the combustion of the char to form oxides. No TGA repetitions were conducted in Ar for CNC and this analysis is based on the data from a single run. The initial mass was 106 mg; after 120 °C hold the mass was

12 mg and the final residual mass at the end of 700 °C hold was 3 mg. The weight loss in the range of 240-450 °C was 55 % which was less than the value obtained in air (~73 %). And, the weight loss beyond this point until the end of 700 °C decreased significantly to approximately 14 % in Ar as compared to the air runs (20 %). This could be because of the elimination of several oxidation reactions due to Ar environment which could occur in the presence of air. From the data, the TGA curves of CNC in Ar were very smooth as compared to CNC in air (Figures 24 and 25). In air, at a temperature of approximately 450 °C, there was at least 5 °C shift backwards that was seen in all of the repetitive runs which was assumed to be happening due to the higher ramping rate i.e. 10 °C/min. This was not observed when the sample gas was shifted to Ar.

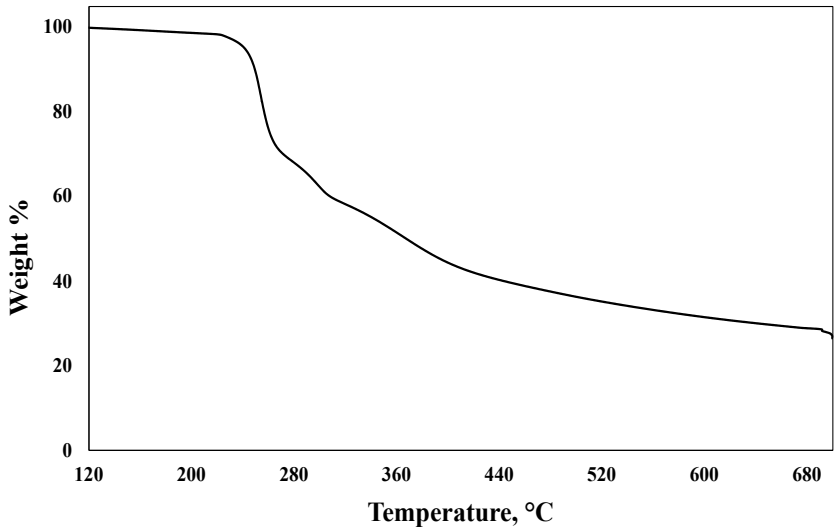

Figure 27 TGA plot for CNC using Ar as sample gas

Figure 28 corresponds to the TGA plot and the FTIR Gram-Schmidt overlay for the dispersion CNC-APTES conducted in air. Two repetitions were conducted on CNC-APTES coming from two different reaction batches using same conditions to confirm the reliability of the data and the results were in agreement with each other. The degradation temperature was around

231 °C where the weight loss was 5 %. From T_d to 450 °C, the weight loss was 58 % and at higher temperatures from 500-700 °C, the weight loss was 34 % leaving behind a residual weight % of 3. The slightest increase in the residual weight could be on account of the added silicon functionality due to APTES functionalization. In terms of actual mass, the initial mass that was loaded for analysis was 98 mg. The mass by the end of 120 °C hold was around 8 mg and the final residual mass was 0.2 mg.

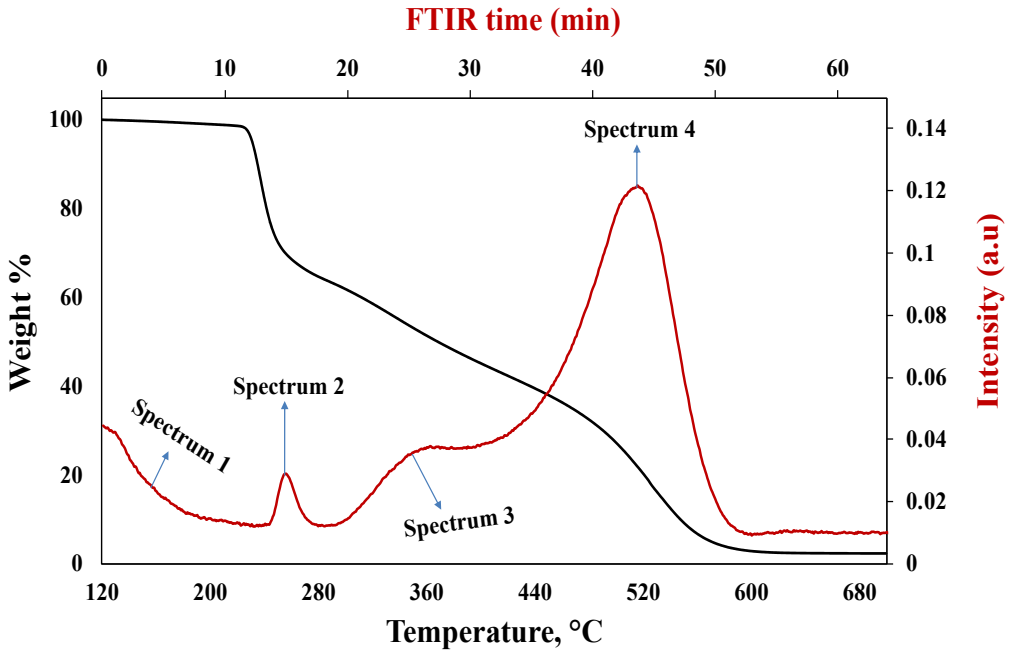

Figure 28 TGA and Gram-Schmidt plots for CNC-APTES in air

Spectrum 1 collected at a temperature of 152 °C (Figure 29A) showed the evolution of CO_2 and H_2O along with some organo-sulfates. The FTIR peak intensities of $-OSO_3^-$ and $-HSO_4^-$ decreased or were less prominent as compared to the CNC. This could be because of the added APTES weights. The linked spectrum at 250 °C (Figure 29B) showed an evolution of CO_2, H_2O along with nitrous oxide (N_2O) and nitric oxide (NO) presumably. The additional evolution of N_2O corresponding to wavenumber around 2400 cm^{-1} and NO around 1100-1200 cm^{-1} were assumed to

be coming from the amino functionality present in APTES. The linked spectrum at 355 °C (Figure 29C) consisted of mainly CO_2, and H_2O while the linked spectrum at 538 °C (Figure 29D) showed an additional evolution of CO.

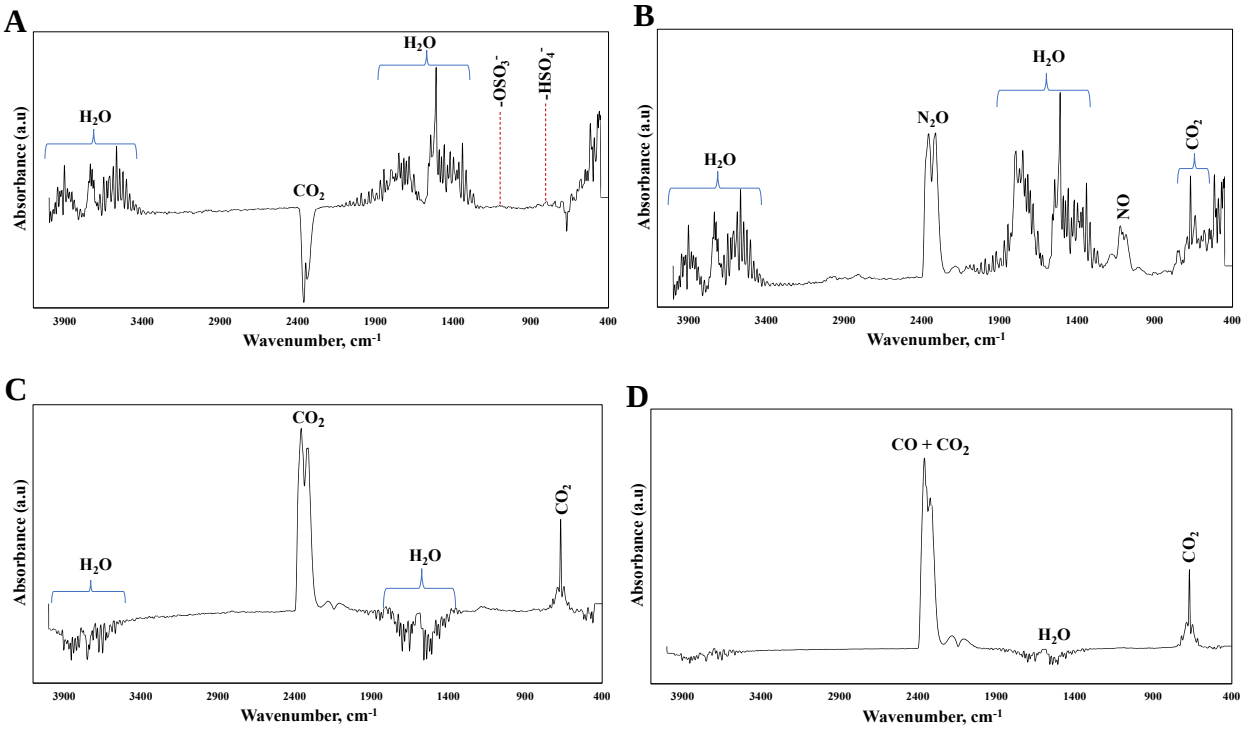

Figure 29 A, B, C and D. FTIR linked spectra of CNC-APTES in air corresponding to the evolution of various compounds at 152 °C, 250 °C, 355 °C and 538 °C respectively.

Figure 30 corresponds to the TGA plot and the FTIR Gram-Schmidt overlay for the dispersion CNC-APTES conducted under Ar atmosphere. The analysis on this sample is based on the data/results from a single run. The initial loading mass was 108 mg. The mass at the end of 120 °C hold was around 9 mg and the final residual mass was therefore 3 mg. From T_d to 450 °C, the weight loss was 52 % and at higher temperatures from 450-700 °C, the weight loss was 11 %. The residual weight % was approximately 32 wt.% which was much higher than the CNC-APTES air run (3 wt.%). This can be mainly attributed to the Ar atmosphere. A residual weight % of 32

was obtained which could be due to the char residue along with silicon-based compounds (siloxanes, Si-O-C etc.) formation as a result of APTES modification of CNC.

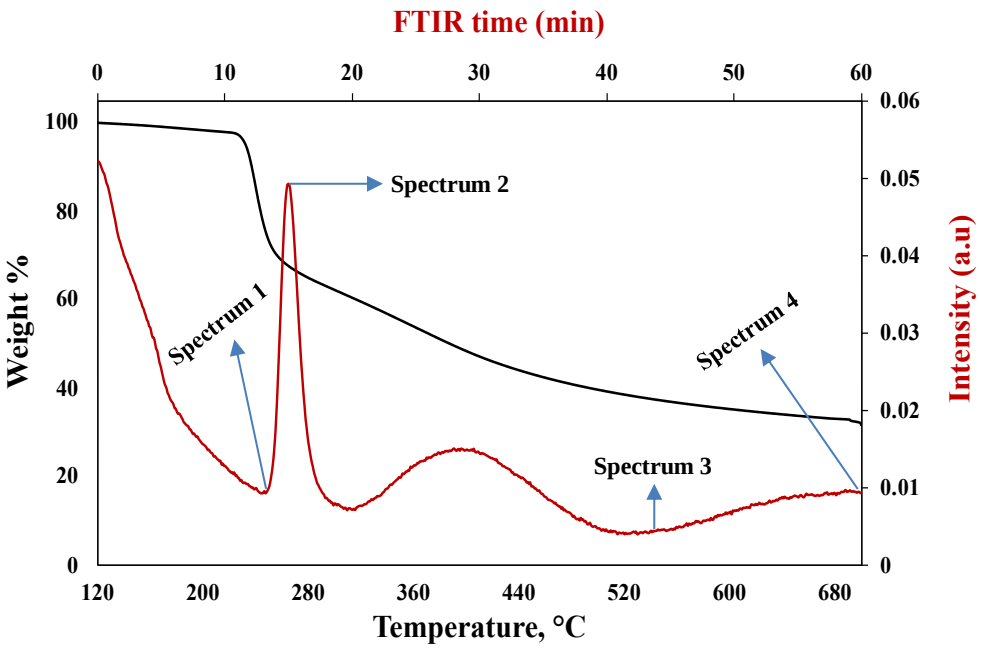

Figure 30 TGA and Gram-Schmidt plots for CNC-APTES in Ar

The linked spectrum at 243 °C in Figure 31A showed evolution of H_2O, CO_2 and organo-sulfates along with some possible ethylene. There was also N_2O evolution assumed to be coming from the amino group after APTES functionalization but with slightly reduced intensity as compared to the CNC-APTES air run. The linked spectrum at 255 °C (Figure 31B) showed evolution of H_2O, CO_2 and NO. At 544 °C, the evolution consisted of H_2O and CO_2. The sharp peak at 3000 cm^{-1} could be attributed to methane (CH_4) and the double peak in the range of 2900-2800 cm^{-1} could be attributed to the ethylene as a result of degradation (Figure 31C). During the isothermal hold at 700 °C, the linked spectrum collected mainly consisted of CO and CO_2 (Figure 31D).

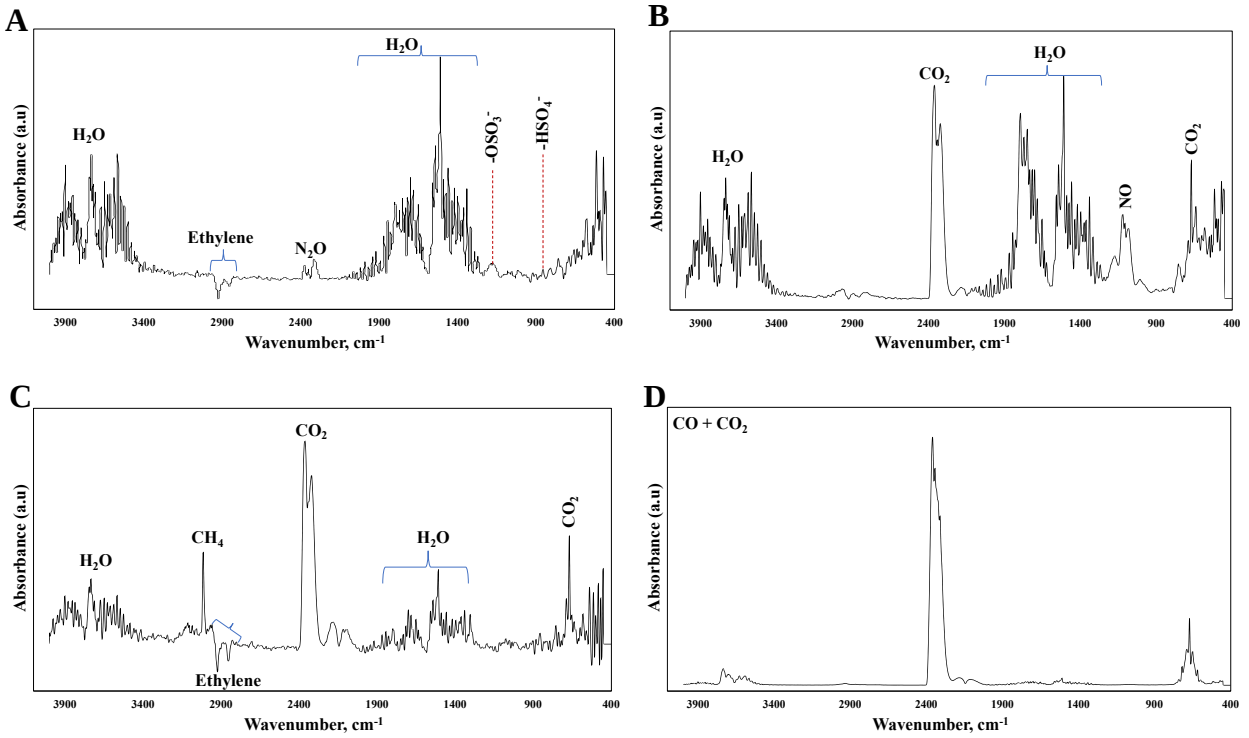

Figure 31 A, B, C and D. FTIR linked spectra of CNC-APTES in Ar corresponding to the evolution of various compounds at 243 °C, 255 °C, 544 °C and 700 °C respectively.

In addition to characterizing the CNC with bound APTES and GA, TGA analysis was also performed on GA (as obtained from vendor) which is a solid at room temperature. Figure 32 corresponds to the TGA plot of the GA conducted using air as sample gas. The T_d value obtained at 5 % weight loss of the sample was 142 °C. This analysis was based on the data from a single run. The initial mass was around 19 mg; after 120 °C hold, the mass was 17 mg and the final residual mass at the end of 700 °C hold was negligible. There was a sharp weight loss starting from 150 °C until around 240 °C. The mass at the end of 240 °C was approximately 0.03 mg. The accompanied weight loss in this range of 150-240 °C was 91 % and the final residual weight % at the end of 700 °C was 0.02 %.

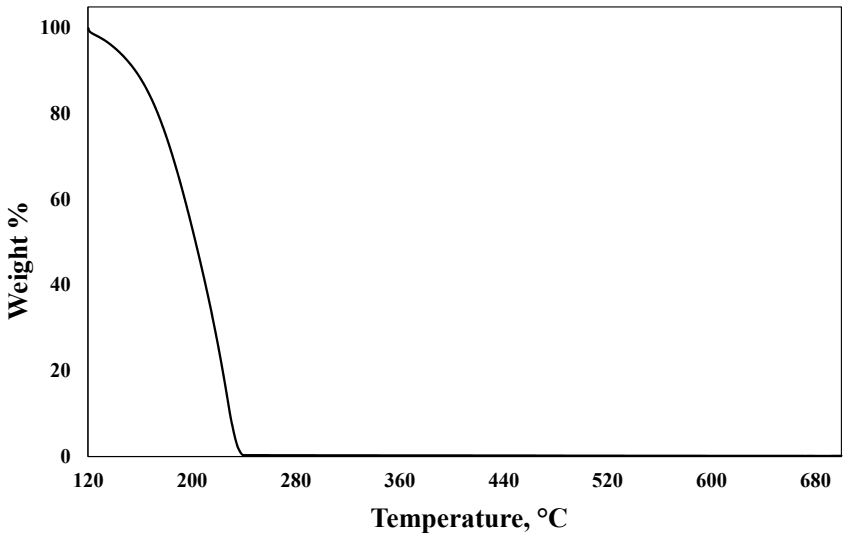

Figure 32 TGA plot of GA using air as sample gas

The TGA analysis was also performed on GA under Ar atmosphere. Figure 33 corresponds to the TGA plot of the GA conducted using Ar as sample gas. The T_d value obtained at 5 % weight loss of the sample was around 139 °C. This analysis was also based on the data from a single run. The initial mass was around 19 mg; after 120 °C hold, the mass was 16 mg and the final residual mass at the end of 700 °C hold was also almost negligible but slightly higher than the air run. There was a sharp weight loss starting from 150 °C until around 240 °C similar to the air run. However, the mass at the end of 240 °C decreased slightly to 0.02 mg. The accompanied weight loss in this range of 150-240 °C was also 91 % but the final residual weight % at the end of 700 °C increased to 0.06 %.

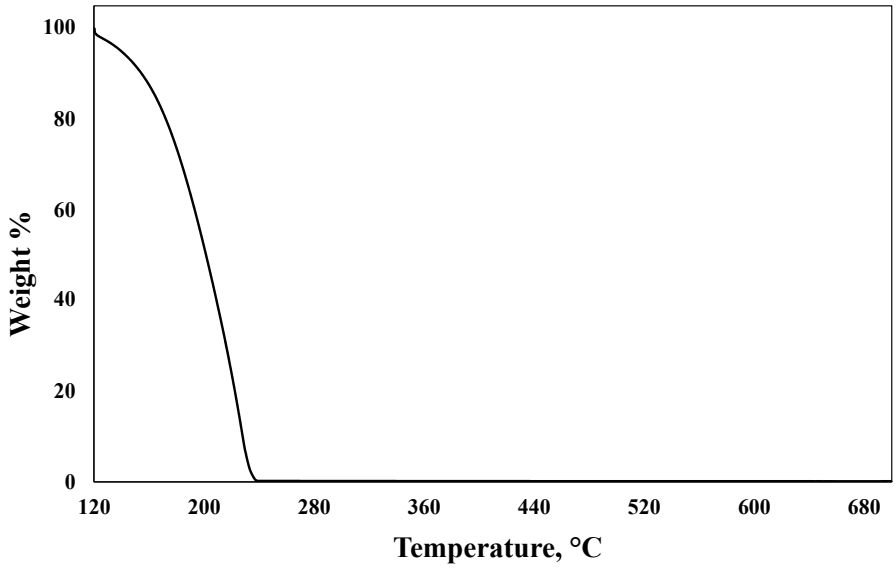

Figure 33 TGA plot of GA using Ar as sample gas

Figure 34 corresponds to the TGA plot and the FTIR Gram-Schmidt overlay for the dispersion CNC-GA conducted in air. The analysis on this sample is based on the data/results from a single run. The degradation temperature was around 220 °C where the weight loss was 5 %. From T_d to 450 °C, the weight loss was 55 % and at higher temperatures from 500-700 °C, the weight loss was 28 % leaving behind a residual weight of 12 wt. %. This increase in the residual weight in comparison to CNC-APTES in air (3 %) could be on account of introduction of amide functionality into the structure from the GA modification as they do not oxidize easily.[129] The degradation of the amides commences at high temperatures, around 400 °C where their dehydration starts leaving behind C-N groups. The C-N along with the Si and char residue could be the dominant reason for the increased residual mass. In terms of actual mass, the initial mass that was loaded into the TGA sample pan for analysis was 140 mg. The mass by the end of 120 °C hold was around 14 mg and therefore the final residual mass was 2 mg. The linked spectrum at around 312 °C in Figure 35A showed evolution of H_2O and CO_2. The linked spectrum at 463 °C

(Figure 35B) showed evolution of CO_2 and CO. At 525 °C, the evolution mainly consisted of CO_2 (Figure 35C). At 700 °C, the linked spectrum collected mainly consisted of H_2O and CO_2 (Figure 35D).

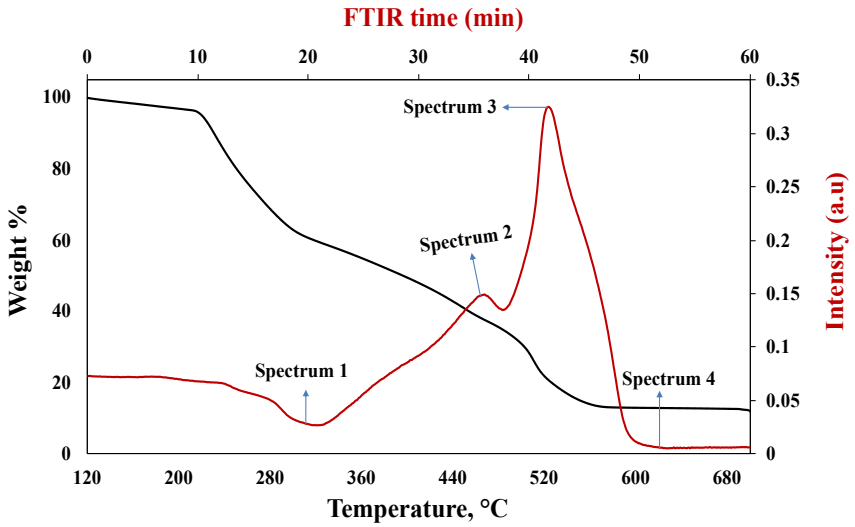

Figure 34 TGA and Gram-Schmidt plots for CNC-GA in air

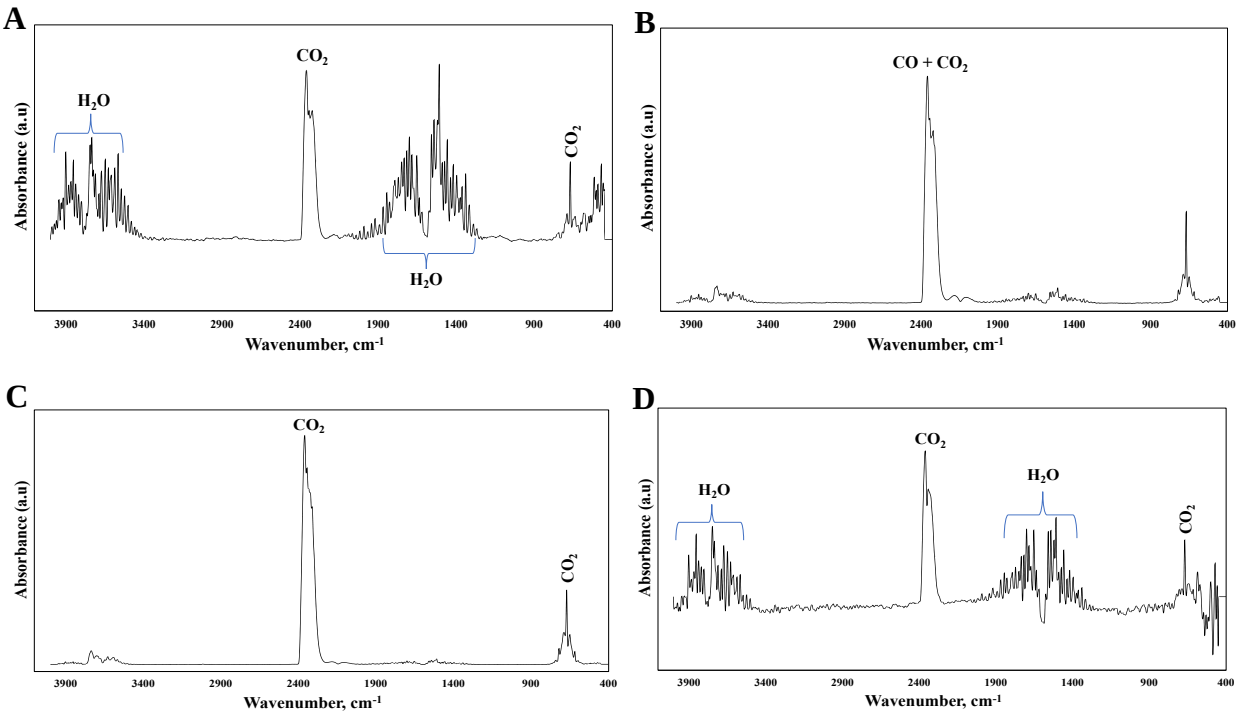

Figure 35 A, B, C and D. FTIR linked spectra of CNC-GA in air corresponding to the evolution of various compounds at 312 °C, 463 °C, 525 °C and 624 °C respectively.

Figure 36 corresponds to the TGA plot and the FTIR Gram-Schmidt overlay for the dispersion CNC-GA conducted under Ar atmosphere. The analysis on this sample is based on the data/results from a single run. The residual mass was approximately 29 wt.% which was slightly lower as compared to the CNC-APTES Ar run (32 wt.%). This result is opposite of the one that was obtained in air for the CNC-APTES and CNC-GA where the residual mass increased after GA modification. So, this could be mainly attributed to the sample gas atmosphere as there are no oxidation reactions in Ar atmosphere. The slightly higher value observed in CNC-APTES Ar run could be attributed to the Si residue which decreases in percentage with GA functionalization. The initial loading mass was 116 mg. The mass at the end of 120 °C hold was around 8 mg and the final residual mass was therefore 2.4 mg. From T_d to 450 °C, the weight loss was 53 % and at higher temperatures from 500-700 °C, the weight loss was 13 % leaving behind a residual weight % of 29.

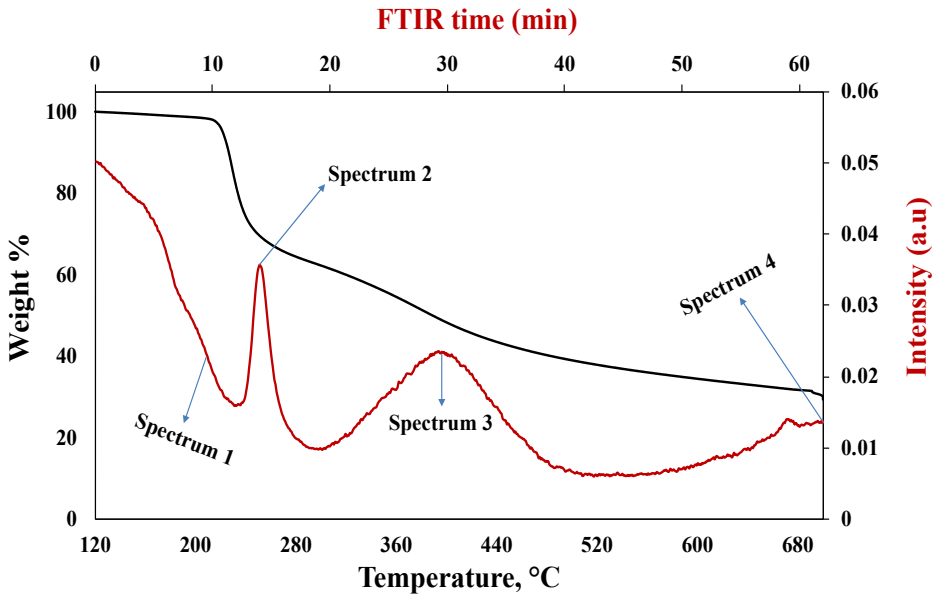

Figure 36 TGA and Gram-Schmidt plots for CNC-GA in Ar

The linked spectra at around 202 °C below in Figure 37A showed evolution of H_2O. The linked spectrum at 245 °C (Figure 37B) showed evolution of H_2O, CO_2 and NO. The linked spectrum at 405 °C (Figure 37C) consisted of H_2O, CO_2 and CO evolution. At 525 °C, the evolution comprised of H_2O, CO_2, CH_4 along with CO (Figure 37D). During the isothermal hold at 700 °C, the linked spectrum collected mainly consisted of CO and CO_2 (Figure 37E).

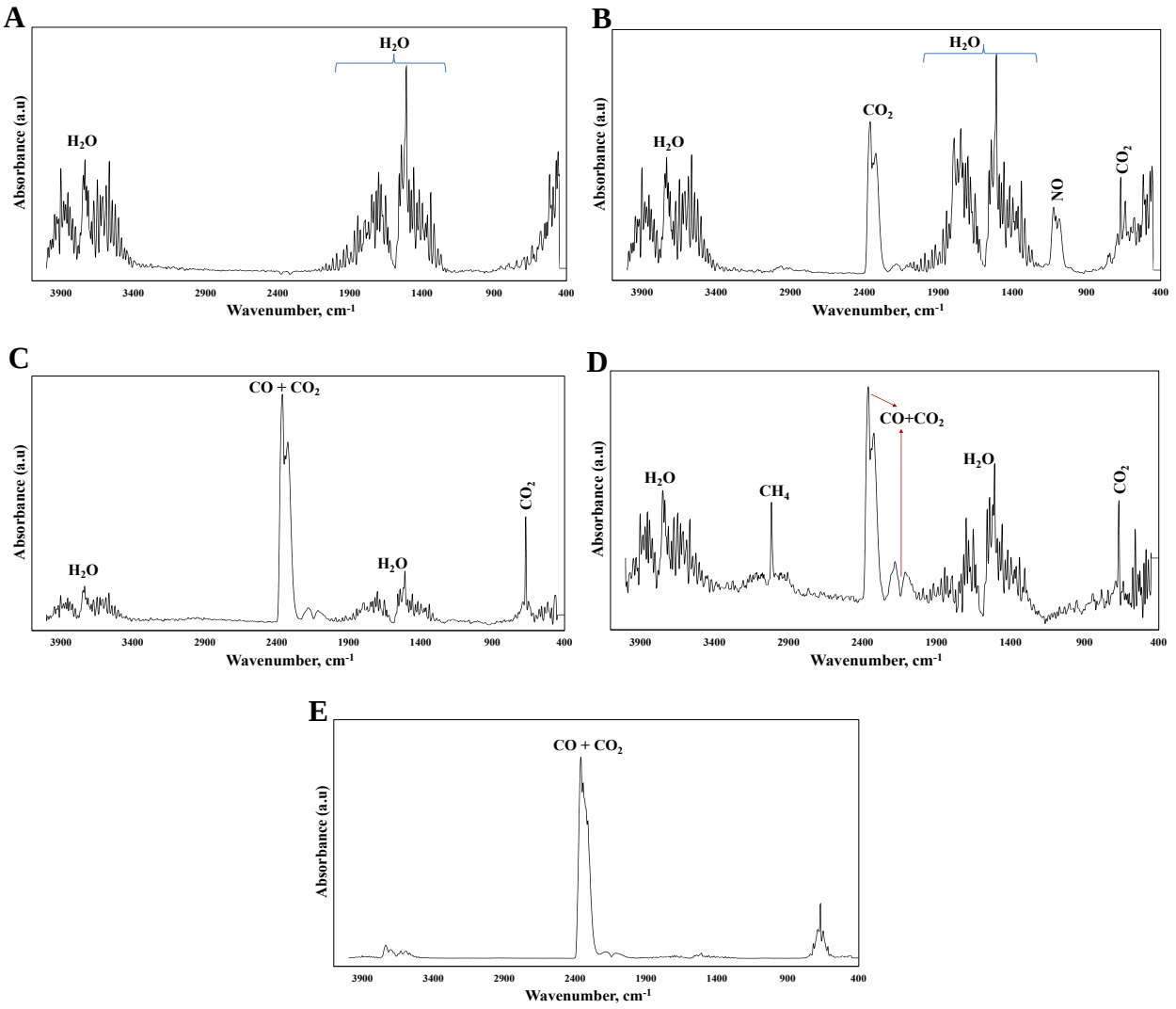

Figure 37 A, B, C and D. FTIR linked spectra of CNC-GA in Ar corresponding to the evolution of various compounds at 202 °C, 245 °C, 405 °C, 525 °C and 700 °C respectively.

After each antibody immobilization and antigen binding, the TGA-FTIR analysis were performed, and they all looked similar. As mentioned earlier, the small amount of immobilized antibody/antigen precludes accurately quantifying the amounts using TGA. For all these dispersions, the sample gas atmosphere was set to air (Figures 38A-F) and the analysis is based on the data/results from a single run. The T_d of CNC-antiCEA (Figure 38A) was approximately 218 °C which is close to the value obtained for the CNC-GA air run. The residual mass at the end of 700 °C was 7 %. This decrease was assumed to have occurred due to the added protein denaturation.[130] The antibody addition would reduce the overall weight percentage of the thermally stable groups from the previous steps. At lower temperatures (<150 °C), the major weight loss was attributed to the water and other dehydration processes from the various groups present. The linked spectra for the temperatures until around 316 °C and below showed evolution of CO_2 (Figure 39A). Since the antibodies are comprised of a large number of N and C terminals, the combustion products namely N_2O, CO, CO_2 etc. along with H_2O (oxidation) were the evolution gases at temperatures >500 °C until 700 °C from the linked spectra presented in Figure 39B and 39C.

This trend of gaseous evolution was very similar for all the rest of the samples CNC-antiAFP, CNC-antiPSA, CNC-CEA, CNC-AFP, and CNC-PSA. The T_d of the CNC-antiAFP and CNC-antiPSA were 220 °C and 217 °C respectively (Figure 38B and 38C), and the residual mass of both were around 8 wt.%. The T_d's of the CNC-CEA, CNC-AFP and CNC-PSA were 121 °C, 190 °C and 217 °C respectively (Figure 38D-F); and their residual masses were around 5 %, 14 %, and 13 % respectively. The T_d value was lower in case of CNC-CEA which was unexpected, and the exact reason for this was unknown. For all of these dispersions after antibody immobilization and antigen binding, the actual masses at different points were mentioned in Table 4. The residual masses and percentage weight losses of each of the samples in both air and Ar

discussed in this section were also tabulated in Table 4. Since the antibody immobilized CNC and the antigen bound CNC were only analyzed using TGA in air, the Ar columns were left blank in each category of Table 4.

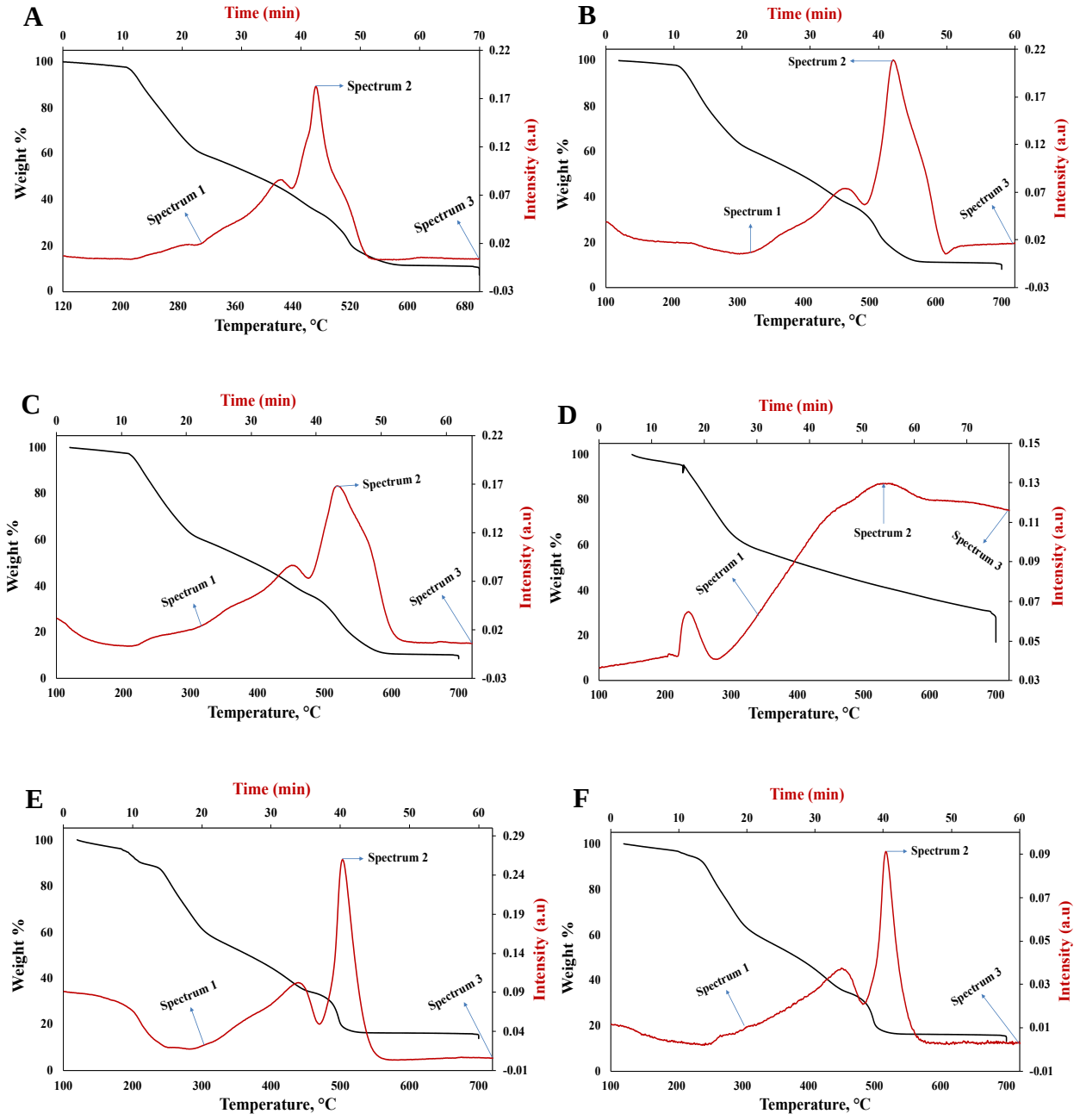

Figure 38 TGA and Gram-Schmidt plots conducted in air for, A. CNC-antiCEA, B. CNC-antiAFP, C. CNC-antiPSA, D. CNC-CEA, E. CNC-AFP, F. CNC-PSA

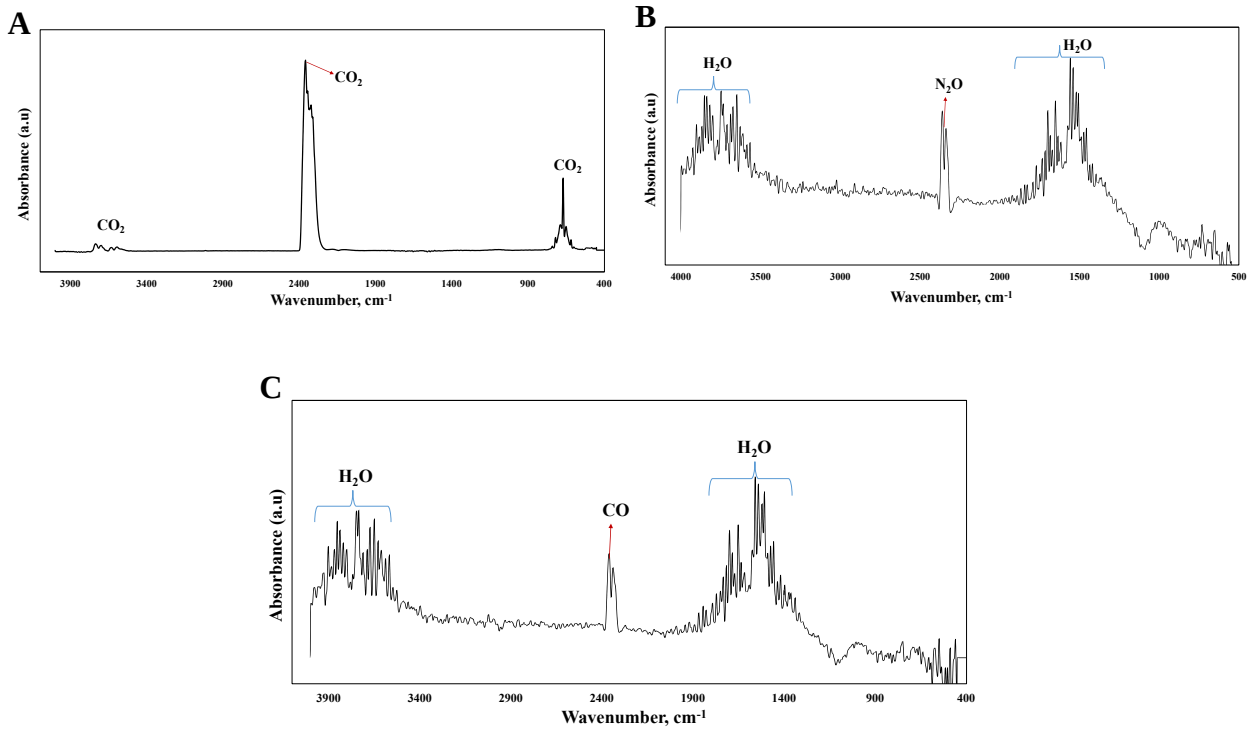

Figure 39 FTIR linked spectra common to all samples above (Figures 38A-F) at temperatures, A. 316 °C, and B. 500 °C, and C. 700 °C

All the values presented below in the Tables 4 and 5 are based on the results from the final repetitions (if there were any) as discussed in this section under each sample analysis.

Table 4 TGA sample masses at various temperatures for the dispersion modified CNC at each step conducted in air and Ar atmosphere.

Sample	Initial mass (mg)		Mass at the end of 120 °C hold (mg)		Residual mass (mg)	
	In air	In Ar	In air	In Ar	In air	In Ar
CNC	120	106	13	12	0.2	3
CNC-APTES	98	108	8	9	0.2	3
CNC-GA	140	116	14	8	2	2.4
CNC-antiCEA	67	-	7	-	0.5	-
CNC-antiAFP	87	-	8	-	0.6	-
CNC-antiPSA	118	-	12	-	1	-
CNC-CEA	129	-	32	-	1.5	-
CNC-AFP	152	-	9.5	-	1.3	-
CNC-CEA	125	-	9	-	1	-

Table 5 TGA percentage weight losses between various temperature points and final residual weights for the dispersion modified CNC at each step conducted in air and Ar atmosphere.

Sample	Weight loss (%)				Final Residual weight (%)	
	From T_d* to 450 °C		450 °C – 700 °C			
	In air	In Ar	In air	In Ar	In air	In Ar
CNC	73	55	20	14	2	26
CNC-APTES	58	52	34	11	3	32
CNC-GA	55	53	28	13	12	29

*T_d corresponds to 5 % mass loss in the sample after 120 °C isothermal hold

4.5.3. Following layers interaction by QCM-D

The film-modification reactions were followed in the 1 & 2 chambers while the dispersion modification reactions were followed in 3 & 4 chambers for the three biomarker cases (CEA, AFP & PSA) of our interest. So, a total of four reaction methods were followed in the four different chambers in order to detect each biomarker. In Method 1, the CNC dispersion was spin-coated on the QCM sensor which was then modified with APTES, GA and antibodies in order, followed by introduction into QCM-D (*in situ*) for antigen detection (see Figure 40A). Method 2 was similar to Method 1 until the APTES step after which the sensor was introduced *in situ* to perform the rest of the steps (see Figure 40B). In Method 3, all the reactions until antibody immobilization were performed on dispersed CNC. The antibody-immobilized CNC dispersions were spin-coated on the sensor surfaces followed by antigen detection *in situ* (see Figure 40C). In Method 4, the dispersion modified CNC until the antibody immobilization step was directly passed *in situ* followed by antigen detection *in situ* (see Figure 40D). These methods were followed for all the three model cancer antibodies and antigens that were discussed earlier. Hence, there are a total of twelve reactions data from QCM-D and the analysis was based on the results or data obtained from one set of experiments without repetitions except for the CEA antigen detection reactions.

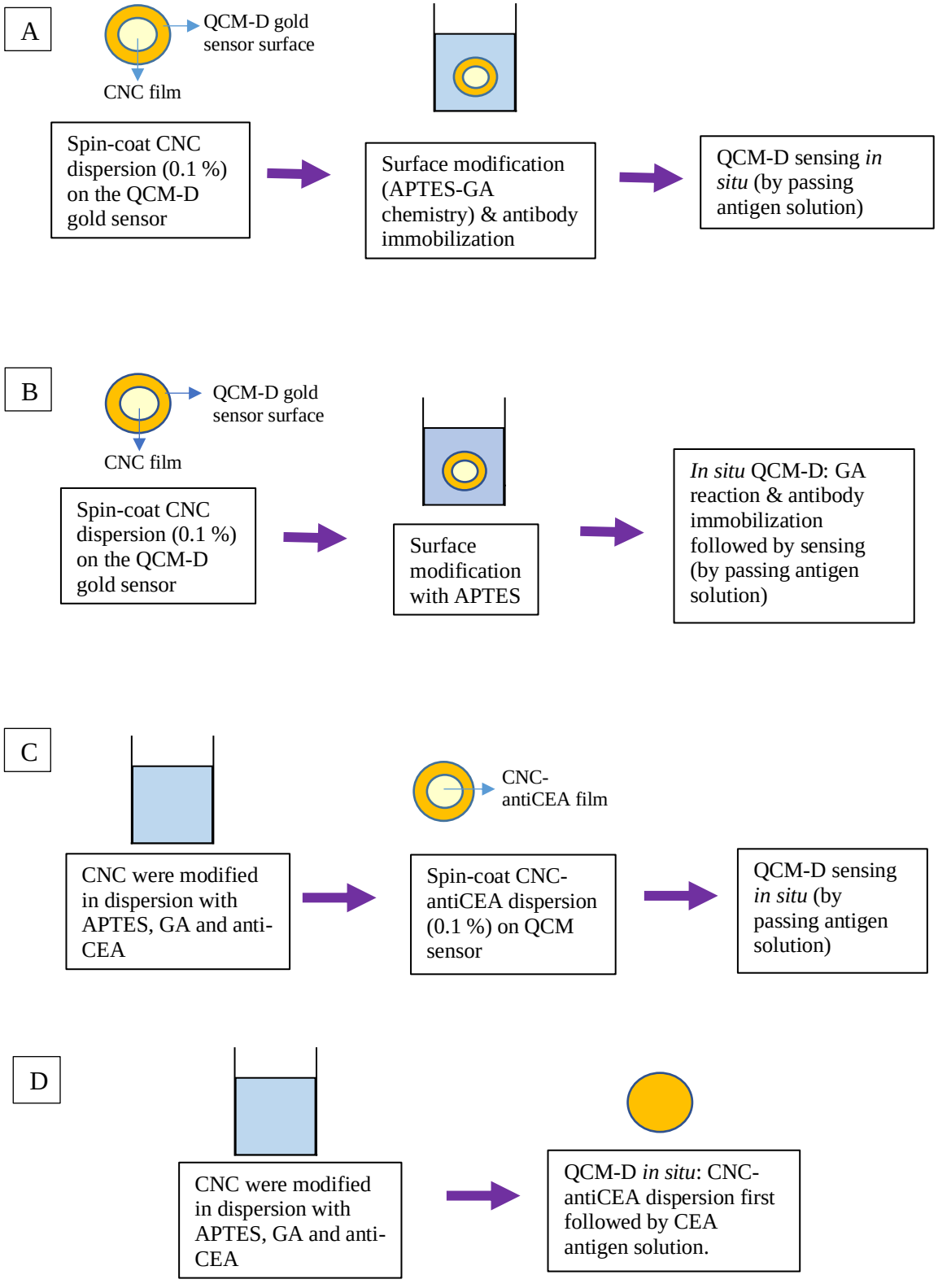

Figure 40 A. Film modification reaction in QCM-D chamber 1- Method 1, B. Film modification reaction in QCM-D chamber 2 - Method 2, C. Dispersion modification reaction in QCM-D chamber 3 - Method 3, D. Dispersion modification reaction in QCM-D chamber 2 - Method 4

The CEA detection for the first set of experiments were conducted in QCM-D using the spray-dried CNC powder as the starting material following the method described in Section 4.4. From the results, it was hard to comment on the amounts of antigen adsorption in the Methods 1 and 2 which correspond to the film modification reactions. This was because the frequency decreases and accompanying mass increases was negligible. However, the amounts of antigen adsorbed using the dispersion modification reactions, Methods 3 and 4 were 194 and 110 ng/m^2 respectively. Following this, the CEA detection was repeated along with AFP and PSA detection by starting with the CNC suspension (batch # 2018-FPL-CNC-126).

Figures 41A-D correspond to all the reactions following four methods leading to the biomarker CEA detection on the CEA antibody immobilized CNC. In all the figures, the arrow marks point towards the frequency shift during the antigen detection reaction when a particular antigen solution in PBS was passed through the sensor surfaces. There was the respective solvent flush before and after each reaction step in QCM-D. The pre-flush (before a reaction) was performed to stabilize the adhered layers in that particular solvent in which the following reaction would be performed. And the post flush was performed to ensure the bonding of the reagents as a result of the reaction was strong enough. If there is an accompanying mass loss during the post flush, which is accompanied by the increase in frequency, it indicates that the reagents are not strongly bound to the surface layer. Hence, this mass loss was taken into consideration while calculating the mass of a particular reagent layer adhering to the surface using Dfind software.

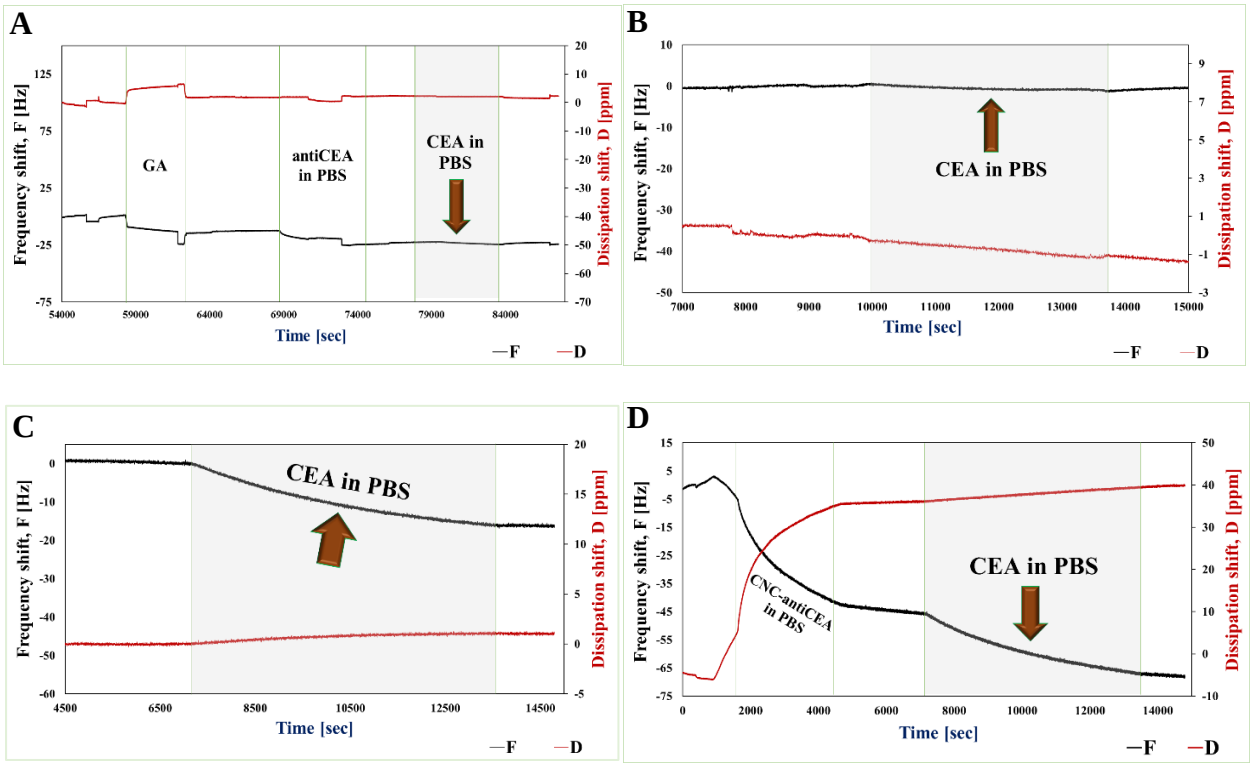

Figure 41 QCM-D frequency and dissipation shifts from CNC surface modification with the biomarker CEA for: A. Method 1, B. Method 2, C. Method 3, and D. Method 4.

Similarly, Figures 42A-D and 43A-D correspond to the biomarkers AFP and PSA detection reactions in QCM-D. In addition, the Sauerbrey equation was used to quantify the sensing capabilities or the antibody-antigen binding in terms of the mass and thickness of the antigen layer adsorbed on the CNC-antibody sensors. The results are tabulated in Table 6 and the analysis was based on the results from the single set of experiments. In case of all the three biomarkers, the dispersion modified CNC has better sensing performance as compared to the film modified ones. Also, in the dispersion modified cases (Methods 3 & 4) for all the three biomarkers, the sensitivity of the CNC-antiCEA sensor was the highest particularly in Method 4.

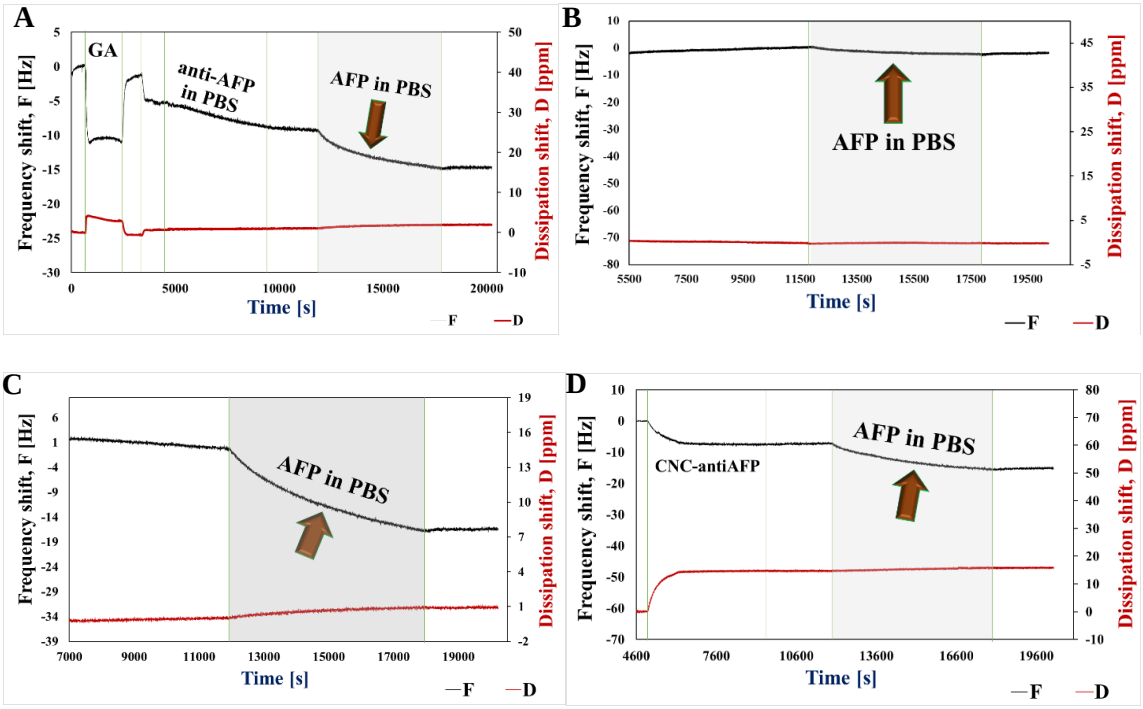

Figure 42 QCM-D frequency and dissipation shifts from CNC surface modification with the biomarker AFP for A. Method 1, B. Method 2, C. Method 3, and D. Method 4.

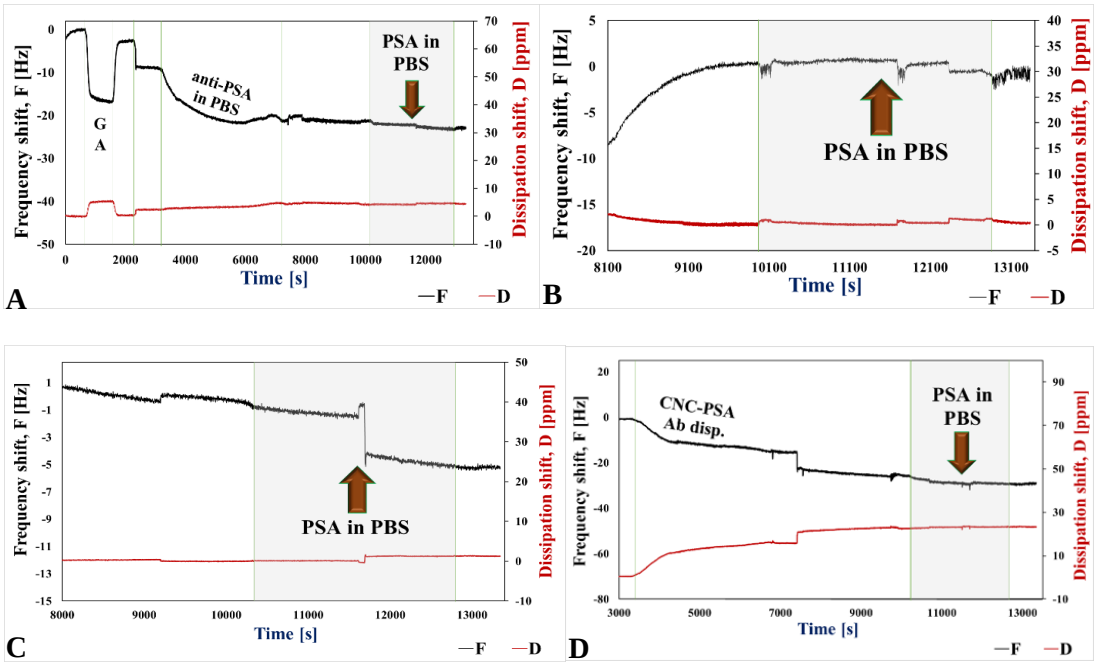

Figure 43 QCM-D frequency and dissipation shifts from CNC surface modification with the biomarker PSA for A. Method 1, B. Method 2, C. Method 3, and D. Method 4.

Table 6 Quantification of antigen layer binding onto the antibody immobilized CNC from QCM-D

Method	AFP		PSA		CEA	
	Mass of antigen adsorbed [ng/m^2]	Thickness of the antigen layer [nm]	Mass of antigen adsorbed [ng/m^2]	Thickness of the antigen layer [nm]	Mass of antigen adsorbed [ng/m^2]	Thickness of the antigen layer [nm]
1	7	0.3	2	0.05	10	0.05
2	103	1.25	27	1.5	33	0.25
3	286	1.8	75	0.75	**300**	2.6
4	133	0.8	51	0.35	**6322**	70

One other important observation is that in case of the biomarkers AFP and PSA, Method 3 showed higher sensitivity than the Method 4, as seen from the values of these antigens adsorbed. This trend was contradictory for the biomarker CEA case where the antigen adsorption was the highest in Method 4. This abnormality could be because of the differences in the formation of the surface while spin coating in Method 3 during the CEA run. The masses of reagents adsorbed during the other reaction steps conducted in QCM-D such as GA and antibody reactions for each biomarker detection case were also quantified. These results were presented below in Table 7. Methods 1 and 3 only have the antigen reactions which were conducted *in situ* whose masses were quantified already as shown in Table 6. So, in the below table the masses from reactions conducted using Methods 2 and 4 were presented. In all of the Methods, the APTES reaction was conducted outside and so only the masses from GA and antibody reactions were given below.

Table 7 Quantification of GA and antibody immobilization reactions from QCM-D in Methods 2 and 4

Method	Mass of the reagent adsorbed [ng/m^2]					
	GA	Antibody CEA	GA	AFP	GA	Antibody PSA
2	100	320	18	60	39	174
4	-	5602	-	42	-	124

4.5.4. Specificity experiments using QCM-D

The specificity experiments were conducted only on the dispersion modified CNC in QCM-D and particularly following the procedure described for Method 3. They were performed in three different sets for the three different antibody-antigen pairs. The first set was aimed to check the CEA pair specificity, second – AFP pair specificity and the third – PSA pair specificity. For each of these tests, the dispersions CNC-antiCEA, CNC-antiAFP and CNC-antiPSA were prepared following the immobilization scheme in dispersion (as discussed in Section 4.5). These three dispersions were then spin-coated onto three Qsense gold sensors and introduced into the three QCM-D chambers in the same order. PBS was flushed through all of these chambers until the frequency curve remained stable. The antigen solution was prepared by dispersing it in PBS. In the first set of reactions, the antigen CEA solution was passed through the three sensors with the layers CNC-antiCEA, CNC-antiAFP and CNC-antiPSA. The resulting layers after the antigen CEA immobilization reaction were labeled as CNC-CEA, CNC-antiAFP-CEA and CNC-antiPSA-CEA. After the frequency got stabilized, the solvent PBS flush was performed to track any mass variations. This similar technique was followed for the second and third sets of reactions using the remaining antigens AFP and PSA respectively. After all the reactions, there were nine sensors in total which are as follows (in order) -

Reaction Set 1: CNC-CEA, CNC-antiAFP-CEA and CNC-antiPSA-CEA

Reaction Set 2: CNC-antiCEA-AFP, CNC-AFP and CNC-antiPSA-AFP

Reaction Set 3: CNC-antiCEA-PSA, CNC-antiAFP-PSA and CNC-PSA

The QCM-D plots for the above nine cases are displayed below (Figures 44A-I) and a tabulated column with the masses and thickness of the antigen layers were also presented (Table 8). The most desired scenario is that the sensors CNC-antiCEA, CNC-antiAFP, and CNC-antiPSA would show the highest detection capabilities/frequency drops towards CEA, AFP and PSA detection respectively. All of these results and discussion were based on single set of experiments.

From the quantified results, the CEA antigen is attaching to all the three antibody immobilized sensor surfaces (CNC-antiCEA, CNC-antiAFP and CNC-antiPSA) with the highest mass on CNC-antiPSA instead of CNC-antiCEA). This could mean that the antibody PSA is cross-reacting with the antigen CEA. It can also be inferred from the respective plots (Figure 44C) that the frequency shift is steep in case of CNC-antiPSA-CEA as compared to the other two. In the second reaction set, which corresponds to the AFP attachment, the lowest mass was recorded on the CNC-antiAFP sensor, which was unexpected. The mass of the AFP attached on the CNC-antiPSA sensor (115 ng/m^2) was the highest followed by CNC-antiCEA (106 ng/m^2). So, the antibody AFP is cross-reacting with both the antigens CEA and PSA. In the third reaction set, which corresponds to PSA antigen interaction on the three surfaces, CNC-antiPSA showed the highest positive signal (PSA mass = 312 ng/m^2) with antigen PSA.

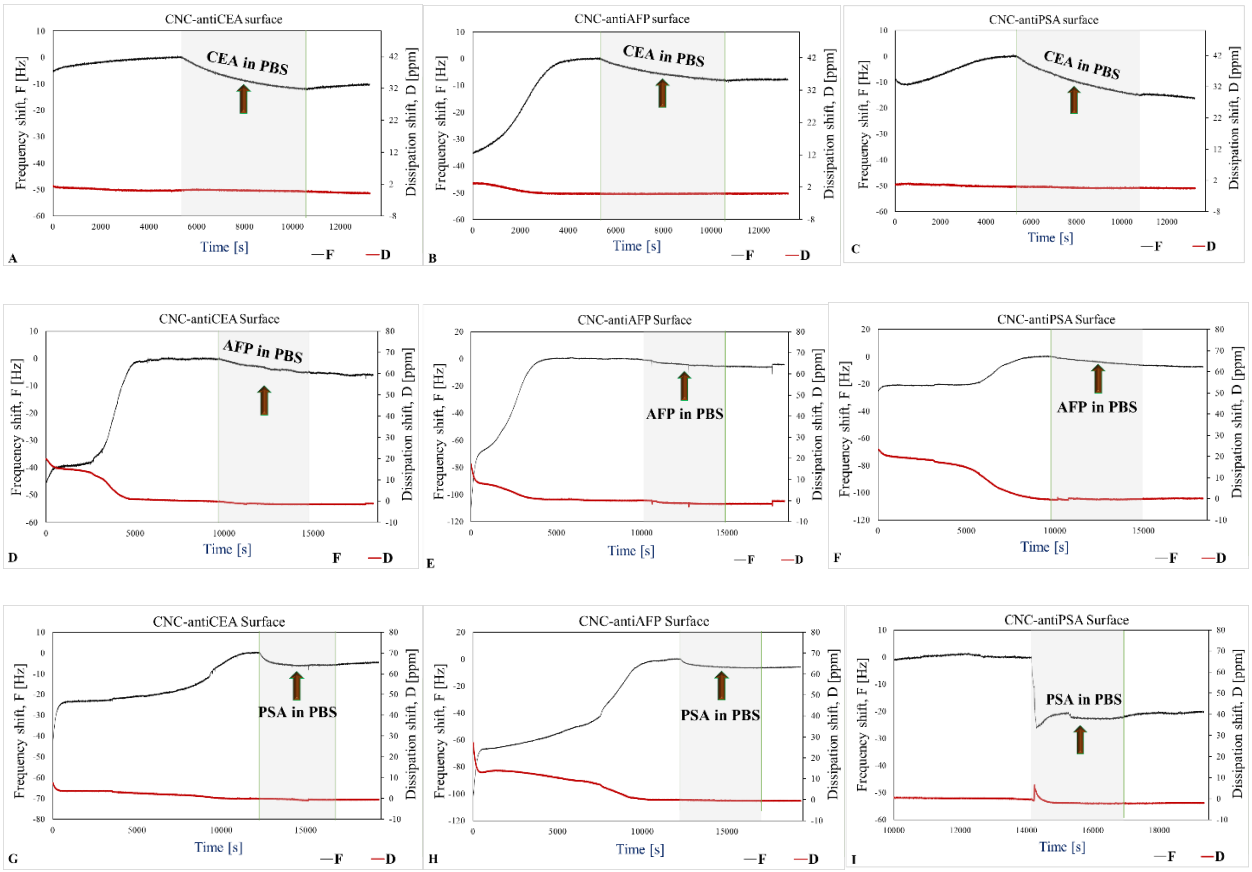

Figure 44 QCM-D Specificity plots on the sensor surfaces, A. CNC-antiCEA reacted with CEA, B. CNC-antiAFP reacted with CEA, C. CNC-antiPSA reacted with CEA antigen, D. CNC-antiCEA reacted with AFP, E. CNC-antiAFP reacted with AFP, F. CNC-antiPSA reacted with AFP, G. CNC-antiCEA reacted with PSA, H. CNC-antiAFP reacted with PSA, and I. CNC-antiPSA reacted with PSA.

Adding another dimension to this data, when we compare the different antigens binding on the CNC-antiCEA surface from the Table 8, the mass of the CEA adsorbed is the highest which is 200 ng/m^2 as compared to AFP and PSA which were 106 and 93 ng/m^2. When looked in the same way, the CNC-antiPSA sensor surface is again more specific to its immunogen PSA as compared to other antigens. The CNC-antiAFP surface is not specific in either way.

The Method 3 in Table 6 data which corresponds to the adsorption of a specific antigen to its respective antibody can be compared with the same in Table 8. The concentrations of the dispersions spin-coated on top of the sensor surface was the same in both of these cases. The

masses of CEA and AFP adsorbed on CNC-antiCEA and CNC-antiAFP surfaces respectively decreased in the specificity tests (Table 8) as compared to the same in Table 6. However, the mass of PSA adsorbed on to the CNC-antiPSA increased remarkably (from 75 ng/m^2 to 312 ng/m^2) in the specificity runs as compared to the original runs. The exact reason for this anomaly was unknown and was assumed to be because of the model fitting. So, more repetitions need to be performed in the future to understand and resolve this issue.

Table 8 Specificity tests – Mass and thickness of the antigen layers (CEA, AFP & PSA)

Sensor surface	**CEA antigen layer**		**AFP antigen layer**		**PSA antigen layer**	
	Mass of antigen adsorbed [ng/m^2]	Thickness of the antigen layer [nm]	Mass of antigen adsorbed [ng/m^2]	Thickness of the antigen layer [nm]	Mass of antigen adsorbed [ng/m^2]	Thickness of the antigen layer [nm]
CNC-antiCEA	200	0.8	106	0.7	93	0.6
CNC-antiAFP	141	0.56	76	0.5	102	0.64
CNC-antiPSA	276	1.1	115	0.7	**312**	2

The cross-reactivity behaviors of the antibodies with other antigens was unexpected as they were monoclonal. Cross-reactivity was often found to be predominant with several monoclonal antibodies including CEA and PSA that were used in this study. Many human antibodies have been reported to possess significant cross-reactivity with the homologous proteins in non-human models, such as a mouse, rat, monkey etc.[131-135] A few articles also discuss this similar issue of cross-reactivity of the CEA and PSA human monoclonal antibodies with other human kallikrein derived antigens.[136-138] The cross-reactivity depends on the extent of protein sequence similarity (homology) between the immunogen and the potential cross-reactive protein. In general, cross-

reactivity can occur if the sequence of the immunogen and the potential cross-reactive protein share 75% sequence homology.

The five immunoglobulin classes (isotypes) of antibody molecules found in serum are IgG, IgM, IgA, IgE and IgD. The antibodies used in this study belong to the isotype IgG which is distinguished by the presence of heavy chains called γ-chains. IgG is the most prevalent antibody in mammalian tissue and cross-reactivity was reported in assays using such tissue-derived samples with the entire Igs, as primary immunoglobulins. Therefore, use of fragments, rather than entire Igs, as primary immunoglobulins could be one approach to prevent cross-reactivity.

All of the antibodies that were used in this study namely CEA, AFP and PSA were obtained from Bioss as discussed in Section 3.1. All the antibodies were produced in vivo with the help of the mouse immune system. Their specification from the seller website mentioned that the antibodies CEA and PSA have reactivity to human species antigens, and AFP possesses reactivity to both human and rat antigens. Reactivity to a species/group of species means that the antibodies have manifested cross-reactivity behaviors with the homologous target antigens from these species. So, in this scenario, the antibodies CEA, AFP and PSA can recognize epitopes that are alike in all the human species antigens. It also means that the cross-reactivity with antigens of other mammalian species was not tested and is quite likely to occur.

The use of the secondary antibody specific to the primary antibody can overcome species cross-reactivity and increases specificity. Various polyclonal antibodies which come under cross-adsorbed secondary antibodies are specially synthesized with an additional purification step in order to remove the members in the antibody that bind to off-target species of immunoglobulin (IgG) class. There are different protocols in choosing the suitable secondary antibody depending

on the experiment set up (for example, the secondary antibody should be chosen coming from a different host).

However, cross-reactivity is not always an undesired property as it can improve an antibody's scope of application in recognizing other biomarkers. Therefore, future research should consider potential cross-reactivity between chosen antibodies based on the specific research goals.

4.5.5. Anisotropic fluorescence

The anisotropy values for PBS and CNC-GA were zero while they showed some fluorescence intensities from the Table 9. Since all the antibodies have fluorescent labels conjugated directly to them, the fluorescence intensity readings were taken for the solvent PBS, CNC-GA and following the antibody immobilization. The fluorescence intensity measurements confirm the successful antibody reaction in all the three cases from the increase in fluorescence intensities after antibody immobilization. The decrease after the antigen reaction is observed in almost all the cases and it does not relate to the antibody-antigen binding. Therefore, fluorescence anisotropy measurements were performed to confirm the successful antibody-antigen binding. The anisotropy was also used to detect the specificity of a particular antibody to its respective antigen and any cross-reactivity behavior with other antigens. This common ID, CNC-antibody-antigen was used for all the possible combination reactions between any two non-specific antibody-antigen pairs. For example, the label for the sample CNC-antiCEA-AFP denotes the CEA immobilized CNC that was reacted with AFP antigen.

As discussed in the experimental section, the samples CNC-CEA, CNC-AFP and CNC-PSA correspond to the corresponding antibody-antigen binding. The anisotropy results and fluorescence intensities were tabulated (Table 9). In all the anisotropy readings, since the amount

of antibody and antigen used are negligible in comparison to the bulk CNC-GA, the changes in anisotropy between the CNC-antibody and CNC-antigen samples were low.[117] The anisotropy experiments were conducted on the dispersions from two different batches of reaction to check the repeatability as shown in the table and the 2 sets of data were labeled as 'Anisotropy 1 and 'Anisotropy 2'. One anisotropy reading per sample in each of these two batches was taken. The associated error was based on the minimum and maximum values. From the results shown in Table 9, the anisotropy increase from CNC-antiCEA to CNC-CEA was the highest as compared to the other antibody-antigen pairs. However, the associated error obtained in the case of CNC-CEA was also the highest. In the other two cases, CNC-antiAFP and CNC-antiPSA showed highest affinity to their immunogens AFP and PSA respectively, but the associated error was high. So, it was hard to conclude that each of these antibodies were specific to their immunogens.

Table 9 Fluorescent intensities and anisotropy measurements for two batches of dispersions

Sample ID	Fluorescence intensity	Aniso. 1	Aniso. 2	Avg.	Min	Max	(+) Error	(-) Error
PBS	0	0	0	0	0	0	0	0
CNC-GA	75	0	0	0	0	0	0	0
CNC-antiCEA	193	0.2	0.1	0.2	0.1	0.2	0.1	0.1
CNC-CEA	113	1	0.1	0.7	0.1	1	0.6	0.6
CNC-antiCEA-AFP	142	0.2	0.1	0.1	0.1	0.2	0.1	0.1
CNC-antiCEA-PSA	174	0.2	0.1	0.2	0.1	0.2	0.1	0.1
CNC-antiAFP	180	0.1	0	0.1	0	0.1	0.1	0.1
CNC-AFP	61	0.3	0	0.2	0	0.3	0.1	0.1
CNC-antiAFP-PSA	144	0.1	0	0.1	0	0.1	0	0
CNC-antiAFP-CEA	139	0.2	0	0.1	0	0.2	0.1	0.1
CNC-antiPSA	341	0.2	0.2	0.2	0.2	0.2	0	0
CNC-PSA	271	0.3	0.1	0.2	0.1	0.3	0.1	0.1
CNC-antiPSA-CEA	222	0.2	0.1	0.1	0.1	0.2	0	0
CNC-antiPSA-AFP	245	0.2	0.1	0.1	0.1	0.2	0.1	0.1

The reason for the huge error was assumed to be arising from the difference in sample batches. Therefore, the next set of measurements were obtained from a single batch which considerably reduced errors. A new reaction batch was generated, and each resulting sample was divided into four portions. The anisotropy of these four portions was measured individually which

allowed to obtain four repetitive readings on a single sample. Further, this procedure can also take into account the instrument biases and any errors as these portions came from the same sample. The anisotropy data of all the antibody/antigen reacted dispersions were tabulated as shown in the Table 10 below.

Table 10 Anisotropy readings for CNC-antibody and CNC-antigen dispersions from single batch

Sample	Fluorescence Anisotropy				Average	Standard Deviation
	Load 1	Load 2	Load 3	Load 4		
CNC-antiCEA	0.029	0.042	0.043	0.102	0.054	0.033
CNC-CEA	0.390	0.312	0.330	0.304	0.334	0.039
CNC-antiCEA-AFP	0.330	0.289	0.283	0.347	0.312	0.031
CNC-antiCEA-PSA	0.245	0.316	0.331	0.360	0.313	0.049
CNC-antiAFP	0.144	0.162	0.173	0.173	0.163	0.014
CNC-AFP	0.187	0.361	0.109	0.197	0.214	0.106
CNC-antiAFP-CEA	0.188	0.202	0.175	0.186	0.188	0.011
CNC-antiAFP-PSA	0.176	0.146	0.210	0.159	0.173	0.028
CNC-antiPSA	0.018	0.170	0.172	0.134	0.124	0.072
CNC-PSA	0.192	0.136	0.182	0.182	0.173	0.025
CNC-antiPSA-CEA	0.253	0.233	0.027	0.256	0.192	0.111
CNC-antiPSA-AFP	0.272	0.238	0.239	0.335	0.271	0.045

Figure 46A corresponds to the anisotropy measurements to check the specificity and cross-reactivity of the antibody CEA towards antigens CEA, AFP and PSA. There was a significant increase in anisotropy after the antigens binding to the CNC-antiCEA. The average anisotropy of the CNC-CEA was higher than the CNC-antiCEA-AFP and CNC-antiCEA-PSA which means that the affinity of the antibody CEA to its immunogen CEA is the highest. From Figure 46B, the increase in anisotropy from CNC-antiAFP and CNC-AFP was also highest as compared to CNC-antiAFP-CEA and CNC-antiAFP-PSA, but the associated error was huge. From the Figure 46C, the antibody PSA showed higher affinity towards antigen AFP followed by the antigen CEA. The affinity of the antibody PSA towards its immunogen PSA was the least as

observed from the bar graph as compared to the other two antigens. So, the antibody PSA was not specific to its antigen PSA and cross-reacted with the CEA and AFP. Although the antibody AFP showed highest affinity to AFP, the associated error was huge which made it difficult to confirm the specificity. Therefore, only the antibody CEA showed specificity to its antigen CEA. The anisotropy results were close to the results that were obtained from the QCM-D specificity tests. Both QCM-D and FA show that the antibody CEA possesses highest affinity to its immunogen CEA.

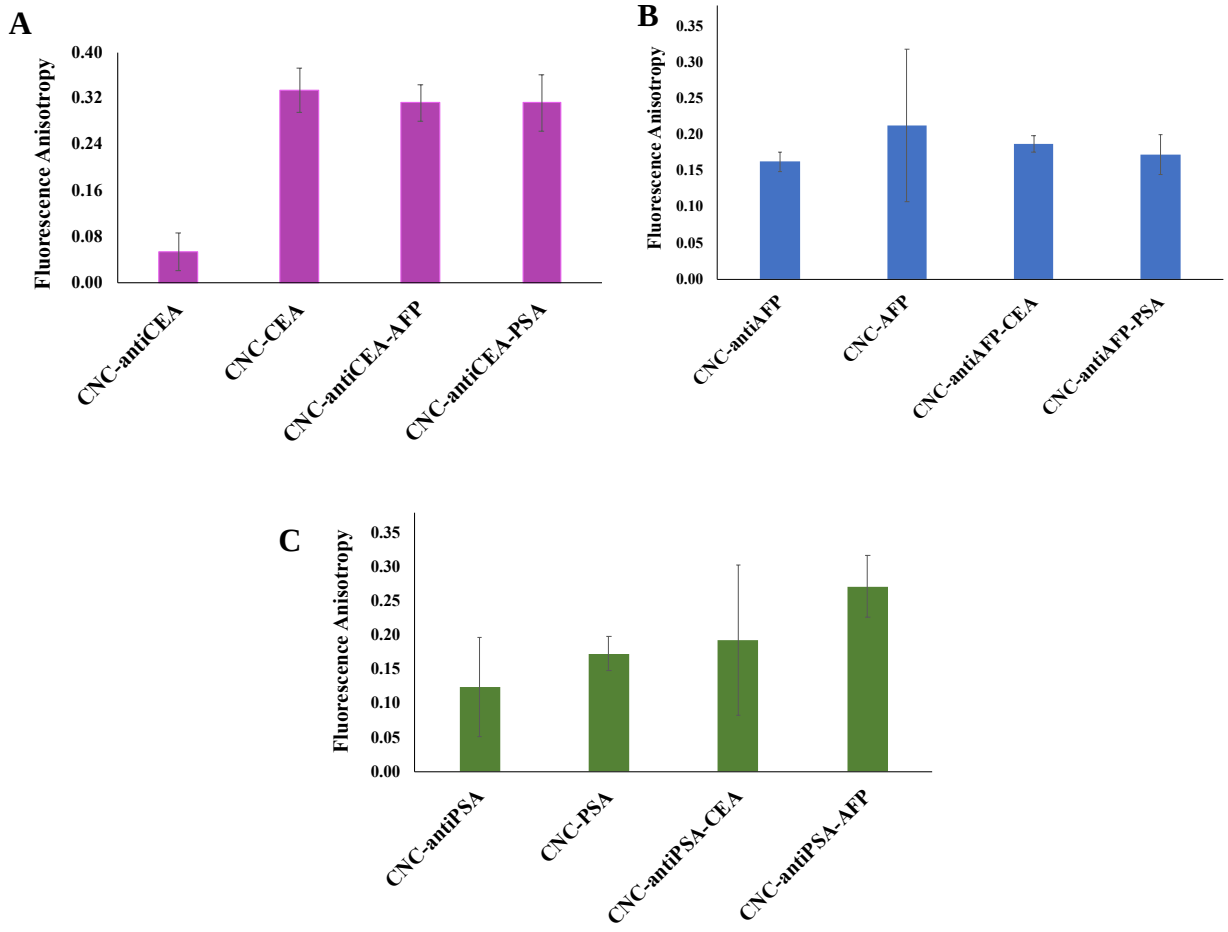

Figure 45 Fluorescence Anisotropy measurements for confirming- A. antiCEA-CEA specificity, B. antiAFP-AFP specificity, and C. antiPSA-PSA specificity, on the CNC

Chapter 5. Conclusions

This work demonstrates antibody immobilization on dispersed cellulose nanocrystals using APTES-GA chemistry. The APTES functionalization was not successful when performed by a simple method using water as a solvent. In contrast, the method adapted from Saha *et al.*[15] was complicated and created large aggregates but successfully imparted the amino functionalization on to CNC which was confirmed by FTIR. Finally, a method modified from Kargarzadeh *et al.*[19] imparted the amino functionalization on the CNC surface in a way that was simple and resulted in significantly less aggregation even for dispersion concentrations up to 6 wt.%. The analysis of aggregates for each of these different approaches was mainly visual examination using optical microscopy and SEM. FTIR functionalization was used to confirm the APTES-GA reaction chemistry and antibody immobilization. TGA-FTIR analysis at each step for CNC, CNC-APTES, CNC-GA, CNC-antibody (antiCEA, antiAFP, and antiPSA) and CNC-antigen (CEA, AFP, and PSA), provided the thermal degradation properties and information on the functional groups from the evolved gas IR spectra. QCM-D experiments were used to quantify each step of the CNC modification scheme including antibody immobilization and antigen binding. It also highlighted the advantage of modifying dispersed CNC instead of assembled films; more binding was achieved on dispersion modified CNC due to the entire surface being accessible for antibody immobilization. In terms of antibody-antigen binding, the greatest binding of ~6000 ng/m^2 was achieved for CEA antigen adsorption on the CNC-antiCEA surface prepared from a dispersion reaction scheme in QCM-D. The maximum detection capabilities of the other two surfaces namely CNC-antiAFP and CNC-antiPSA were 286 and 312 ng/m^2.

From the QCM-D specificity results, the antibody CEA showed highest affinity to CEA as compared to other the two antigens (AFP and PSA). The antibody PSA showed cross-reactivity towards CEA, whereas antibody AFP cross-reacted with both CEA and PSA. From the FA measurements, antibody CEA again showed highest affinity to CEA. There was huge associated error in FA measurements performed to confirm the specificity of antibody AFP to AFP. Finally, antibody PSA showed least affinity to PSA and cross-reacted with CEA and AFP. Therefore, the specificity results obtained from both QCM-D and FA were in close agreement in terms of confirming the specificity of CEA antibody to CEA.

These results of this research highlight that sulfated CNC can be used for antibody immobilization and are an interesting green material for biosensors. It provides a comprehensive idea of the merits and challenges in developing antibody-immobilized CNC surfaces via different methods and potential issues of cross-reactivity for biosensors based on antibody-antigen binding. It provides a first step in developing point of care biosensors for the detection of biomarkers.

References

1. Tothill, I. E., Biosensors for Cancer Markers Diagnosis. *Semin Cell Dev Biol* **2009,** *20* (1), 55-62.

2. Chinen, A. B.; Guan, C. M.; Ferrer, J. R.; Barnaby, S. N.; Merkel, T. J.; Mirkin, C. A., Nanoparticle Probes for the Detection of Cancer Biomarkers, Cells, and Tissues by Fluorescence. *Chemical Reviews* **2015,** *115* (19), 10530-10574.

3. Mittal, S.; Kaur, H.; Gautam, N.; Mantha, A. K., Biosensors for Breast Cancer Diagnosis: A Review of Bioreceptors, Biotransducers and Signal Amplification Strategies. *Biosens Bioelectron* **2017,** *88*, 217-231.

4. Pan, L. H.; Kuo, S. H.; Lin, T. Y.; Lin, C. W.; Fang, P. Y.; Yang, H. W., An Electrochemical Biosensor to Simultaneously Detect VEGF and PSA for Early Prostate Cancer Diagnosis Based on Graphene Oxide/SSDNA/PLLA Nanoparticles. *Biosens Bioelectron* **2017,** *89* (Pt 1), 598-605.

5. Vasan, A. S. S.; Mahadeo, D. M.; Doraiswami, R.; Huang, Y.; Pecht, M., Point-of-Care Biosensor Systems. *Front Biosci (Schol Ed) 5* **2013**, 39–71.

6. Schyrr, B.; Pasche, S.; Voirin, G.; Weder, C.; Simon, Y. C.; Foster, E. J., Biosensors Based on Porous Cellulose Nanocrystal-Poly(Vinyl Alcohol) Scaffolds. *ACS Appl Mater Interfaces* **2014,** *6* (15), 12674-83.

7. Lin, N.; Dufresne, A., Physical and/or Chemical Compatibilization of Extruded Cellulose Nanocrystal Reinforced Polystyrene Nanocomposites. *Macromolecules* **2013,** *46* (14), 5570-5583.

8. Kaboorani, A.; Riedl, B., Surface Modification of Cellulose Nanocrystals (CNC) by a Cationic Surfactant. *Industrial Crops and Products* **2015,** *65*, 45-55.

9. Yin, Y.; Tian, X.; Jiang, X.; Wang, H.; Gao, W., Modification of Cellulose Nanocrystal Via Si-ATRP of Styrene and the Mechanism of Its Reinforcement of Polymethylmethacrylate. *Carbohydr Polym* **2016,** *142*, 206-12.

10. Clift, M. J.; Foster, E. J.; Vanhecke, D.; Studer, D.; Wick, P.; Gehr, P.; Rothen-Rutishauser, B.; Weder, C., Investigating the Interaction of Cellulose Nanofibers Derived from Cotton with a Sophisticated 3D Human Lung Cell Coculture. *Biomacromolecules* **2011,** *12* (10), 3666-73.

11. Lee, H.-J.; Lee, H.-S.; Seo, J.; Kang, Y.-H.; Kim, W.; Kang, T., State-of-the-Art of Cellulose Nanocrystals and Optimal Method for Their Dispersion for Construction-Related Applications. *Applied Sciences* **2019,** *9* (3).

12. Chang, H.; Luo, J.; Bakhtiary Davijani, A. A.; Chien, A. T.; Wang, P. H.; Liu, H. C.; Kumar, S., Individually Dispersed Wood-Based Cellulose Nanocrystals. *ACS Appl Mater Interfaces* **2016,** *8* (9), 5768-71.

13. Cho, S. Y.; Choi, Y.; Park, D.; Heo, S.; Kim, D. H.; Jin, H.-J., Cellulose Nanocrystals with High Thermal Stability and Their Nanocomposites with Poly (Lactic Acid). In *18th International conference on composite materials: ICCM18, Jeju Island, Korea*, Korean Society of Composite Materials.

14. Khanjanzadeh, H.; Behrooz, R.; Bahramifar, N.; Gindl-Altmutter, W.; Bacher, M.; Edler, M.; Griesser, T., Surface Chemical Functionalization of Cellulose Nanocrystals by 3-Aminopropyltriethoxysilane. *Int J Biol Macromol* **2018,** *106*, 1288-1296.

15. Saha, P. Optimization of Cellulose Nanocrystal Films for Optical and Micromechanical Applications. Ph.D Dissertation, Auburn University, Auburn, Al. **2018**.

16. De Oliveira Taipina, M.; Ferrarezi, M. M. F.; Yoshida, I. V. P.; Gonçalves, M. d. C., Surface Modification of Cotton Nanocrystals with a Silane Agent. *Cellulose* **2013,** *20* (1), 217-226.

17. Pei, A.; Zhou, Q.; Berglund, L. A., Functionalized Cellulose Nanocrystals as Biobased Nucleation Agents in Poly(L-Lactide) (PLLA) – Crystallization and Mechanical Property Effects. *Compos. Sci. Technol.* **2010,** *70* (5), 815-821.

18. Raquez, J. M.; Murena, Y.; Goffin, A. L.; Habibi, Y.; Ruelle, B.; DeBuyl, F.; Dubois, P., Surface-Modification of Cellulose Nanowhiskers and Their Use as Nanoreinforcers into Polylactide: A Sustainably-Integrated Approach. *Composites Science and Technology* **2012,** *72* (5), 544-549.

19. Kargarzadeh, H.; M. Sheltami, R.; Ahmad, I.; Abdullah, I.; Dufresne, A., Cellulose Nanocrystal: A Promising Toughening Agent for Unsaturated Polyester Nanocomposite. *Polymer* **2015,** *56*, 346-357.

20. Kargarzadeh, H.; Sheltami, R. M.; Ahmad, I.; Abdullah, I.; Dufresne, A., Cellulose Nanocrystal Reinforced Liquid Natural Rubber Toughened Unsaturated Polyester: Effects of Filler Content and Surface Treatment on Its Morphological, Thermal, Mechanical, and Viscoelastic Properties. *Polymer* **2015,** *71*, 51-59.

21. Davis, V. A.; Parra-Vasquez, N.; Ericson, L. M.; Ramesh, S.; Saini, R.; Kittrell, C.; Billups, W. E.; Hauge, R. H.; Smalley, R. E.; Pasquali, M. In *Rheology and Phase Behavior of Swnts in Strong Acids: Evidence of Mesophases*, APS March Annual Meeting 2003, Austin, TX, Austin, TX, 2003.

22. Saini, S.; Belgacem, M. N.; Salon, M.-C. B.; Bras, J., Non Leaching Biomimetic Antimicrobial Surfaces Via Surface Functionalisation of Cellulose Nanofibers with Aminosilane. *Cellulose* **2016,** *23* (1), 795-810.

23. Diao, J.; Ren, D.; Engstrom, J. R.; Lee, K. H., A Surface Modification Strategy on Silicon Nitride for Developing Biosensors. *Anal Biochem* **2005,** *343* (2), 322-8.

24. Patel, D. K.; Dutta, S. D.; Lim, K.-T., Nanocellulose-Based Polymer Hybrids and Their Emerging Applications in Biomedical Engineering and Water Purification. *RSC Advances* **2019,** *9* (33), 19143-19162.

25. Joubert, F.; Musa, O. M.; Hodgson, D. R.; Cameron, N. R., The Preparation of Graft Copolymers of Cellulose and Cellulose Derivatives Using ATRP under Homogeneous Reaction Conditions. *Chem Soc Rev* **2014,** *43* (20), 7217-35.

26. Klemm, D.; Kramer, F.; Moritz, S.; Lindstrom, T.; Ankerfors, M.; Gray, D.; Dorris, A., Nanocelluloses: A New Family of Nature-Based Materials. *Angew Chem Int Ed Engl* **2011,** *50* (24), 5438-66.

27. Trache, D.; Hussin, M. H.; Haafiz, M. K.; Thakur, V. K., Recent Progress in Cellulose Nanocrystals: Sources and Production. *Nanoscale* **2017,** *9* (5), 1763-1786.

28. Wang, B.; Sain, M.; Oksman, K., Study of Structural Morphology of Hemp Fiber from the Micro to the Nanoscale. *Applied Composite Materials* **2007,** *14* (2), 89-103.

29. Lin, N.; Dufresne, A., Nanocellulose in Biomedicine: Current Status and Future Prospect. *Eur. Polym. J.* **2014,** *59*, 302-325.

30. Golmohammadi, H.; Morales-Narváez, E.; Naghdi, T.; Merkoçi, A., Nanocellulose in Sensing and Biosensing. *Chemistry of Materials* **2017,** *29* (13), 5426-5446.

31. Nayak, S.; Blumenfeld, N. R.; Laksanasopin, T.; Sia, S. K., Point-of-Care Diagnostics: Recent Developments in a Connected Age. *Anal Chem* **2017,** *89* (1), 102-123.

32. Yetisen, A. K.; Akram, M. S.; Lowe, C. R., Paper-Based Microfluidic Point-of-Care Diagnostic Devices. *Lab Chip* **2013,** *13* (12), 2210-51.

33. Primiceri, E.; Chiriaco, M. S.; Notarangelo, F. M.; Crocamo, A.; Ardissino, D.; Cereda, M.; Bramanti, A. P.; Bianchessi, M. A.; Giannelli, G.; Maruccio, G., Key Enabling Technologies for Point-of-Care Diagnostics. *Sensors (Basel)* **2018,** *18* (11).

34. Moon, R. J.; Martini, A.; Nairn, J.; Simonsen, J.; Youngblood, J., Cellulose Nanomaterials Review: Structure, Properties and Nanocomposites. *Chem Soc Rev* **2011,** *40* (7), 3941-94.

35. Bettaieb, F.; Khiari, R.; Dufresne, A.; Mhenni, M. F.; Belgacem, M. N., Mechanical and Thermal Properties of Posidonia Oceanica Cellulose Nanocrystal Reinforced Polymer. *Carbohydr Polym* **2015,** *123*, 99-104.

36. Lee, K.-Y.; Aitomäki, Y.; Berglund, L. A.; Oksman, K.; Bismarck, A., On the Use of Nanocellulose as Reinforcement in Polymer Matrix Composites. *Composites Science and Technology* **2014,** *105*, 15-27.

37. Jonoobi, M.; Oladi, R.; Davoudpour, Y.; Oksman, K.; Dufresne, A.; Hamzeh, Y.; Davoodi, R., Different Preparation Methods and Properties of Nanostructured Cellulose from Various Natural Resources and Residues: A Review. *Cellulose* **2015,** *22* (2), 935-969.

38. Xu, X.; Liu, F.; Jiang, L.; Zhu, J. Y.; Haagenson, D.; Wiesenborn, D. P., Cellulose Nanocrystals Vs. Cellulose Nanofibrils: A Comparative Study on Their Microstructures and Effects as Polymer Reinforcing Agents. *ACS Appl Mater Interfaces* **2013,** *5* (8), 2999-3009.

39. Orts, W. J.; Shey, J.; Imam, S. H.; Glenn, G. M.; Guttman, M. E.; Revol, J.-F., Application of Cellulose Microfibrils in Polymer Nanocomposites. *Journal of Polymers and the Environment* **2005,** *13* (4), 301-306.

40. Kan, K. H.; Li, J.; Wijesekera, K.; Cranston, E. D., Polymer-Grafted Cellulose Nanocrystals as pH-Responsive Reversible Flocculants. *Biomacromolecules* **2013,** *14* (9), 3130-9.

41. Brown, A.J. Xix. - the Chemical Action of Pure Cultivations of Bacterium Aceti. *J. Chem. Soc. Trans.* **1886**, *49*, 172–187.

42. Panchal, P.; Ogunsona, E.; Mekonnen, T., Trends in Advanced Functional Material Applications of Nanocellulose. *Processes* **2018,** *7* (1).

43. Moon, R. J.; Martini, A.; Nairn, J.; Simonsen, J.; Youngblood, J., Cellulose Nanomaterials Review: Structure, Properties and Nanocomposites. *Chemical Society Reviews* **2011,** *40* (7), 3941.

44. Hubbe, M. A.; Rojas, O. J.; Lucia, L. A.; Sain, M., Cellulosic Nanocomposites: A Review. *2008* **2008,** *3* (3), 52.

45. Siró, I.; Plackett, D., Microfibrillated Cellulose and New Nanocomposite Materials: A Review. *Cellulose* **2010,** *17* (3), 459-494.

46. Iwamoto, S.; Abe, K.; Yano, H., The Effect of Hemicelluloses on Wood Pulp Nanofibrillation and Nanofiber Network Characteristics. *Biomacromolecules* **2008,** *9* (3), 1022-1026.

47. Habibi, Y.; Lucia, L. A.; Rojas, O. J., Cellulose Nanocrystals: Chemistry, Self-Assembly, and Applications. *Chem. Rev.* **2010,** *110* (6), 3479-3500.

48. Zhou, C. J.; Wu, Q. J. Recent Development in Applications of Cellulose Nanocrystals for Advanced Polymer-Based Nanocomposites by Novel Fabrication Strategies. In *Nanocrystals - Synthesis, Characterization and Applications*; Neralla, S., Ed.; Intech, 2012; Pp 103−120.

49. Orts, W. J.; Godbout, L.; Marchessault, R. H.; Revol, J. F., Enhanced Ordering of Liquid Crystalline Suspensions of Cellulose Microfibrils: A Small Angle Neutron Scattering Study. **1998,** *31* (17), 5717-5725.

50. Dong, X. M.; Kimura, T.; Revol, J.-F.; Gray, D. G., Effects of Ionic Strength on the Isotropic−Chiral Nematic Phase Transition of Suspensions of Cellulose Crystallites. *Langmuir* **1996,** *12* (8), 2076-2082.

51. Marchessault, R. H., Morehead, F. F. And Koch, M. J. (1961) Some Hydrodynamic Properties of Neutral suspensions of Cellulose Crystallites as Related to Size and Shape. *J. Colloid Sci*. **16**, 327-344.

52. Revol, J. F.; Bradford, H.; Giasson, J.; Marchessault, R. H.; Gray, D. G., Helicoidal Self-Ordering of Cellulose Microfibrils in Aqueous Suspension. **1992,** *14* (3), 170-172.

53. Berry, G. C.; Wong, C. P.; Venkatamen, S.; Chu, S. G., . *Solution Processing Rod-Like Polymers, Technical Report: Afml-Tr-79-4115*; Air Force Materials Laboratory: Dayton, 1979.

54. Lee, T. M., Over-the-Counter Biosensors: Past, Present, and Future. *Sensors (Basel)* **2008,** *8* (9), 5535-5559.

55. Soper, S. A.; Brown, K.; Ellington, A.; Frazier, B.; Garcia-Manero, G.; Gau, V.; Gutman, S. I.; Hayes, D. F.; Korte, B.; Landers, J. L.; Larson, D.; Ligler, F.; Majumdar, A.; Mascini, M.; Nolte, D.; Rosenzweig, Z.; Wang, J.; Wilson, D., Point-of-Care Biosensor Systems for Cancer Diagnostics/Prognostics. *Biosens Bioelectron* **2006,** *21* (10), 1932-42.

56. Stobiecka, D. M. Biosensors - Lecture. http://stobiecka.net/teaching.htm (accessed Oct 11, 2019).

57. Bhalla, N.; Jolly, P.; Formisano, N.; Estrela, P., Introduction to Biosensors. *Essays In Biochemistry* **2016,** *60* (1), 1-8.

58. Agarwal, A.; Lang, J. H., *Foundations of Analog and Digital Electronic Circuits*. Morgan Kaufmann Publishers: China, 2005; p 973.

59. Dixon, M. C., Quartz Crystal Microbalance with Dissipation Monitoring: Enabling Real-Time Characterization of Biological Materials and Their Interactions. *J Biomol Tech* **2008,** *19* (3), 151-158.

60. C. K. O'sullivan and G. G. Guilbault, "Commercial Quartz Crystal Microbalances—Theory and Applications," Biosensors and Bioelectronics, Vol. 14, No. 8-9, 1999, Pp. 663-670.

61. Lange, K.; Rapp, B. E.; Rapp, M., Surface Acoustic Wave Biosensors: A Review. *Anal Bioanal Chem* **2008,** *391* (5), 1509-19.

62. Arlett, J. L.; Myers, E. B.; Roukes, M. L., Comparative Advantages of Mechanical Biosensors. *Nat Nanotechnol* **2011,** *6* (4), 203-15.

63. Datar, R.; Kim, S.; Jeon, S.; Hesketh, P.; Manalis, S.; Boisen, A.; Thundat, T., Cantilever Sensors: Nanomechanical Tools for Diagnostics. *MRS Bulletin* **2011,** *34* (6), 449-454.

64. Boisen, A.; Thundat, T., Design & Fabrication of Cantilever Array Biosensors. **2009,** *12* (9), 32-38.

65. Boisen, A., Dohn, S., Keller, S. S., Schmid, S., & Tenje, M. (2011). Cantilever-like micromechanical sensors. Reports on Progress in Physics, 74(3), 036101. https://doi.org/10.1088/0034-4885/74/3/036101.

66. Fritz, J., Cantilever Biosensors. *Analyst* **2008,** *133* (7), 855-63.

67. Waggoner, P. S.; Craighead, H. G., Micro- and Nanomechanical Sensors for Environmental, Chemical, and Biological Detection. *Lab Chip* **2007,** *7* (10), 1238-55.

68. Raiteri, R.; Grattarola, M.; Butt, H.-J.; Skládal, P., Micromechanical Cantilever-Based Biosensors. **2001,** *79* (2-3), 115-126.

69. Sapsford, K. E.; Shriver-Lake, L. C., Bacterial Detection Using Evanescent Wave-Based Fluorescent Biosensors. In *Principles of Bacterial Detection: Biosensors, Recognition Receptors and Microsystems*, Zourob, M.; Elwary, S.; Turner, A., Eds. Springer New York: New York, NY, 2008; pp 109-123.

70. Lijmer, J. G.; Bossuyt, P. M. M., Various Randomized Designs Can Be Used to Evaluate Medical Tests. **2009,** *62* (4), 364-373.

71. Yu, X.; Xu, D.; Cheng, Q., Label-Free Detection Methods for Protein Microarrays. *Proteomics* **2006,** *6* (20), 5493-5503.

72. Chamritski, I.; Clarkson, M.; Franklin, J.; Li, S. W., Real-Time Detection of Antigen-antibody Reactions by Imaging Ellipsometry. *Australian Journal of Chemistry* **2007,** *60* (9), 667-671.

73. Ray, S.; Mehta, G.; Srivastava, S., Label-Free Detection Techniques for Protein Microarrays: Prospects, Merits and Challenges. **2010,** *10* (4), 731-748.

74. Ji, J.; O'Connell, J. G.; Carter, D. J. D.; Larson, D. N., High-Throughput Nanohole Array Based System to Monitor Multiple Binding Events in Real Time. *Analytical Chemistry* **2008,** *80* (7), 2491-2498.

75. Vo-Dinh, T.; Cullum, B., Biosensors and Biochips: Advances in Biological and Medical Diagnostics. *Fresenius J Anal Chem* **2000,** *366* (6-7), 540-51.

76. Bashir, R., Biomems: State-of-the-Art in Detection, Opportunities and Prospects. *Adv. Drug Del. Rev.* **2004,** *56* (11), 1565-1586.

77. Kua, C. H.; Lam, Y.; Yang, C.; Youcef-Toumi, K., Review of Bio-Particle Manipulation Using Dielectrophoresis. **2004**.

78. Donald, A. M.; Windle, A. H., *Liquid Crystalline Polymers*. Cambridge University Press: Cambridge, 1992.

79. Rusling, J. F.; Kumar, C. V.; Gutkind, J. S.; Patel, V., Measurement of Biomarker Proteins for Point-of-Care Early Detection and Monitoring of Cancer. **2010,** *135* (10), 2496.

80. Ksv Instruments Ltd. 'What Is a Quartz Crystal Microbalance – QCM'. https://www.chem.uci.edu/~unicorn/243/papers/ksv01.pdf (accessed Oct 11, 2019).

81. Voinova, M. V.; Jonson, M.; Kasemo, B., 'Missing Mass' Effect in Biosensor's QCM Applications. *Biosensors and Bioelectronics* **2002,** *17* (10), 835-841.

82. Voinova, M. V.; Rodahl, M.; Jonson, M.; Kasemo, B., Viscoelastic Acoustic Response of Layered Polymer Films at Fluid-Solid Interfaces: Continuum Mechanics Approach. *Physica Scripta* **1999,** *59* (5), 391-396.

83. Turon, X.; Rojas, O. J.; Deinhammer, R. S., Enzymatic Kinetics of Cellulose Hydrolysis: A QCM-D Study. **2008,** *24* (8), 3880-3887.

84. Ebbesen, T. W.; Ajayan, P. M., Nanotubes. *Nature* **1992,** *358*, 220.

85. Thess, A.; Lee, R.; Nikolaev, P.; Dai, H. J.; Petit, P.; Robert, J.; Xu, C. H.; Lee, Y. H.; Kim, S. G.; Rinzler, A. G.; Colbert, D. T.; Scuseria, G. E.; Tomanek, D.; Fischer, J. E.; Smalley, R. E., Crystalline Ropes of Metallic Carbon Nanotubes. *Science* **1996,** *273* (5274), 483-487.

86. Jenkins, S.; Jacob, K. I.; Kumar, S., The Effect of Hydrogen Bonding on the Physical and Mechanical Properties of Rigid-Rod Polymers. *Journal of Polymer Science Part B-Polymer Physics* **2000,** *38* (23), 3053-3061.

87. Petrie, C. J. S., The Rheology of Fibre Suspensions. *Journal of Non-Newtonian Fluid Mechanics* **1999,** *87* (2-3), 369-402.

88. Monoclonal Antibody. https://en.wikipedia.org/wiki/Monoclonal_antibody#cite_note-1 (accessed Oct 8, 2019).

89. Liu, J.; Rinzler, A. G.; Dai, H. J.; Hafner, J. H.; Bradley, R. K.; Boul, P. J.; Lu, A.; Iverson, T.; Shelimov, K.; Huffman, C. B.; Rodriguez-Macias, F.; Shon, Y. S.; Lee, T. R.; Colbert, D. T.; Smalley, R. E., Fullerene Pipes. *Science* **1998,** *280* (5367), 1253-1256.

90. AppliChem Biological Buffers. https://www.applichem.com/fileadmin/Broschueren/BioBuffer.pdf.

91. Su, L.; Zou, L.; Fong, C. C.; Wong, W. L.; Wei, F.; Wong, K. Y.; Wu, R. S.; Yang, M., Detection of Cancer Biomarkers by Piezoelectric Biosensor Using PZT Ceramic Resonator as the Transducer. *Biosens Bioelectron* **2013,** *46*, 155-61.

92. Ding, Y.; Liu, J.; Wang, H.; Shen, G.; Yu, R., A Piezoelectric Immunosensor for the Detection of Alpha-Fetoprotein Using an Interface of Gold/Hydroxyapatite Hybrid Nanomaterial. *Biomaterials* **2007,** *28* (12), 2147-54.

93. Kosaka, P. M.; Pini, V.; Ruz, J. J.; Da Silva, R. A.; González, M. U.; Ramos, D.; Calleja, M.; Tamayo, J., Detection of Cancer Biomarkers in Serum Using a Hybrid Mechanical and Optoplasmonic Nanosensor. **2014,** *9* (12), 1047-1053.

94. Etayash, H.; Jiang, K.; Azmi, S.; Thundat, T.; Kaur, K., Real-Time Detection of Breast Cancer Cells Using Peptide-Functionalized Microcantilever Arrays. **2015,** *5*, 13967.

95. Capobianco, J. A.; Shih, W. Y.; Yuan, Q. A.; Adams, G. P.; Shih, W. H., Label-Free, All-Electrical, in Situ Human Epidermal Growth Receptor 2 Detection. *Rev Sci Instrum* **2008,** *79* (7), 076101.

96. Jayanthi, V.; Das, A. B.; Saxena, U., Recent Advances in Biosensor Development for the Detection of Cancer Biomarkers. *Biosens Bioelectron* **2017,** *91*, 15-23.

97. Chou, S.-F.; Hsu, W.-L.; Hwang, J.-M.; Chen, C.-Y., Development of an Immunosensor for Human Ferritin, a Nonspecific Tumor Marker, Based on a Quartz Crystal Microbalance. **2002,** *453* (2), 181-189.

98. Wu, G.; Datar, R. H.; Hansen, K. M.; Thundat, T.; Cote, R. J.; Majumdar, A., Bioassay of Prostate-Specific Antigen (PSA) Using Microcantilevers. *Nature Biotechnology* **2001,** *19* (9), 856-860.

99. S. Vashist, *J. Nanotechnol.*, 2007, **3, 1–15**.

100. Chen, X.; Pan, Y.; Liu, H.; Bai, X.; Wang, N.; Zhang, B., Label-Free Detection of Liver Cancer Cells by Aptamer-Based Microcantilever Biosensor. *Biosens Bioelectron* **2016,** *79*, 353-8.

101. Zhou, Y.; Wang, Z.; Yue, W.; Tang, K.; Ruan, W.; Zhang, Q.; Liu, a. L., Label-Free Detection of P53 Antibody Using a Microcantilever Biosensor with Piezoresistive Readout. In *IEEE Sensors*, Canterbury, New Zealand, 2009.

102. Ali, M. A.; Mondal, K.; Jiao, Y.; Oren, S.; Xu, Z.; Sharma, A.; Dong, L., Microfluidic Immuno-Biochip for Detection of Breast Cancer Biomarkers Using Hierarchical Composite of Porous Graphene and Titanium Dioxide Nanofibers. *ACS Appl Mater Interfaces* **2016,** *8* (32), 20570-82.

103. Ding, C.; Zhang, W.; Wang, W.; Chen, Y.; Li, X., Amplification Strategies Using Electrochemiluminescence Biosensors for the Detection of DNA, Bioactive Molecules and Cancer Biomarkers. *TrAC Trends in Analytical Chemistry* **2015,** *65*, 137-150.

104. Haun, J. B.; Yoon, T. J.; Lee, H.; Weissleder, R., Magnetic Nanoparticle Biosensors. *Wiley Interdiscip Rev Nanomed Nanobiotechnol* **2010,** *2* (3), 291-304.

105. Ilkhani, H.; Sarparast, M.; Noori, A.; Zahra Bathaie, S.; Mousavi, M. F., Electrochemical Aptamer/Antibody Based Sandwich Immunosensor for the Detection of EGFR, a Cancer Biomarker, Using Gold Nanoparticles as a Signaling Probe. *Biosens Bioelectron* **2015,** *74*, 491-7.

106. Li, K.; Liu, G.; Wu, Y.; Hao, P.; Zhou, W.; Zhang, Z., Gold Nanoparticle Amplified Optical Microfiber Evanescent Wave Absorption Biosensor for Cancer Biomarker Detection in Serum. *Talanta* **2014,** *120*, 419-24.

107. Mani, V.; Chikkaveeraiah, B. V.; Patel, V.; Gutkind, J. S.; Rusling, J. F., Ultrasensitive Immunosensor for Cancer Biomarker Proteins Using Gold Nanoparticle Film Electrodes and Multienzyme-Particle Amplification. *ACS Nano* **2009,** *3* (3), 585-94.

108. Myung, S.; Solanki, A.; Kim, C.; Park, J.; Kim, K. S.; Lee, K. B., Graphene-Encapsulated Nanoparticle-Based Biosensor for the Selective Detection of Cancer Biomarkers. *Adv Mater* **2011,** *23* (19), 2221-5.

109. Stoeva, S. I.; Lee, J.-S.; Smith, J. E.; Rosen, S. T.; Mirkin, C. A., Multiplexed Detection of Protein Cancer Markers with Biobarcoded Nanoparticle Probes. **2006,** *128* (26), 8378-8379.

110. Uludag, Y.; Tothill, I. E., Development of a Sensitive Detection Method of Cancer Biomarkers in Human Serum (75%) Using a Quartz Crystal Microbalance Sensor and Nanoparticles Amplification System. *Talanta* **2010,** *82* (1), 277-82.

111. Uludag, Y.; Tothill, I. E., Cancer Biomarker Detection in Serum Samples Using Surface Plasmon Resonance and Quartz Crystal Microbalance Sensors with Nanoparticle Signal Amplification. *Anal Chem* **2012,** *84* (14), 5898-904.

112. Pospisil, M. J.; Saha, P.; Abdulquddos, S.; Noor, M. M.; Davis, V. A.; Green, M. J., Orientation Relaxation Dynamics in Cellulose Nanocrystal Dispersions in the Chiral Liquid Crystalline Phase. *Langmuir* **2018,** *34* (44), 13274-13282.

113. Comprehensive Cellulose Chemistry. Volume 1. Fundamentals and Analytical Methods by D. Klemm, B. Philipp, T. Heinze, U. Heinze, and W. Wagenknecht. Wiley: Weinheim, Germany. 1998. 260 Pp. $236.25. ISBN 3-527-29413-9. *Journal of the American Chemical Society* **1999,** *121* (37), 8677-8677.

114. Cranston, E. D.; Gray, D. G., Birefringence in Spin-Coated Films Containing Cellulose Nanocrystals. *Colloids and Surfaces A: Physicochemical and Engineering Aspects* **2008,** *325* (1-2), 44-51.

115. Pasquali, M. P.; Davis, V. A.; Ericson, L. M.; Saini, R.; Ramesh, S.; Huffman, C.; Ausman, K. D.; Veedu, S.; Batthacharya, A.; Zheng, J.; Kumar, S.; Hauge, R. H.; Smalley, R. E. In *From Ropes to Super-Ropes to Alewives: Alignment & Aggregation of SWNT Dispersions*, AIChE Fall Annual Meeting, Reno, NV, Reno, NV, 2001.

116. Contact Angles. https://chem.libretexts.org/Bookshelves/Physical_and_Theoretical_Chemistry_Textbook_Maps/Supplemental_Modules_(Physical_and_Theoretical_Chemistry)/Physical_Properties_of_Matter/States_of_Matter/Properties_of_Liquids/Contact_Angles (accessed Oct 11,2019).

117. Gijsbers, A.; Nishigaki, T.; Sanchez-Puig, N., Fluorescence Anisotropy as a Tool to Study Protein-Protein Interactions. *J Vis Exp* **2016,** (116).

118. Rinken, A.; Lavogina, D.; Kopanchuk, S., Assays with Detection of Fluorescence Anisotropy: Challenges and Possibilities for Characterizing Ligand Binding to GPCRs. *Trends Pharmacol Sci* **2018,** *39* (2), 187-199.

119. Zhang, H.; Wu, Q.; Berezin, M. Y., Fluorescence Anisotropy (Polarization): From Drug Screening to Precision Medicine. *Expert Opin Drug Discov* **2015,** *10* (11), 1145-61.

120. James J. Miller; Levinson, S. S., *7 - Interferences in Immunoassays*. Academic Press: 1996; p 165-190.

121. Thompson, L.; Nikza, M.; Sbarski, I.; Miller, J.; Yu, A. In *Cellulose Nanocrystal Reinforced Epoxy Vinyl Ester Resins:Fabrication and Mechanical Properties*, 21st International Conference on Composite Materials: ICCM21, Xi'an, China, August 20-25, 2017; Shanyi Du, J. L., Ed. Chinese Society for Composite Materials: Beijing, China.

122. Peng. Y; Han. Y; Gardner, D. J., Spray-Drying Cellulose Nanofibrils: Effect of Drying Process Parameters on Particle Morphology and Size Distribution. *Wood Fiber Science* **2012,** *44 (4)*, pp. 1-14.

123. Wang, N.; Ding, E.; Cheng, R., Thermal Degradation Behaviors of Spherical Cellulose Nanocrystals with Sulfate Groups. *Polymer* **2007,** *48* (12), 3486-3493.

124. Ericson, L. M.; Davis, V. A. *Single Wall Nanotube (SWNT) Fibers GA Tech Visit June 18 - 22, 2001*; Rice University: Houston, July 11, 2001.

125. Tan, Z. J.; Berry, G. C., Studies on the Texture of Nematic Solutions of Rodlike Polymers. 3. Rheo-Optical and Rheological Behavior in Shear. *J. Rheol.* **2003,** *47* (1), 73-104.

126. Wang, L., Preparation of Cellulose Sulphate and Evaluation of Its Properties. *Journal of Fiber Bioengineering and Informatics* **2010,** *3* (1), 32-39.

127. Bradley, M. S. TGA-IR Analysis Using the Omnic Mercury TGA Software. https://assets.thermofisher.com/TFS-Assets/CAD/Application-Notes/Whitepaper_TGAIR_L.pdf.

128. Amand, L.-E.; Tullin, C. J. *The Theory Behind Ftir Analysis: Application Examples from Measurement at the 12 MW Circulating Fluidized Bed Boiler at Chalmers*; Chalmers University of Technology: SE-412 96 Göteborg, Sweden.

129. Mahindrakar, J. N.; Patil, Y. S.; Salunkhe, P. H.; Ankushrao, S. S.; Kadam, V. N.; Ubale, V. P.; Ghanwat, A. A., Optically Transparent, Organosoluble Poly(Ether-Amide)S Bearing Triptycene Unit; Synthesis and Characterization. *Journal of Macromolecular Science, Part A* **2018,** *55* (9), 658-667.

130. Bischof, J. C.; He, X., Thermal Stability of Proteins. *Ann N Y Acad Sci* **2005,** *1066*, 12-33.

131. Zhao, Z.; Weinstein, E.; Tuzova, M.; Davidson, A.; Mundel, P.; Marambio, P.; Putterman, C., Cross-Reactivity of Human Lupus Anti-DNA Antibodies With Alpha-Actinin and Nephritogenic Potential. **2005,** *52* (2), 522-530.

132. Priyamvada, L.; Quicke, K. M.; Hudson, W. H.; Onlamoon, N.; Sewatanon, J.; Edupuganti, S.; Pattanapanyasat, K.; Chokephaibulkit, K.; Mulligan, M. J.; Wilson, P. C.; Ahmed, R.; Suthar, M. S.; Wrammert, J., Human Antibody Responses after Dengue Virus Infection are Highly Cross-Reactive to Zika Virus. *Proceedings of the National Academy of Sciences* **2016,** *113* (28), 7852-7857.

133. Tsai, W.-Y.; Lai, C.-Y.; Wu, Y.-C.; Lin, H.-E.; Edwards, C.; Jumnainsong, A.; Kliks, S.; Halstead, S.; Mongkolsapaya, J.; Screaton, G. R.; Wang, W.-K., High-Avidity and Potently Neutralizing Cross-Reactive Human Monoclonal Antibodies Derived from Secondary Dengue Virus Infection. **2013,** *87* (23), 12562-12575.

134. Jin, C.; Altmann, F.; Strasser, R.; Mach, L.; Schahs, M.; Kunert, R.; Rademacher, T.; Glossl, J.; Steinkellner, H., A Plant-derived Human Monoclonal Antibody Induces an Anti-Carbohydrate Immune Response in Rabbits. *Glycobiology* **2007,** *18* (3), 235-241.

135. Jass, J. R.; Allison, L. M.; Edgar, S., Monoclonal Antibody TKH2 to the Cancer-Associated Epitope Sialosyl Tn Shows Cross-Reactivity with Variants of Normal Colorectal Goblet Cell Mucin. *Pathology* **1994,** *26* (4), 418-422.

136. Finlay, J. A.; Day, J. R.; Rittenhouse, H. G., Polyclonal and Monoclonal Antibodies to Prostate-Specific Antigen can Cross-React with Human Kallikrein 2 and Human Kallikrein 1. **1999,** *53* (4), 746-751.

137. Dillman, R. O.; Beauregard, J. C.; Sobol, R. E.; Royston, I.; Bartholomew, R. M.; Hagan, P. S.; Halpern, S. E., Lack of Radioimmunodetection and Complications Associated with Monoclonal Anticarcinoembryonic Antigen Antibody Cross-Reactivity with an Antigen on Circulating Cells. *Cancer Res* **1984,** *44* (5), 2213-8.

138. Primus, F. J.; Newman, E. S.; Hansen, H. J., Affinity in Radioimmunoassay of Antibody Cross-Reactive with Carcinoembryonic Antigen (CEA) and Colon Carcinoma Antigen-iii (CCA-iii). *The Journal of Immunology* **1977,** *118,* 55-61.